NASA Technical Paper 3577

ATCOM Technical Report 95-A-006

August 1995

3-D Wake Measurements Near a Hovering Rotor for Determining Profile and Induced Drag

K. W. McAlister, C. A. Schuler, L. Branum, and J. C. Wu

National Aeronautics and Space Administration

US Army
Aviation and Troop Command

NASA Technical Paper 3577

ATCOM Technical Report 95-A-006

1995

3-D Wake Measurements Near a Hovering Rotor for Determining Profile and Induced Drag

K. W. McAlister
Aeroflightdynamics Directorate, USAAVRDEC, ATCOM, Ames Research Center, Moffett Field, California
C. A. Schuler
Aerometrics, Inc., Sunnyvale, California
L. Branum
Aeroflightdynamics Directorate, USAAVRDEC, ATCOM, Ames Research Center, Moffett Field, California
J. C. Wu
School of Aerospace Engineering, Georgia Institute of Technology, Atlanta, Georgia

National Aeronautics and Space Administration

US Army
Aviation and Troop Command

Aeroflightdynamics Directorate
Moffett Field, CA 94035-1000

CONTENTS

NOMENCLATURE

c	chord of rotor blade (fixed)
C_q	torque coefficient, torque/$\rho\pi\Omega^2R^5$
C_t	thrust coefficient, thrust/$\rho\pi\Omega^2R^4$
d	diameter of tip vortex
D	total drag
D_i	induced drag
D_p	profile drag
f	function defined by mass continuity
HW	hot-wire anemometer
LDV	laser Doppler velocimeter
LV	laser velocimeter
n	number of rotor blades
N	total number of time steps
p	static pressure
P	total pressure
PC	personal computer
r	radius from center of vortex
R	radius of blade tip
RWTS	rotary-wing test stand
S	integration plane
SM	smoke-flow visualization
t	time
u	x-component of velocity in drag model
v	y-component of velocity in drag model
V	velocity
V_c	maximum circulatory velocity of tip vortex
w	z-component of velocity in drag model
$\bar{x}$	distance behind rotor blade
x	coordinate along free-stream direction

y	coordinate normal to x-z plane
z	coordinate normal to x-y plane
Γ	circulation
Γ_b	maximum blade circulation
ρ	density of air
θ	collective pitch at 0.75R
μ	advance ratio, $V_\infty/\Omega R$
ξ	x-component of vorticity
σ	solidity of rotor disk, $nc/\pi R$
ϕ	scalar potential
ψ	stream function in y-z plane
Ψ	rotor-blade azimuth
ω	vorticity
Ω	rotor-blade angular velocity
2-D	two-dimensional
3-D	three-dimensional

Subscripts

a,b	upstream, downstream integration-plane locations
max	maximum
min	minimum
∞	free-stream condition
1,2,3	components relative to laser-velocimetry system

3-D WAKE MEASUREMENTS NEAR A HOVERING ROTOR FOR DETERMINING PROFILE AND INDUCED DRAG

K. W. MCALISTER, C. A. SCHULER,* L. BRANUM,† AND J. C. WU‡

Aeroflightdynamics Directorate, USAAVRDEC, ATCOM, Ames Research Center

SUMMARY

Primarily an experimental effort, this study focuses on the velocity and vorticity fields in the near wake of a hovering rotor. Drag terminology is reviewed, and the theory for separately determining the profile- and induced-drag components from wake quantities is introduced. Instantaneous visualizations of the flow field are used to center the laser velocimeter (LV) measurements on the vortex core and to assess the extent of the positional meandering of the trailing vortex. Velocity profiles obtained at different rotor speeds and distances behind the rotor blade clearly indicate the position, size, and rate of movement of the wake sheet and the core of the trailing vortex. The results also show the distribution of vorticity along the wake sheet and within the trailing vortex.

INTRODUCTION

Designers of new rotor configurations (especially those involving changes to the tip region) who want to improve the performance of the helicopter must consider the drag mechanisms that result from the altered flow field around each blade. Whether the effort is theoretical or experimental, it is important to distinguish between and accurately account for the contributions of friction and pressure drag. Although the induced drag (which is a large part of the pressure drag) is much greater than the friction drag when the rotor is developing lift, small changes in either component along the outer radius of the blade can have a considerable effect on the performance of the helicopter.

The induced drag cannot be determined from surface measurements on the rotor blade. However, methods based on the integration of wake quantities have been used for many years to determine the profile drag on two-dimensional (2-D) bodies. Although the wake-integral technique has been applied to three-dimensional (3-D) bodies in a few cases, the separate quantification of profile and induced drag on rotating 3-D bodies based solely on wake measurements is virtually nonexistent. Because of the importance of discriminating between the various components of drag, a theoretical effort is presently under way to develop rigorously the necessary equations for calculating induced and profile drag on a rotor using only near-wake measurements.

---

*Aerometrics, Inc., Sunnyvale, California.
†Aeroflightdynamics Directorate, USAAVRDEC, ATCOM, Ames Research Center, Moffett Field, California.
‡School of Aerospace Engineering, Georgia Institute of Technology, Atlanta, Georgia.

The philosophy behind the present approach for determining drag is that if the governing equations can be cast in terms of vorticity, then only the relatively confined vortical wake will need to be considered. The fundamental equations were first derived by Wu et al. (ref. 1) for the far wake of a fixed 3-D body and applied to a lifting wing. Following the same principles, Hackett and Sugavanam (ref. 2) developed a form of the equations that is valid in the near wake, and they applied the equations to the drag on a stationary model car in a wind tunnel.

The data presented in this report consist of near-wake measurements behind a hovering rotor. The flow field is surveyed across a given area as well as during a finite period of time in order to calculate vorticity and velocity derivatives over orthogonal planes that contain the shed wake and the trailing vortex. Although the quantity of measurements is not extensive, they should be sufficient for guiding the development of the theory and for judging the relative importance of various terms in the governing equations.

COMPONENTS OF DRAG

The resultant force vector acting on an airfoil or wing derives from the integration of two surface tractions, one that acts normal to the surface (called pressure) and another that acts tangential to the surface (called friction). It is customary to regard this resultant force vector in terms of two orthogonal components (assuming there is no side force) that are directionally referenced to the free-stream velocity (defined at a distance far from the airfoil). The force component that is parallel to the free-stream direction is called drag, and the component that is normal to the free-stream direction is called lift. The total drag force, for example, is composed of forces due to pressure and friction (fig. 1).

However, in the case of a lifting 3-D airfoil (a wing at a nonzero angle of attack), it is more useful to regard the total drag force as the sum of the drag that would exist had the airfoil been 2-D (called "profile" drag) plus the additional drag that arises because the airfoil has a finite aspect ratio (ref. 3). The flow around the tip of a wing develops into a strong trailing vortex (directed nearly parallel to the free-stream velocity), and this vortex induces a reduction in the apparent angle of attack in the vicinity of the wing tip. Relative to the free-stream velocity vector, the induced flow has the effect of tilting the lift vector away from the normal, which in turn produces a component of force in the drag direction (ref. 4). This additional drag is called the "induced" drag (sometimes called "vortex" drag or "edge" drag), and it exists only in 3-D flows.

From a different point of view, the induced flow merely causes a redistribution of pressure near the tip so that the pressure drag becomes equal to "form" drag (as if the airfoil were 2-D) plus the additional induced drag (whenever the airfoil is 3-D and has lift). The total drag force is therefore composed of induced and profile drag, and the profile drag is composed of form and friction drag (fig. 2). If the flow does not separate from the airfoil, then the form drag is zero. If the flow is inviscid (no boundary layer), then both the form drag and the friction drag are zero (D'Alembert's paradox). If a 3-D airfoil has no lift on any section along the span, then the induced drag is zero. If the section lift varies from positive to negative values along the span of the wing such that the net lift is zero, the induced drag will not be zero since energy is always extracted from the flow whenever vorticity is produced (regardless of the sign).

When the flow is 2-D, the induced drag is always zero. All of the vorticity in the wake originates in the boundary layer on the airfoil and is oriented perpendicular to the flow. The bound vortex (which imparts equal amounts of upwash ahead and downwash behind the airfoil) does not change the "local" free-stream velocity, hence there is no "tilting back" of the lift vector and, therefore, no component of force is produced in the drag direction.

When the flow is 3-D, the energy required to impart a vortical motion to the fluid manifests itself in an altered pressure distribution on the surface of the airfoil. In the purest physical terms, a lifting wing produces a downwash that simply alters the pressure distribution from its 2-D counterpart. In this case the pressure integral no longer represents just the form drag; it now reflects the sum of both the form drag and the induced drag. Form- and induced-drag forces cannot be separately identified in the surface integration of pressure. The trailing-vortex system (which is semi-infinite) imparts a downwash on the wing (strongest near the tip) and causes a decrease in the "local" angle of attack. Keeping the lift vector perpendicular to the local free-stream velocity is equivalent to tilting the lift vector back, and this results in a component of lift along the original drag direction.

The drag in steady flow can be determined by evaluating the static pressure and the momentum flux along the boundaries of the control volume surrounding the airfoil. Consider a constant-area control volume with lateral boundaries (defined by y and z) that are solid (i.e., test-section walls) or located at infinity (fig. 3). The total drag, D, on a 3-D object can be determined from quantities on the upstream and downstream boundaries according to:

$$D = \iint \left((p_a + \rho_a u_a^2) - (p_b + \rho_b u_b^2) \right) dS \tag{1}$$

where p is static pressure, ρ is the density of air, u is the x-component of velocity, and a and b represent upstream and downstream, respectively. The variable of integration, S, is taken to be the infinite planes that bound the nearby flow both upstream and downstream of the airfoil. Clearly dS is equivalent to dydz.

If we assume the flow to be incompressible and denote the total pressure, P, by

$$P = p + \frac{1}{2}\rho(u^2 + v^2 + w^2) \tag{2}$$

where v and w are the y- and z-components of the velocity, respectively, the drag can be stated as

$$\begin{aligned} D = \underbrace{\iint}_{\text{wake}} (P_a - P_b)\, dS + \frac{1}{2}\rho \iint (u_a^2 - u_b^2)\, dS \\ - \frac{1}{2}\rho \iint \left((v_a^2 + w_a^2) - (v_b^2 + w_b^2) \right) dS \end{aligned} \tag{3}$$

with the integrand of the first term vanishing everywhere outside the vortical-wake region.

Betz (ref. 5) introduced a hypothetical velocity, u'_b, downstream from the airfoil (fig. 4) that is identical with u_b outside the wake depression, but it differs from u_b inside the depression by an amount necessary for the total pressure P'_b to be equal to P_a (or P_∞ since there are no losses upstream of the airfoil). In other words,

$$P_\infty = p_b + \frac{1}{2}\rho(u_b'^2 + v_b^2 + w_b^2) \tag{4}$$

Following a more correct treatment by Maskell (ref. 6) and working with identities involving u_∞ and the more general case for u, Wu et al. (ref. 1) and Hackett and Sugavanam (ref. 2) have shown that the drag has the form

$$\begin{aligned} D = & \underbrace{\iint}_{\text{wake}} (P_\infty - P_b)\, dS \\ & + \frac{1}{2}\rho \underbrace{\iint}_{\text{wake}} (u'_b - u_b)(u'_b + u_b - 2u_\infty)\, dS \\ & + \frac{1}{2}\rho \iint \left((u'_a - u_\infty)^2 - (u'_b - u_\infty)^2\right) dS \\ & + \frac{1}{2}\rho \iint \left((v_b^2 + w_b^2) - (v_a^2 + w_a^2)\right) dS \end{aligned} \tag{5}$$

The first two terms, originally derived by Betz for an external flow (without wind-tunnel walls) and called the profile drag, contain integrands that vanish outside the wake depression. The third term, subsequently derived by Maskell and interpreted as being a small correction to the profile drag due to blockage when wind-tunnel walls are present, does not vanish outside the wake depression. For now, it will be assumed that the blockage of the flow is negligibly small when the test-section walls are far removed, so that this entire term may be omitted. The last term, which represents the induced drag, does not vanish outside the vortical wake region (although it becomes small). The profile drag, D_p, can therefore be determined from quantities in the wake downstream of the model according to

$$D_p = \underbrace{\iint}_{wake} (P_\infty - P_b)\, dS + \frac{1}{2}\rho \underbrace{\iint}_{wake} (u_b' - u_b)(u_b' + u_b - 2u_\infty)\, dS \tag{6}$$

Thus far the flow has been assumed to be steady and incompressible, and the lateral, control-volume surfaces (which are possibly solid) are located at a large distance from the model. The next task is to show that the induced drag, which is the last integral in equation (5), can also be expressed as a wake integral. From continuity,

$$\frac{\partial v}{\partial y} + \frac{\partial w}{\partial z} = -\frac{\partial u}{\partial x} = f \tag{7}$$

The x component of the vorticity vector, ξ, is defined by

$$\frac{\partial w}{\partial y} - \frac{\partial v}{\partial z} = \xi \tag{8}$$

On surface S, where x is constant, the variables v, w, f, and ξ are functions of y and z only. Therefore, if ξ(y,z) and f(y,z) are known on S, then with proper boundary conditions v(y,z) and w(y,z) can be determined. In other words, the flow conditions on S can be regarded as a 2-D problem. As such, it is useful to introduce a stream function, ϕ, and a scalar potential, ϕ, and let

$$v = \frac{\partial \psi}{\partial z} + \frac{\partial \phi}{\partial y} \tag{9}$$

and

$$w = \frac{\partial \psi}{\partial y} + \frac{\partial \phi}{\partial z} \tag{10}$$

Substituting equations (9) and (10) into equations (7) and (8) yields

$$f = \frac{\partial^2 \phi}{\partial y^2} + \frac{\partial^2 \phi}{\partial z^2} \tag{11}$$

and

$$-\xi = \frac{\partial^2 \psi}{\partial y^2} + \frac{\partial^2 \psi}{\partial z^2} \tag{12}$$

Using identities based on equations (7)–(12) and imposing Green's theorem and the divergence theorem, we calculate the induced drag

as

$$\begin{aligned} D_i &= \frac{1}{2}\rho \iint \left(\left({v_b}^2 + {w_b}^2 \right) - \left({v_a}^2 + {w_a}^2 \right) \right) dS \\ &= \frac{1}{2}\rho \iint \left(\psi_b \xi_b - \psi_a \xi_a \right) dS \\ &\quad - \frac{1}{2}\rho \iint \left(\phi_b f_b - \phi_a f_a \right) dS \end{aligned} \tag{13}$$

Under certain circumstances the second integral in equation (13) is arguably negligible. If we assume that the vorticity upstream of the model, ξ_a, is zero and recognize that the vorticity downstream of the model, ξ_b, is present only in the wake, the expression for the induced drag simplifies to

$$D_i = \frac{1}{2}\rho \underbrace{\iint}_{wake} \psi_b \xi_b \, dS \tag{14}$$

The theoretical development outlined above is intended to show that the profile drag and the induced drag can be separately quantified and that they both can be determined from conditions that are limited to the wake downstream of the model. Various detailed arguments that explain and defend these results, along with an effort to extend this approach to the rotating case, are beyond the scope of this study, and they will be presented in another report. The present data emphasize certain features of the flow in the wake of a rotor blade in order to guide the development of the theory, to substantiate the relative importance of various terms, and to provide a basis for calculating drag components from wake measurements.

TEST DESCRIPTION

Facility and Model

Test chamber– The experiment was performed in the Hover Test Chamber at the NASA Ames Research Center under the authority of the U.S. Army Aeroflightdynamics Directorate. The chamber has a base of 26 ft × 32 ft and a height of 28 ft. To minimize recirculation in the chamber as well as limit the movement of air around instrumentation located near the floor (fig. 5), the collective pitch of

the rotor blades was set to a negative angle so that the wake would be directed upwards. With the rotor acting like a pump, air was drawn into the chamber through two opposing doors, then confined by an annular diffuser located above the rotor, and finally exhausted to the exterior through 10 ports near the top of the chamber (fig. 6).

Test stand– The rotary-wing test stand (RWTS) was used to drive the rotor (fig. 7). The RWTS was configured with a single, 90-hp electric motor and a transmission with a 6:1 gear ratio. The particular combination of generator, drive motor, and transmission used in this test is capable of producing (neglecting rotor drag) a maximum speed of 1250 rpm. All major natural frequencies of the test stand (with hub and blades installed) were found to occur at speeds greater than 40 percent above the maximum attainable speed. An encoder with a resolution of 4096 steps was connected to the bottom of the rotor shaft to provide a reference for the angular location of the rotor blade.

Hub– The hub consisted of 2 steel sections that were held together by 16 cap screws. After the rotor blades were set to the desired pitch angle, the screws were tightened and the two halves became rigidly clamped around the root portion of the blades (fig. 8). The hub and blade assembly were designed to have a 0 deg coning angle.

Blades– Machined from aluminum, the blades are solid throughout except for seven radial lightening holes near the tip (not shown), a plenum at the tip, and a 15/32-in.-diameter passage extending from the root to the tip (fig. 9). The blades are rectangular and untwisted, and they have a chord length of 7.5 in. and a radius of 45 in. (The diameter of the rotor is 7.5 ft.) The solidity of the two-bladed rotor, σ, is 0.106. Each blade weighs approximately 30 lb, and the center of gravity is located at 0.36R. The profile of the blade is a NACA 0020 airfoil at 0.2R that linearly tapers to a NACA 0012 at 0.5R. The profile remains a NACA 0012 from 0.5R to 1.0R.

The tip of each rotor blade was hollowed out to a depth of 1 in. to form a settling chamber for the seed particles that were routed through the spanwise passage from the root of the blade. The settling chamber of each blade was sealed with an aluminum cover plate secured with 4 machine screws. Six 3/16-in.-diameter holes were drilled in the upper and lower surfaces of the blade at 0.2 in. from the tip. Tape was wrapped around the tip of the blade to cover all the surface holes, and then only that portion of the tape directly above the cavity of the selected hole was removed. This procedure provided some control over the placement of seed particles into the core of the trailing vortex.

Load Measurements

A flexible coupling between the input shaft and the balance was instrumented to measure torque (limited to 510 ft-lb). A dummy balance was installed in the RWTS during the laser velocimeter (LV) portion of the test. At the conclusion of the test the RWTS was moved to another location, and the VSB-27M balance was installed so that thrust (limited to 1900 lb) could also be measured. Thrust and torque loads were simultaneously obtained over the full speed range (limited to 1150 rpm because of rotor drag).

Flow Visualization

A propylene-glycol type of fluid was vaporized to produce the particles needed for visualizing the trailing vortex. The vapor was carried along a rigid pipe that was routed along the axis of the rotor wake to a point just above the rotor hub. The particles were captured by a funnel that was rigidly attached to the rotating hub. From there they were drawn by the favorable pressure gradient produced by centrifugal forces along the blade and the relatively low pressure that was present at the hole on the upper surface of the blade near the tip. Among the six holes that could have been selected, the hole on the upper surface that was nearest the leading edge of the blade proved to be the most effective one for depositing seed particles into the core of the trailing vortex.

A sheet of light passing through the wake of the rotor was formed by refracting a 4-Watt laser beam through a cylindrical lens. The light sheet was adjusted so that it passed near the tip of the rotor blade when the tip was centered within the boundaries of the LV traverse (fig. 5). Since the laser-light sheet was continuous, the rotor wake was "frozen" at the desired blade azimuth by synchronizing a gated video camera with the shaft encoder. This procedure enabled a clear image to be obtained of the cross section of the trailing-vortex core.

Velocity Measurements

Beam management– Three components of velocity were measured with a three-color LV system. An argon-ion laser was used to produce green (5145-Å), blue (4880-Å), and violet (4765-Å) beams. These three beams were optically separated and divided into six power-adjusted beams. Then one beam from each color pair was altered by 40 megahertz (so that the direction of flow could be determined), after which all the beams were directed into optical fibers. The fibers (15-m long) were terminated at the traverse, and the beams were refocused to a common point by two transmitting lenses (with focal lengths of 2286 mm) that were separated by 50 deg (fig. 10). The cross section of the elliptical volume formed by each beam pair had a diameter of approximately 230 μm, and the spacing between the fringes within the volume was 10 mm. A portion of the light scattered by the particles passing through the "probe volume" was collected by a 1000-mm lens (not shown in fig. 10) located midway between the two transmitting lenses. This receiving lens was used as a temporary substitute for the large Cassegrain telescope (located in the center of the traverse) that was found to be astigmatic at the time of the test. The depth of the active portion of the probe volume was restricted to about 500 mm by a spatial filter as well as by the 25-deg offset between the collection axis and the transmission axis.

Traverse– The measurement plane was defined by the transverse and vertical displacements of the traverse. The transverse axis of the traverse was aligned with the span of the rotor blade when the blade was rotated to a particular angle. The output from the rotor encoder at this azimuth angle was used as a reference for locating the rotor relative to this measurement plane. The traverse was positioned so that the flow field could be surveyed over an area of 4 ft^2 in the neighborhood of the blade tip. All the measurements were referenced to the center of the trailing vortex, and they are considered to be accurate to within ±0.01 mm. The procedure for positioning the probe volume on the center of the vortex was based on "strobing" the video camera at the desired rotor azimuth so that an

image of the vortex could be “frozen” in the plane of the light sheet. The traverse was then moved as required so that the LV beams crossed at the center of the image.

Acquisition window– A majority of the data in this experiment focused on the wake after the tip of the rotor had advanced a distance of 3 chords past the measurement plane. To minimize the amount of data to be collected, an acceptance window of ±0.5 chord was imposed (equivalent to 2.6 percent of a complete blade rotation, or $\Delta\Psi = 9.5$ deg). The encoder window was computed to be the count observed at the reference azimuth plus $3 \times 108 \pm 54$ counts (that is, 3 chords ±0.5 chord). This computation was based on the resolution of the encoder (4096 counts) as well as the chord length of the blade and the radius of the rotor (which spans an arc of 108 encoder counts).

Flow seeding– Two seed generators were used to produce the light-scattering particles needed for LV measurements. Both generators were similar in that they vaporized a propylene-glycol type of fluid to produce particles with an average diameter reported to be approximately 1 μm. The index of refraction for these particles was taken to be 1.47. One generator was dedicated to supplying the particles that were routed through the rotor blade and deposited in the core of the trailing vortex. The other generator was placed above and outside of the rotor disk so that these particles would be entrained in the flow moving down toward the rotor and then become more widely spread throughout the rotor wake. Although the size of the particles was not measured in situ, their size was inferred to be on the order of 1 mm because the rotor blades remained dry during the test (larger particles have been observed to impact approaching surfaces rather than following the curved path of the air). From a fluid-dynamic point of view, the size of the particle is important because it affects how well the particle tracks the flow. The effect is especially critical in regions of high acceleration.

Data acquisition– Particles passing through the intersection of coherent, polarized beam pairs will scatter light with a Doppler-difference frequency that is proportional to the velocity of the particles. The instrument used to analyze these signals was a frequency-domain processor. A major benefit from processing the signal bursts in the frequency domain, rather than in the time domain, is that meaningful results can be obtained from the comparatively weak and noisy signals that are typical of backscatter collections. Signal coincidence was not required since only the mean values of the velocity components were of interest; however, a minimum of 1000 samples was acquired for each velocity component at every location. Data collection was inhibited except during the interval of time it took for the tip of the rotor blade to advance a distance of 1 chord. In this experiment the 1-chord interval was chosen to be either from
$0 \rightarrow 1$ chord or from $2.5 \rightarrow 3.5$ chords behind the rotor blade. A timer, which was reset each time the rotor made a complete revolution, was sampled whenever a valid burst was detected. All traverse and acquisition functions were controlled by a personal computer (PC).

RESULTS AND DISCUSSION

Rotor Loads

Thrust and torque loads were measured directly with the collective-pitch angle of the blades fixed at -8 deg (the thrust vector was directed downwards). A series of discrete measurements was obtained for both increasing and decreasing rotor speeds up to a value of 1150 rpm (fig. 11). Horsepower and torque are related by: hp = torque × tip speed/5250, where torque is measured in ft-lb and the tip speed in rpm. Since all the velocity measurements were obtained at rotor speeds of 550 rpm and 1100 rpm, the corresponding loads at these speeds have been tabulated for convenience (table 1).

Table 1. Measured loads

Speed, rpm	Power, hp	Torque, ft-lb	C_g	Thrust, lb	C_t
550	0.98	9.36	0.00052	24.6	0.0051
1100	7.57	36.13	0.00050	95.1	0.0050

Statistical Resolution of Velocity

During the time interval required for the rotor tip to move 1 chord length, data (typically noncoincident, that is, not all three velocity measurements were made on the same particle) were recorded along with the relative time (referenced to the reset point of every blade revolution) for each of the three velocity components. The data window of acceptance was 1.44 ms wide when the rotor speed was 1100 rpm. Some scatter in the measurements was present because of turbulence, unsteady inflow into the hover chamber, and the response time of particles with different diameters. Using a least-squares approximation, a second degree polynomial was fit to the data, and the standard deviation was calculated. Data differing from the curve by more than twice the standard deviation were excluded from the set, and a new curve was fitted to the data.

The results from a typical case appear in figure 12, which shows the final curve fit for each velocity component (V_1,V_2,V_3) along with the accepted data (solid symbols) and the excluded data (open symbols). The data window for this case was located between 2.5 and 3.5 chords behind the trailing edge of the blade tip. V_1 is in the same direction as V_z and is, therefore, equivalent. The orthogonal components V_x and V_y must be calculated from V_2 and V_3 (each of which intersects the y-axis at 25 deg). In those cases where the data window was immediately behind the rotor blade (from 0 to 1 chord), the flow accelerations encountered in the wake nearest the trailing edge required the extent of the second-degree curve fit to be limited (fig. 13). The response of the particles to the rapidly changing conditions in this region offers some assurance that good fidelity was achieved in the range where the curve fit was imposed.

The trailing vortex at 3 chords behind the rotor blade (+3c, which is equivalent to Ψ = 28.6 deg) was observed to randomly move a small amount (less than 1 core diameter) over the y-z plane. Since no

attempt was made to account for this motion during the acquisition of LV data, the calculated peak velocities (based on statistical averages) are undoubtedly lower than the actual instantaneous values. Meander increased substantially with vortex age (fig. 14), to such an extent that measurements of even the nearest vortices that intersect the y-z plane at Ψ = 180 deg (+3c) and Ψ = 360 deg (+3c) were not considered.

Wake Profiles

Five linear traverses were made across the flow in the y-z plane to obtain detailed velocity profiles of the trailing vortex and the wake that was shed behind the rotor blade (fig. 15). The horizontal traverse focused on the trailing vortex, and the vertical traverses were aimed at locating the wake sheet behind the rotor blade. The velocity components V_x and V_y are both parallel to the rotor disk, with V_x directed toward the rotor blade and V_y directed inboard. V_z is aligned with the axis of rotation of the rotor, and it is positive in the vertical direction.

Trailing vortex– In figure 16 the disturbance wave produced by the trailing vortex shows that the vortex moved inboard (+y direction) as the rotor blade moved from 0.3 to 1.0 chord past the measurement plane. The y- and z-velocity components are dominant, and they appear to maintain the same profile shape during this interval. In figure 17 the magnitude of the velocity components can be examined more precisely (in this case the blade tip has moved forward 0.5 chord length past the measurement plane). The data for the vertical component of velocity (V_z) show the classical vortex shape, with the peak velocity reaching about 31 percent of the rotor-tip speed (ΩR = 132 m/s at 1100 rpm). Previous measurements of the peak velocity of trailing vortices at “near-wake” distances behind hovering rotors (Ψ < 180 deg) have been reported (table 2, refs. 7–15) to range from 12 to 67 percent of the rotor-tip speed.

Although the trailing vortex is moving inboard, within the core of the vortex (defined by the maximum and minimum peaks in V_z) V_y is directed outboard with a magnitude of 31 percent of the rotor-tip speed. The flow follows the rotor blade as it sweeps past the measurement plane, with the maximum value of V_x being 8 percent of the rotor-tip speed and occurring at an off-center position that aligns closely with the negative peak in V_z.

Further downstream in the wake (as the rotor-blade tip moves from 2.5 to 3.5 chords past the measurement station), the trailing vortex experiences some significant changes. In figure 18 the disturbance wave produced by the trailing vortex shows that the vortex is continuing to move inboard (+y direction); however, V_x has become more pronounced, and V_y has changed direction (indicating a switch from outboard-directed flow to inboard-directed flow). In figure 19 the data for the vertical component of velocity (V_z) again show the classical vortex shape, with the peak velocity reaching about 30 percent of the rotor-tip speed when the tip of the rotor was 3 chords past the measurement plane.

Table 2. Tip vortex from hovering rotors

Section profile	n	c, cm	R, m	Ω, rpm	ΩR, m/s	θ, deg	C_t/σ	Γ_0, m^2/s	Age, deg	$V_c/\Omega R$	d/c	Method	Source (ref.)
NACA 0012	1	12.7	0.61	500	31.9	6.2	0.033	0.57	60	0.12	0.16	LDV	7
NACA 0012	1	12.7	0.61	500	31.9	12.0	0.086	1.16	30	0.21	0.16	LDV	7
NACA 0012	2	19.1	1.14	1250	150.0	8.0	0.043	4.04	54	0.47	—	HW	8
NACA 0012	2	19.1	1.14	1250	150.0	12.0	0.074	6.49	52	0.67	—	HW	8
NACA 0012	2	19.1	1.14	1250	150.0	8.0	0.043	4.04	215	0.51	—	HW	8
NACA 0012	2	19.1	1.14	1250	150.0	12.0	0.074	6.49	203	0.77	—	HW	8
NACA 0012	2	19.1	1.14	1250	150.0	8.0	0.043	4.04	48	0.37	—	HW	8
NACA 0012	2	19.1	1.14	1750	210.0	8.0	0.043	5.66	60	0.27	—	HW	8
NACA 0012	2	19.1	1.14	2250	270.0	8.0	0.043	7.27	66	0.27	—	HW	8
NACA 0012	2	7.6	1.05	1250	136.8	8.0	0.080	2.76	58	0.58	—	HW	9
NACA 0012	2	7.6	1.05	1250	136.8	12.0	0.127	4.17	76	0.42	—	HW	9
NACA 0012	2	7.6	1.05	1250	136.8	9.8[a]	0.093	2.77	65	0.43	—	HW	9
NACA 0012	2	7.6	1.05	1250	136.8	13.5[a]	0.136	4.09	58	0.59	—	HW	9
NACA 0012	1	41.7	8.53	205	182.9	twist	0.084	—	100	0.25	0.01	HW	10
NACA 0012	1	41.7	8.53	205	182.9	twist	0.103	—	100	0.33	0.01	HW	10
SA 131xx	3	12.3	0.86	2340	210.0	twist	0.075	—	85	0.22	0.18	LDV	11
OA 209	2	5.0	0.75	1362	107.0	6.0[a]	0.054	1.04	120	0.24	0.05	LDV	12
OA 209	2	5.0	0.75	1362	107.0	8.0[a]	0.080	1.25	120	0.35	0.06	LDV	12
OA 209	2	5.0	0.75	1362	107.0	10.0[a]	0.100	2.15	120	0.41	0.12	LDV	12
OA 209	2	5.0	0.75	1362	107.0	10.0[a]	0.100	2.15	80	0.43	0.07	LDV	12
OA 209	2	5.0	0.75	1362	107.0	10.0[a]	0.100	2.15	160	0.38	0.17	LDV	12
BV 23010	2	5.0	0.75	1362	107.0	8.0[a]	0.075	1.15	120	0.32	0.10	LDV	12
BV 23010	2	5.0	0.75	1362	107.0	10.0[a]	0.095	1.60	120	0.37	0.12	LDV	12
NACA 0012	1	10.2	0.61	2379	152.0	9.0[a]	0.083	—	75	0.33	0.06	HW	13
—	2	5.3	1.40	666	48.6	15.8[a]	—	—	18	0.22	0.35	SM	14
NACA 0012	2	28.2[a]	5.35	340	190.5	6.3[a]	0.055	—	220	0.22	0.15	HW	15
NACA 0012	2	28.2[a]	5.35	245	137.2	10.8[a]	0.110	—	169	0.44	0.15	HW	15
NACA 0012	2	28.2[a]	5.35	245	137.2	6.3[a]	0.055	—	287	0.13	0.19	HW	15
NACA 0012	2	19.1	1.14	550	66.0	8.0	0.048	—	29	0.26	0.10	LDV	present
NACA 0012	2	19.1	1.14	1100	132.0	8.0	0.047	—	5	0.31	0.10	LDV	present
NACA 0012	2	19.1	1.14	1100	132.0	8.0	0.047	—	29	0.30	0.10	LDV	present

[a]Indicates either tapered or twisted blade (value given at $0.75R$).

Within the core of the vortex, V_y also approaches 30 percent of the rotor-tip speed, but it is now directed inboard. A wider zone of flow follows the rotor blade as it sweeps past the measurement plane, with the maximum value of V_x increasing to 18 percent of the rotor-tip speed and now occurring at the center of the trailing vortex. Lowering the rotor speed from 1100 to 550 rpm does not change the general appearance of the trailing vortex (fig. 20), nor does it significantly change the magnitude of the velocity components (fig. 21) relative to the rotor-tip speed.

The velocity profiles obtained from traverses directly across the trailing vortex not only reveal the maximum circulatory velocity, V_c, but also indicate the core size and the concentration of vorticity. The concentration of vorticity is suggested by the rapid variation of circulation with r, where r is the radial distance from the center of the vortex, which is assumed to be midway between the velocity peaks. The results obtained at different rotor speeds and at different vortex ages show (fig. 22) that the core size remains the same (20 mm or 10 percent of the chord) over a distance of 3 chords behind the rotor blade. However, the vorticity appears to extend over a larger region (an increasing distance beyond the core boundaries) as the vortex ages. (This conclusion is based on the location of the "knee" in the curve for Γ, which occurs on either side of the core.) For the three cases shown in figure 22, C_t/σ is basically unchanged (0.047). The curve for Γ continues to rise beyond the "knee" on the inboard side because of the rotor "downwash." The strength of the trailing vortex at $\bar{x} = 3c$ is $\Gamma/c\Omega R = 0.16$ when $\Omega = 1{,}100$ rpm. This value is obtained by assuming that the downwash contribution to V_z can be approximately accounted for by averaging the circulation at the knee or either side of the vortex center. Strictly speaking, it is more correct to regard Γ as representing the moment of velocity since it was calculated according to $\Gamma = 2\pi r V_z$. If the flow is symmetrical about the center of the vortex, and if the convection velocity of the vortex is properly accounted for, then Γ becomes the circulation.

Wake sheet– At 40 mm inboard from the center of the trailing vortex, the flow exhibits a distinctive imprint as a result of the wake that is shed by the passing rotor blade (figs. 23 and 24). As the flow is traversed in the vertical direction (+z), a strong positive perturbation in V_x clearly identifies the location ($z = 54$ mm) and width ($\Delta z = 25$ mm) of the wake sheet. During this excursion across the wake sheet, V_y and V_z both experience a decrease in magnitude; however, V_y shows a perturbation similar to that of V_x (but in the opposite direction), whereas the change in V_z is more nearly monotonic. The trend at 80 mm inboard from the center of the trailing vortex appears to be exactly the same (figs. 25 and 26) as at 40 mm.

Traversing the flow at distances further inboard from the trailing vortex ($y = 136$ mm and 192 mm) yields some distinct differences, especially in V_y and V_z (figs. 27–30). V_x continues to exhibit the familiar positive perturbation, but the width of the wake gradually increases with inboard distance. Furthermore, the magnitude of the velocity is higher at locations above the wake sheet where the flow may be starting to feel the effect of the wake that was shed from the previous blade. The shed wake that connects to the trailing vortex gradually increases in width when moving in an inboard direction; this increase is in keeping with the lower rotational speed of each blade section as the radius is decreased. The perturbation in V_y is decidedly less prominent than it was further outboard, and the magnitude is substantially higher at locations above the wake sheet than it is beneath. V_z is still somewhat monotonic, but the slope is now positive.

If the peak value of V_x is used as an indication of the vertical displacement of the wake behind the rotor blade, the wake is observed (fig. 31) to move upward (recall that the rotor thrust vector is down) at a somewhat linear pace with time and at a slightly higher rate along the more inboard locations. The rapid displacement of the wake sheet stands in contrast to the movement of the trailing vortex (fig. 32),

which has moved a comparatively short distance upwards and inboard during the interval of time that the rotor tip has advanced from 2.5 to 3.5 chord lengths past the measuring station.

Velocity Field

y-z plane– A more complete sense of the wake structure and the dominant character of the trailing vortex is provided by an organized set of velocity measurements obtained over a plane located behind the rotor blade (recall fig. 15). The results of the profile measurements (discussed earlier) revealed the extent of the wake, thereby enabling a significant reduction of the set of locations that needed to be surveyed. Topographical surfaces and contour maps were constructed from this set of data.

Guided by the appearance of the streamwise component of velocity, V_z, a concentrated zone of high velocity clearly exists near the center of the vortex (fig. 33). Whereas the flow in this zone (marked as region A in the figure) is directed toward the rotor blade, there is an equally concentrated region B (much weaker in magnitude) that is centered about 10 mm above this high-velocity zone that is directed in the opposite direction. The inboard portion of the wake shows that the flow is moving toward the rotor blade, forming a ridge of positive flow that diminishes in magnitude as it approaches the trailing vortex. Unlike many classical models of the wake that illustrate an endless spiral into a line vortex, the surface and contour plots both suggest a rapid accretion of the wake by the trailing vortex. The ridge of positive wake flow appears to pass just outside (or encircle) a negative flow region (marked as region B in the figure) as it merges with the trailing vortex.

The time rate of change of the streamwise velocity component, $\partial V_x/\partial t$, gives some indication of how the wake is moving (fig. 34). The surface plot reveals that the wake sheet is moving upwards (+z direction). This observation is based on knowing that the wake flow is positive (recall fig. 33) and noting that the velocity is increasing (positive derivative) along the uppermost z locations compared to the opposite behavior at the lower z locations. There is no significant change in the negative velocity zone (region B) that is encircled by the wake flow that is merging with the trailing vortex. The region of peak positive velocity within the trailing vortex is moving upwards (+z) and inboard (+y), along a path that is perhaps more clearly evident in the contour map (direction of movement denoted by an arrow in the figure).

To determine the spatial variation of the velocity field from the inertially fixed LV measurements, it is necessary to draw on the Taylor hypothesis (see summary in ref. 16). The local-flow region is assumed to be comparatively "frozen" within a control volume that is moving with a given velocity past the measurement location. If the velocity of the control volume is large and the time rate of change of a given quantity is small relative to the convected volume, then the temporal and spatial derivatives relative to an inertial frame are related by:

$$\frac{\partial}{\partial x} = -\frac{1}{\Omega(R-y)}\frac{\partial}{\partial t} \tag{15}$$

Equation (15) gives the streamwise derivative of the streamwise component of velocity, $\partial V_x/\partial x$, over the y-z plane located three chord lengths behind the rotor blade (fig. 35). Comparing these results with the velocity field shown in figure 33 shows that, as the rotor blade is approached (+x direction), the regions of high and low velocity within the trailing vortex become more pronounced and the

streamwise component of velocity within the wake sheet increases (more closely matching the speed of the rotor blade).

The most familiar flow pattern produced by the trailing vortex is revealed by the cross-flow components of velocity in the y-z plane, V_y and V_z. The vector sum of these two velocity components, $V_y + V_z$, not only shows the circulatory nature of the flow in this plane, but it also shows the general downwash and inboard direction of flow over the remainder of the wake sheet (fig. 36).

x-z plane– The development of the velocity profiles across the shed wake is best viewed in a plane that is normal to the span of the rotor blade. In fact, planes at several y locations (recall the z-axis surveys shown in fig. 15) are generated during the interval of time it takes for the tip of the rotor blade to move a distance of 1 chord.

Beginning with the plane at y = 40 mm, the velocity components are shown at three instants of time along with relatively smooth curves obtained from spline fits to the data (fig. 37). The resulting surface in the t-z plane is shown in figure 38. The smoothing process results in a far-less-erratic surface (compare with fig. 23) while qualitatively retaining the behavior of the original data. Similar curve fits and surface plots are constructed for t-z planes at the remaining three y locations (figs. 39–44).

During the time that the rotor tip moves a distance of 1 chord length from 2.5c to 3.5c, the relationship between t and x at each of the y locations is given by:

$$t = t_{min} + \left(\frac{n-1}{N-1}\right)(t_{max} - t_{min}) \tag{16}$$

and

$$\bar{x} = 3c + \left(\frac{R-y}{R}\right) c \left(\frac{2n-N-1}{2N-2}\right) \tag{17}$$

where N denotes the total number of time steps selected for dividing up the time interval, and $\bar{x}$, parallel to x, is the distance downstream from the trailing edge of the rotor blade. In other words, when the line of measurements is 3 chords downstream, $\bar{x}$ = 3c-x. Hence, expressions (16) and (17) define the correspondence between the t-z plane and the x-z plane (which is the same as the $\bar{x}$-z plane).

The magnitude and path of the wake sheet that is shed from the rotor can be readily identified by examining the resulting series of velocity profiles obtained from the vector sum of V_x and V_z (figs. 45–48). There is an apparent increase in the width of the wake that occurs in the inboard direction (with increasing y). The rate at which the wake is moving normal to the plane of the rotor can be quantified by using the maximum value of V_x as an indication of the vertical displacement of the wake at each $\bar{x}$ location. The dashed line appearing in each of the figures defines the vertical position, z, of the wake over a calculated range of streamwise locations, $\bar{x}$, that corresponds to the x-z plane at each particular y location. In other words, these figures show what the wake would look like in each of the x-z planes when the tip of the rotor blade is 3 chord lengths beyond the center of the profile sweep ($\bar{x}$ = 573 mm). The slope of the wake, $dz/d\bar{x}$, presented in figure 49, shows that the wake is moving upwards more rapidly at the more inboard locations.

Vorticity Field

After an orthogonal set of velocity components over an evenly distributed array of locations in the y-z plane is obtained, the local streamwise component of vorticity, ω_x, can be calculated from:

$$\omega_x = \Gamma_x / area = \underbrace{\oint}_{ccw} (V_y dy + V_z dz)/\Delta y \Delta z \qquad (18)$$

The results for the plane that intersects the rotor wake after the rotor blade has advanced a distance of three chord lengths show a sizable concentration of vorticity within the trailing vortex (fig. 50); the maximum value for an integration cell reaches 11.7/sec. A small amount of vorticity that remains outside the trailing vortex is spread along the wake sheet for some distance beyond the inboard boundary of the measurement grid. Summing all the calculated streamwise vorticity on this measurement grid during the time it takes for the rotor tip to move 1 chord length shows that vorticity is continuing to migrate along the sheet toward the trailing vortex (fig. 51).

The spanwise component of vorticity, ω_y, over the x-z plane can be calculated by first considering the velocity components, V_x and V_z, at each location during the time interval of interest. Some degree of smoothness in the vorticity is achieved by dividing the time interval into equal increments and obtaining cubic-spline approximations for the variation of each velocity component along the z direction (recall fig. 37). The variable t is replaced by $\bar{x}$ according to equations (16) and (17). The spanwise vorticity over planes that are at different distances from the trailing vortex is shown in figures 52 to 55. The center of the wake deficit, based on the velocity profiles presented in figures 45 to 48, is also included (represented by a heavy dashed line). The results indicate that the sign of the vorticity changes between the two sides defined by the centerline of the wake. The upper side of the wake adjacent to the centerline is negative, and the lower side is positive. These vorticity orientations are consistent with the vorticity produced in the boundary layer on the upper and lower surfaces of the rotor blade. These patterns appear to be repeated in figure 54 at a location that is about 60 mm higher along the z-axis, suggesting the presence of the wake from the preceding rotor blade.

CONCLUSIONS

1. The position of the trailing vortex meanders less than 1 core diameter in the near wake behind the rotor blade (at 3c). However, meandering increases by an order of magnitude by the time the vortex age has reached $\Psi = 180$ deg.

2. The maximum circulatory velocity within the trailing vortex reaches about 31 percent of the rotor-tip speed. This value is probably low because of vortex meandering during the statistical average.

3. The results obtained at different rotor speeds and at different vortex ages (within 3 chords of the blade) show that the core size remains the same (20 mm or 10 percent of the chord). However, the vorticity appears to extend over a larger region (an increasing distance beyond the core boundaries) as the vortex ages.

4. Lowering the rotor speed does not change the general appearance of the trailing relative to the rotor-tip speed.

5. The shed wake that connects to the trailing vortex is about 25 mm wide. The width of the wake gradually increases along an inboard direction, in keeping with the lower rotational speed of each blade section as the radius is decreased.

6. Unlike many classical models of the wake that illustrate an endless spiral into a line vortex, the present data suggest a rapid accretion of the wake by the trailing vortex.

7. A sizable concentration of vorticity occurs within the trailing vortex at $\Psi = 29$ deg. The small amount of vorticity that remains outside the trailing vortex is distributed along the wake sheet, and it continues to migrate toward the trailing vortex.

8. The spanwise-oriented vorticity changes sign across the two sides defined by the centerline of the wake. These vorticity orientations are consistent with the signs of the vorticity produced in the boundary layer on the upper and lower surfaces of the rotor blade.

REFERENCES

1. Wu, J. C.; Hackett, J. E.; and Lilley, D. E.: A Generalized Wake-Integral Approach for Drag Determination in Three-Dimensional Flows. AIAA Paper 79-0279, Presented at the 17th Aerospace Sciences Meeting, New Orleans, La., Jan. 1979.

2. Hackett, J. E.; and Sugavanam, A.: Recent Developments in Three-Dimensional Wake Analysis. AGARD Report 723, Aircraft Drag Prediction and Reduction, 1985.

3. Anderson, J. D., Jr.: Introduction to Flight., McGraw-Hill, Book, Co.,, Inc., 1978, pp. 145–188.

4. Bertin, J. J.; and Smith, M. L.: Aerodynamics for Engineers. Prentice-Hall, Inc., 1979, pp. 163–169.

5. Betz, A.: Ein Verfahren zur Direkten Ermittlung des Profilwiderstandes. ZFM vol. 16, pp. 42–44, 1925 (also see Schlichting, H.: Boundary Layer Theory. McGraw-Hill Book Co., Inc., Feb. 1960, pp. 615–618).

6. Maskell, E. C.: Progress Towards a Method of Measurement of the Components of the Drag of a Wing of Finite Span. Royal Aircraft Establishment RAE-TR-72232, 1979.

7. Thompson, T. L.; Komerath, N. M.; and Gray, R. B.: Visualization and Measurement of the Tip Vortex Core of a Rotor Blade in Hover. J. Aircraft, vol. 25, no. 12, 1988, pp. 1113–1121.

8. Caradonna, F. X.; and Tung, C.: Experimental and Analytical Studies of a Model Helicopter Rotor in Hover. Vertica, vol. 5, no. 2, 1981, pp. 149–161.

9. Tung, C.; Pucci, S. L.; Caradonna, F. X.; and Morse, H. A.: The Structure of Trailing Vortices Generated by Model Rotor Blades. Vertica, vol. 7, no. 1, 1983, pp. 33–43.

10. Cook, C. V.: The Structure of the Rotor Blade Tip Vortex. AGARD-CP-111, 1973.

11. Pouradier, J. M.; and Horowitz, E.: Aerodynamic Study of a Hovering Rotor. Vertica, vol. 5, no. 4, 1981, pp. 301–315.

12. Plantin de Hugues, P.: Etude du Systeme Tourbillonnaire Genere en Extremite de Pale d'un rotor d'Helicoptere en vol Stationnaire. These de Doctorat, Universite d'Aix-Marseille II, IMFM, 1991.

13. Tangler, J. L.: Experimental Investigation of the Subwing Tip and Its Vortex Structure. NASA CR-3058, 1978.

14. Muller, R. H.: Measurement of Helicopter Rotor Tip Vortices Using the “Flow Visualization Gun” Technique. AAAF 18th European Rotorcraft Forum, Paper 82, Avignon, France, Sept. 1992.

15. Boatwright, D. W.: Measurements of Velocity Components in the Wake of a Full-Scale Helicopter Rotor in Hover. USAAMRDL TR 72-33, 1972.

16. Zaman, K. B. M. Q.; and Hussain, A. K. M. F.: Taylor Hypothesis and Large-Scale Coherent Structures. J. Fluid Mech., vol. 112, 1981, pp. 379–396.

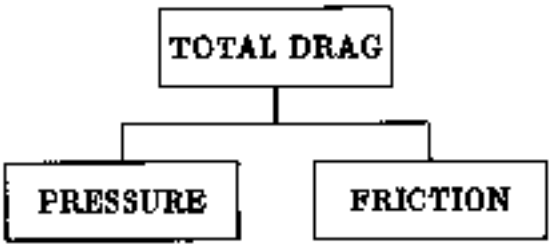

Figure 1. Basic composition of drag.

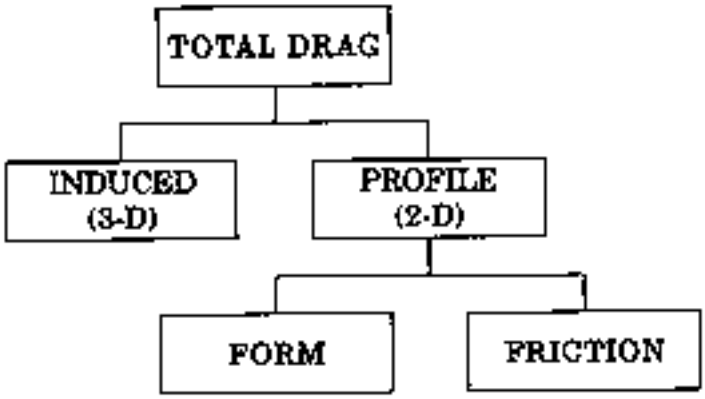

Figure 2. Conventional designation of drag elements for 3-D lifting bodies.

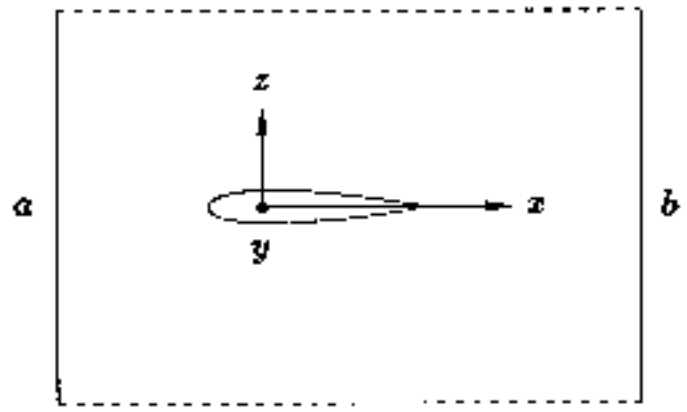

Figure 3. Control volume for determining drag.

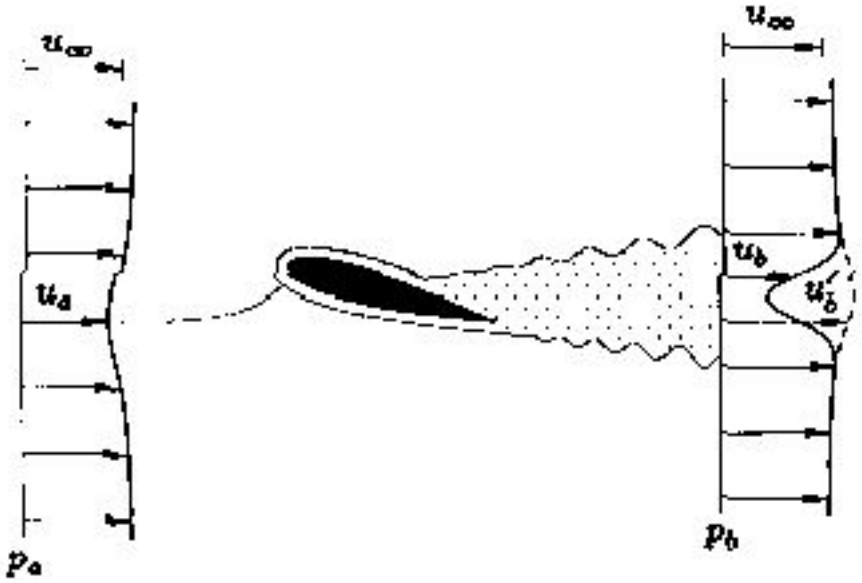

Figure 4. Wake model originally introduced by Betz (ref. 5).

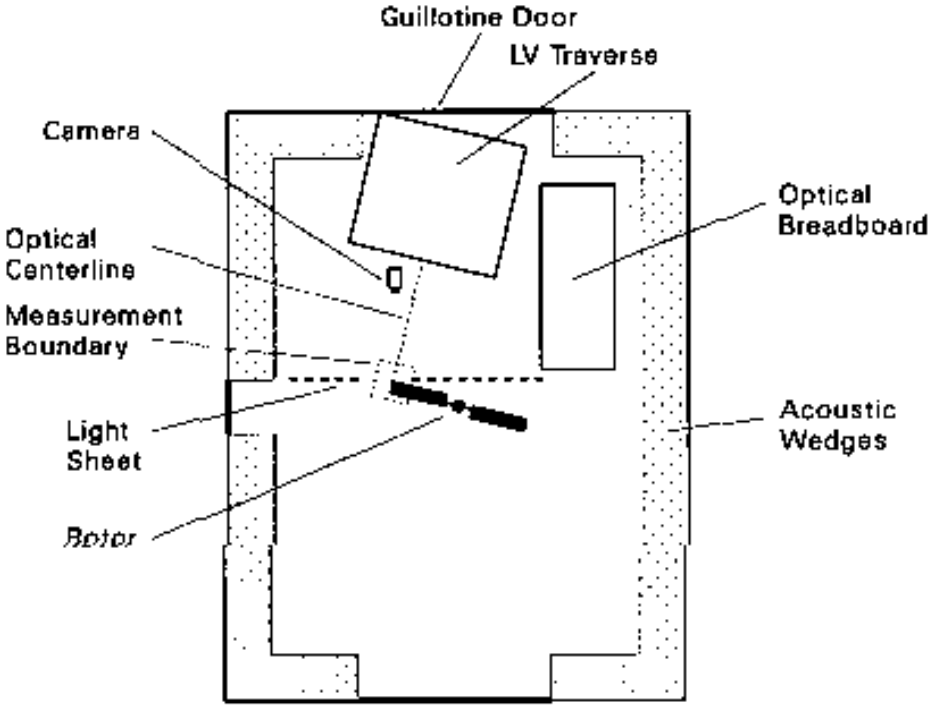

Figure 5. Location of rotor and equipment in chamber of Hover Test Facility.

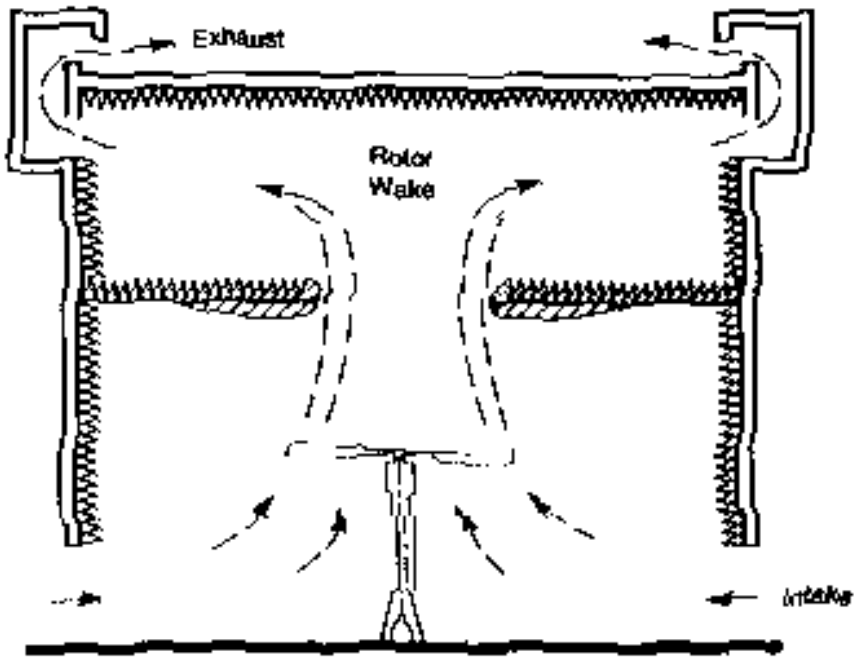

Figure 6. Direction of air flow through chamber of Hover Test Facility.

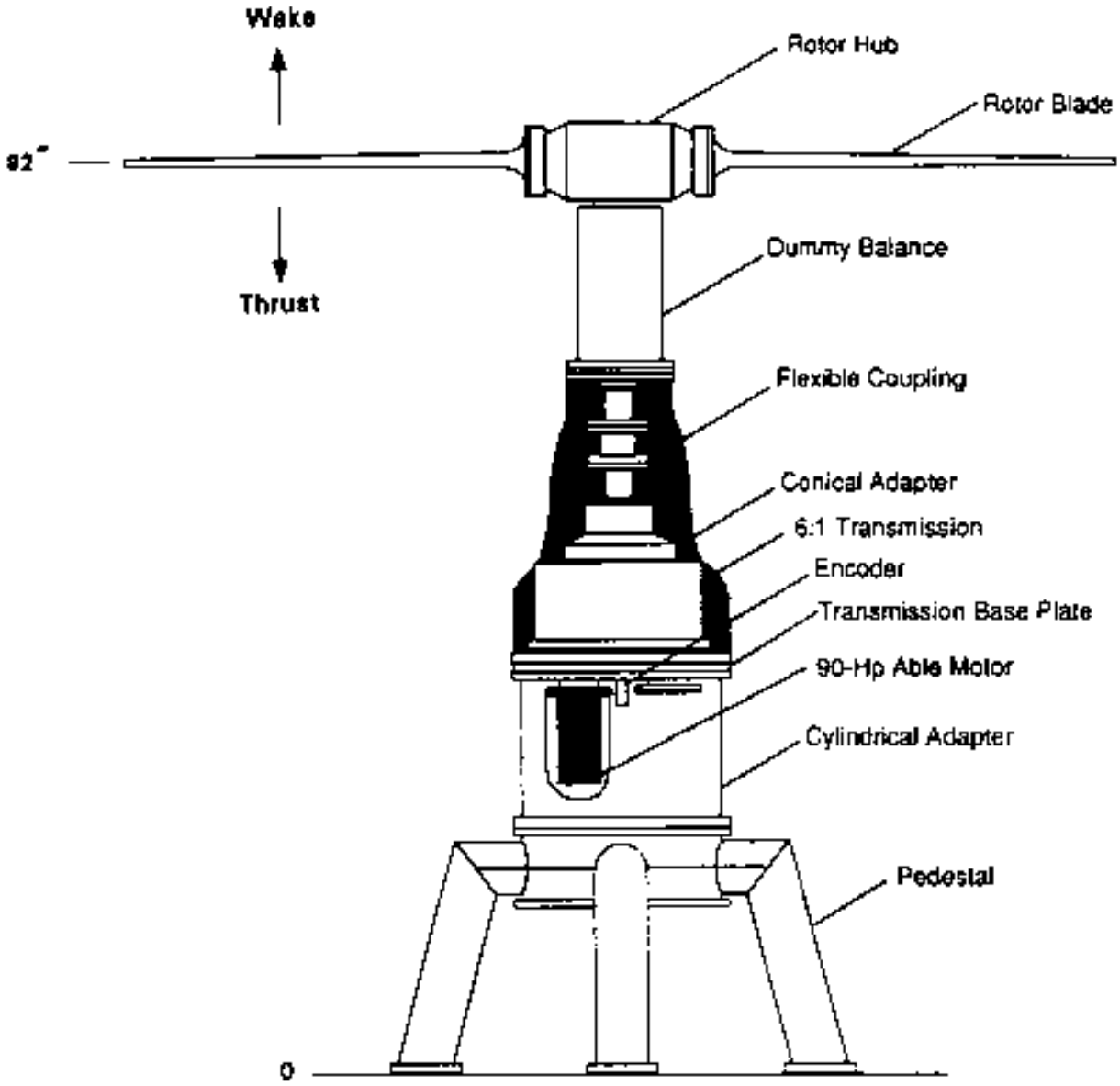

Figure 7. Test stand for hovering rotor experiment.

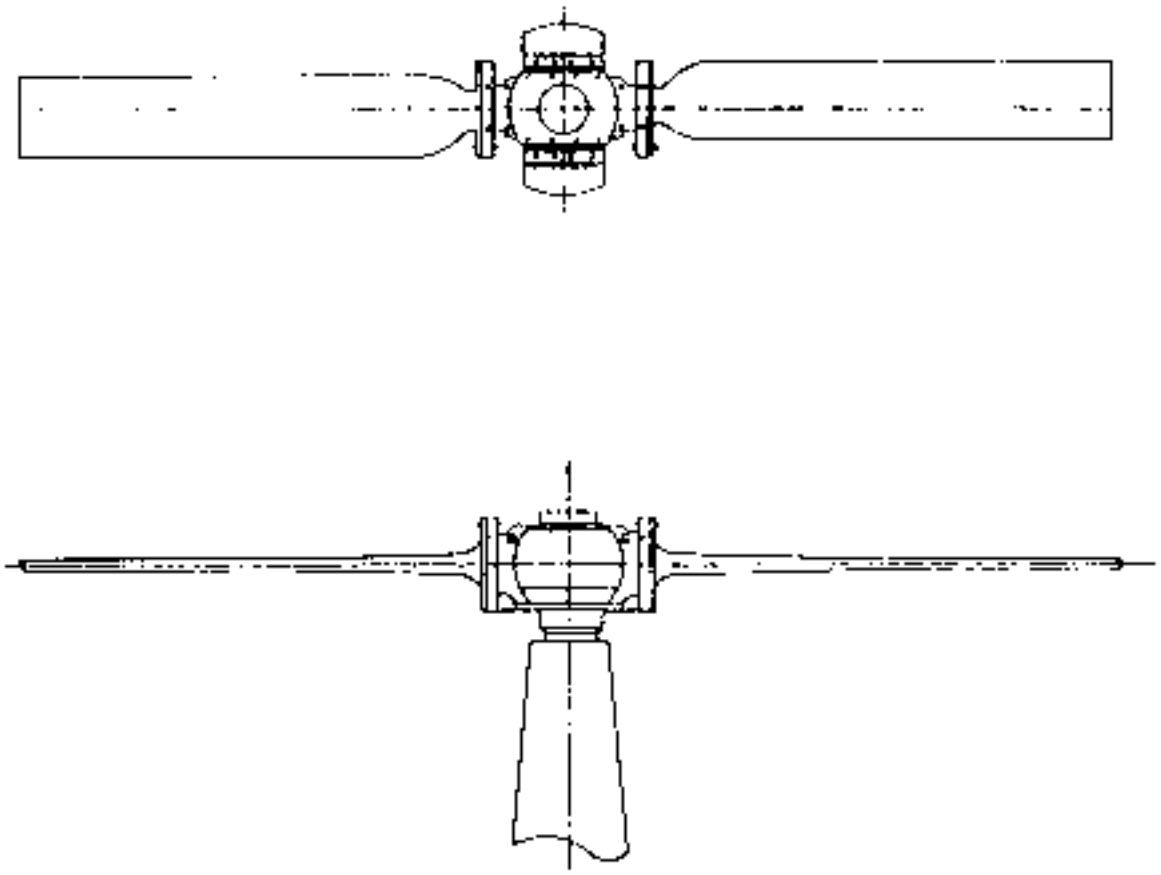

Figure 8. Rotor hub and blade assembly.

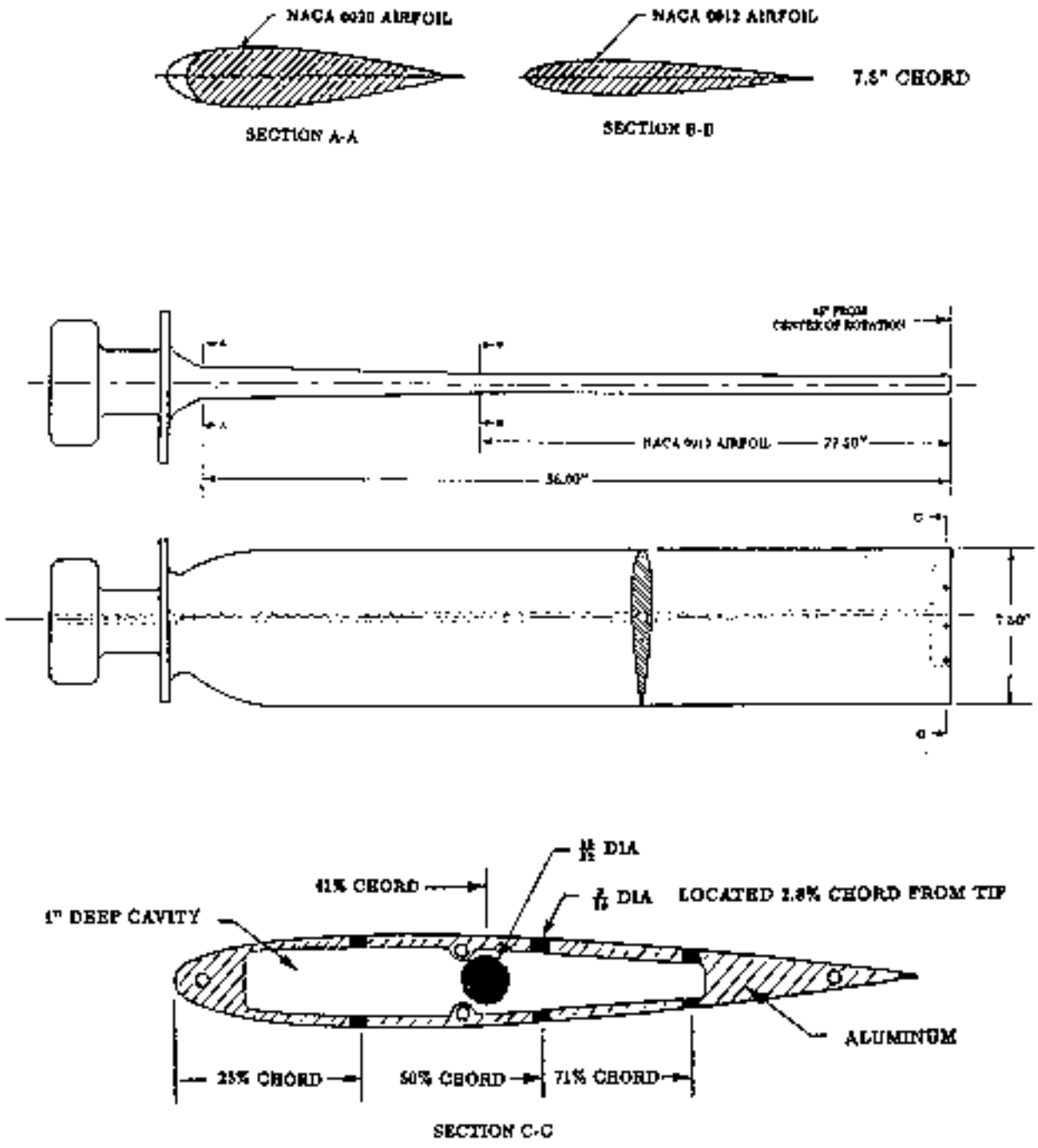

Figure 9. Rotor blade with radial passage and tip plenum for seed particles.

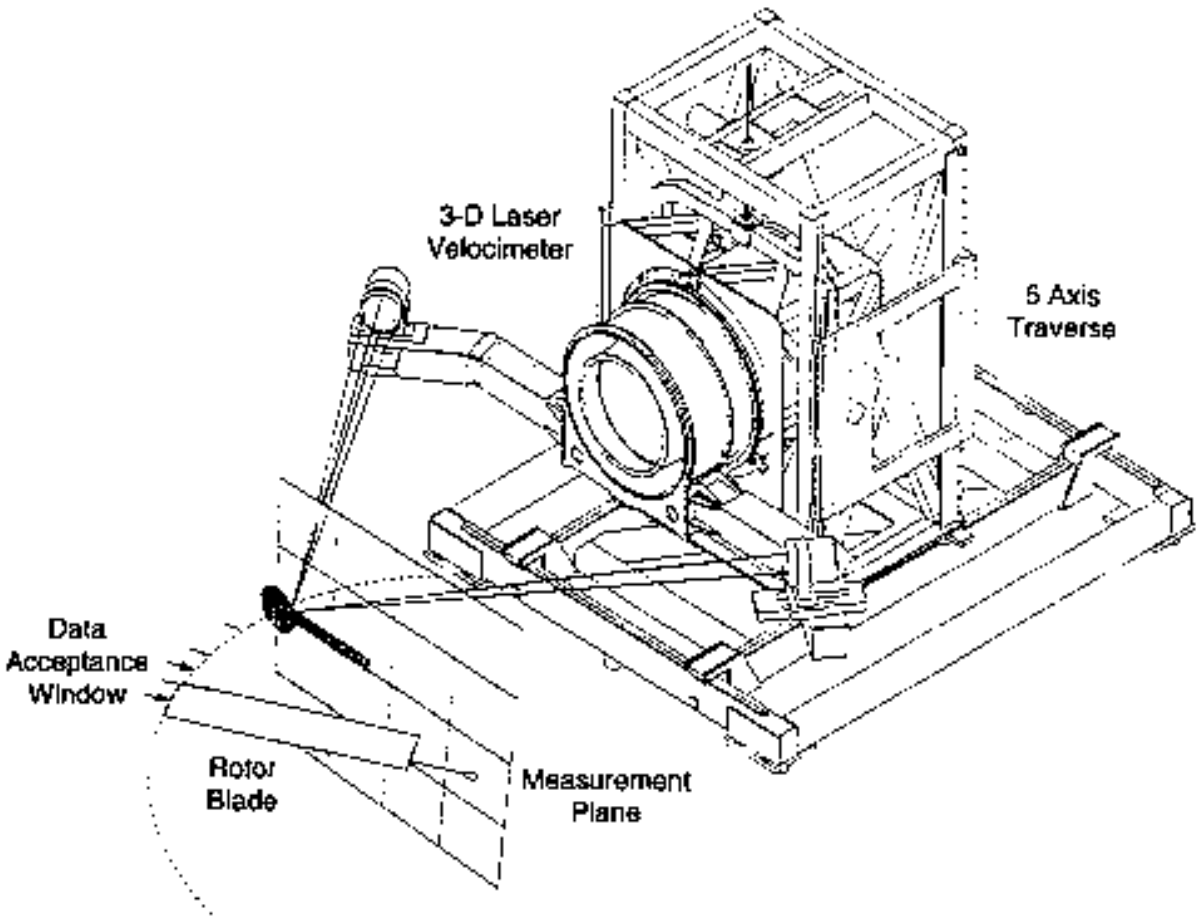

Figure 10. LV setup and measurement field relative to rotor blade.

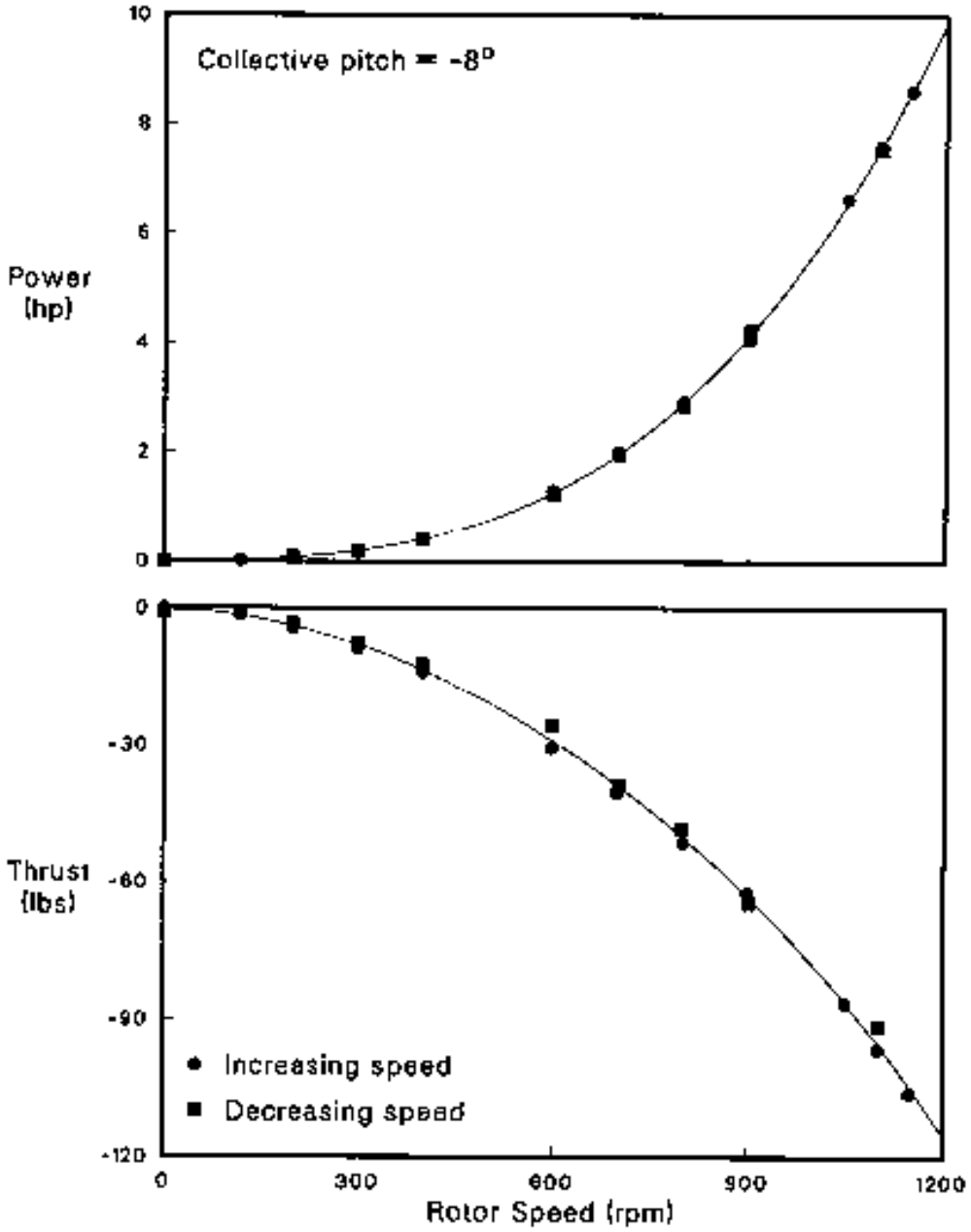

Figure 11. Balance measurements of thrust and power with the collective pitch of the rotor set at –8 deg.

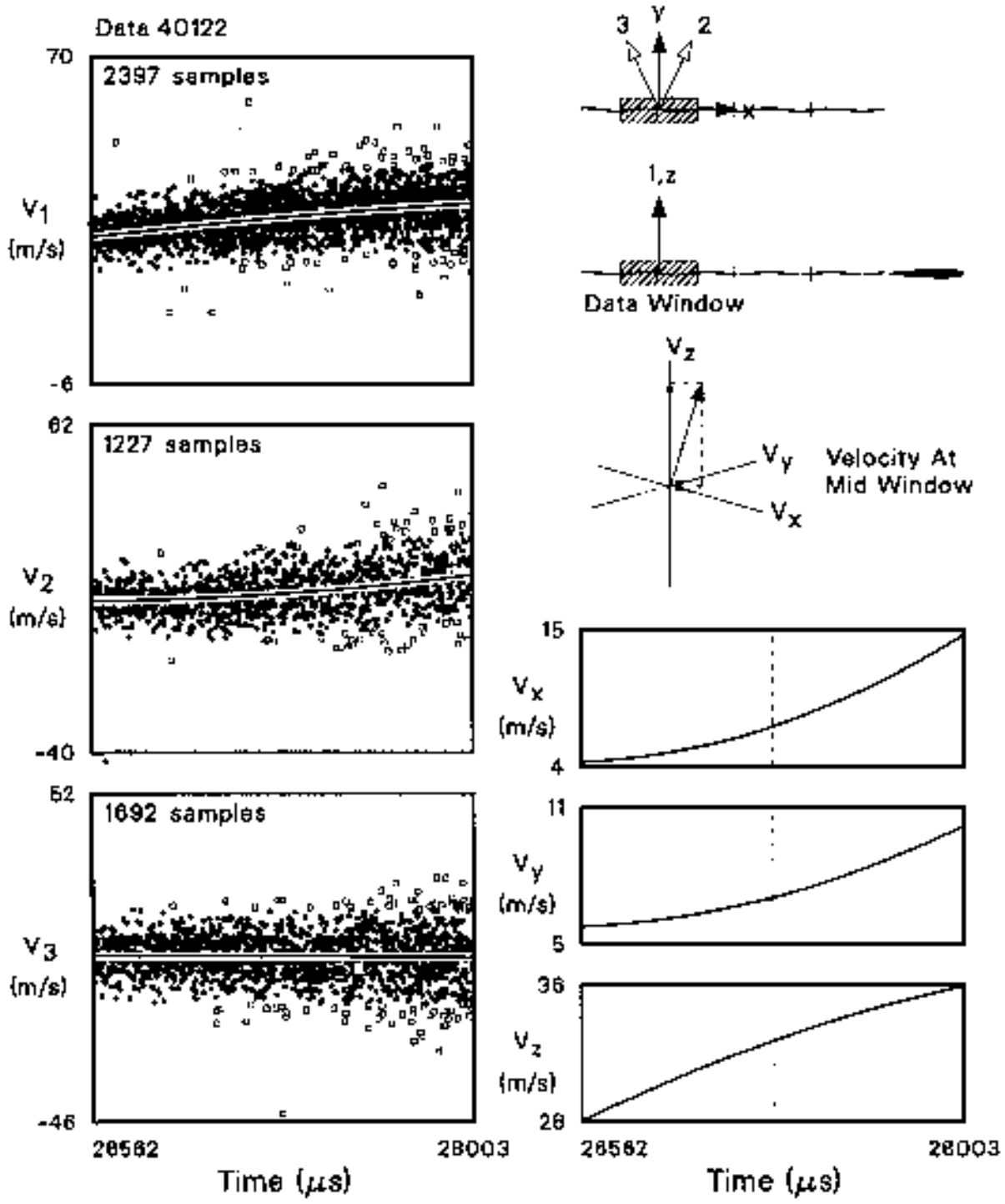

Figure 12. Example of data collected during a finite time window as the rotor blade moved from 2.5 to 3.5 chord lengths beyond the measurement location. Orthogonal coordinate transformations are based on least-squares spline fits to data with <2 rms deviation (solid symbols) from the uncensored curve fit (not shown).

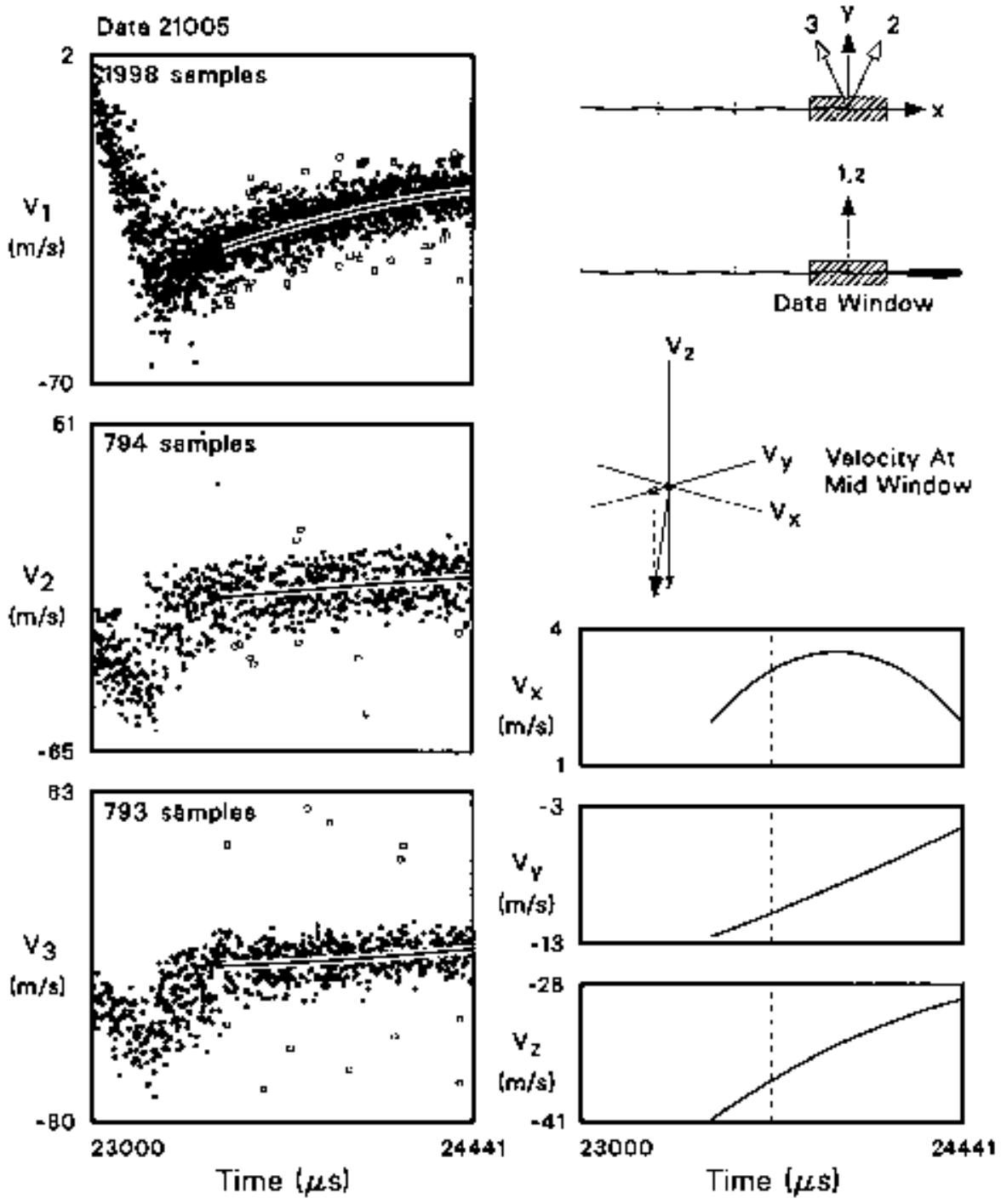

Figure 13. Example of particle dynamics and the restriction on the range of the curve fit in the region immediately following the passage of the rotor blade past the measurement location.

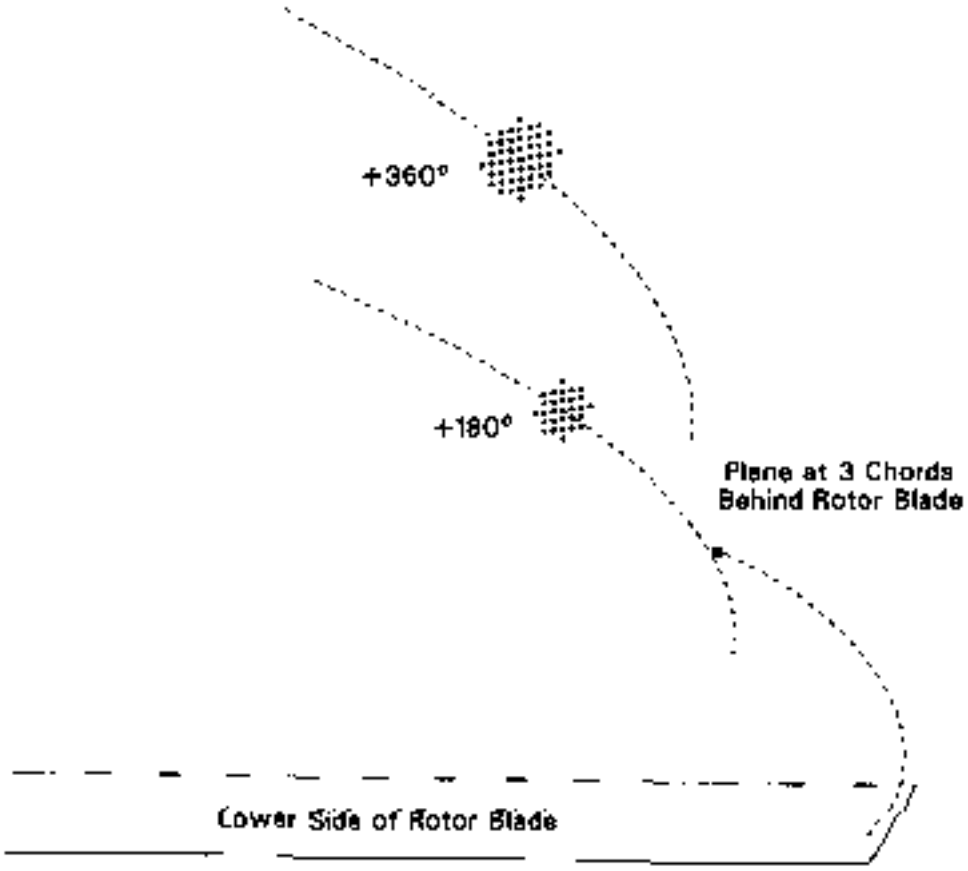

Figure 14. Qualitative rendering of trailing-vortex meander at different azimuthal positions in the rotor wake.

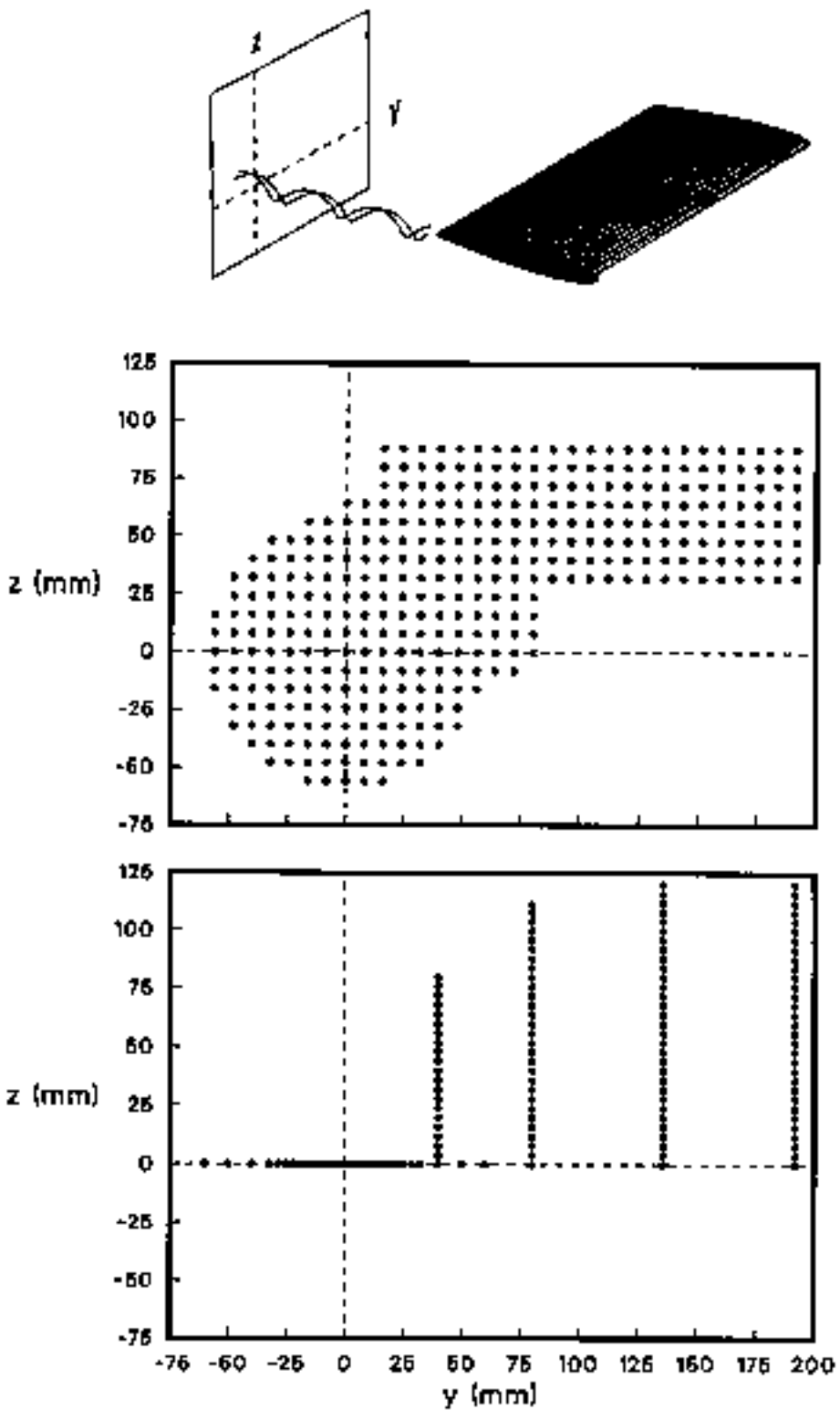

Figure 15. Measurement locations over the y-z plane in the wake of the rotor blade. The approximate center of the trailing vortex defines the (0,0) position.

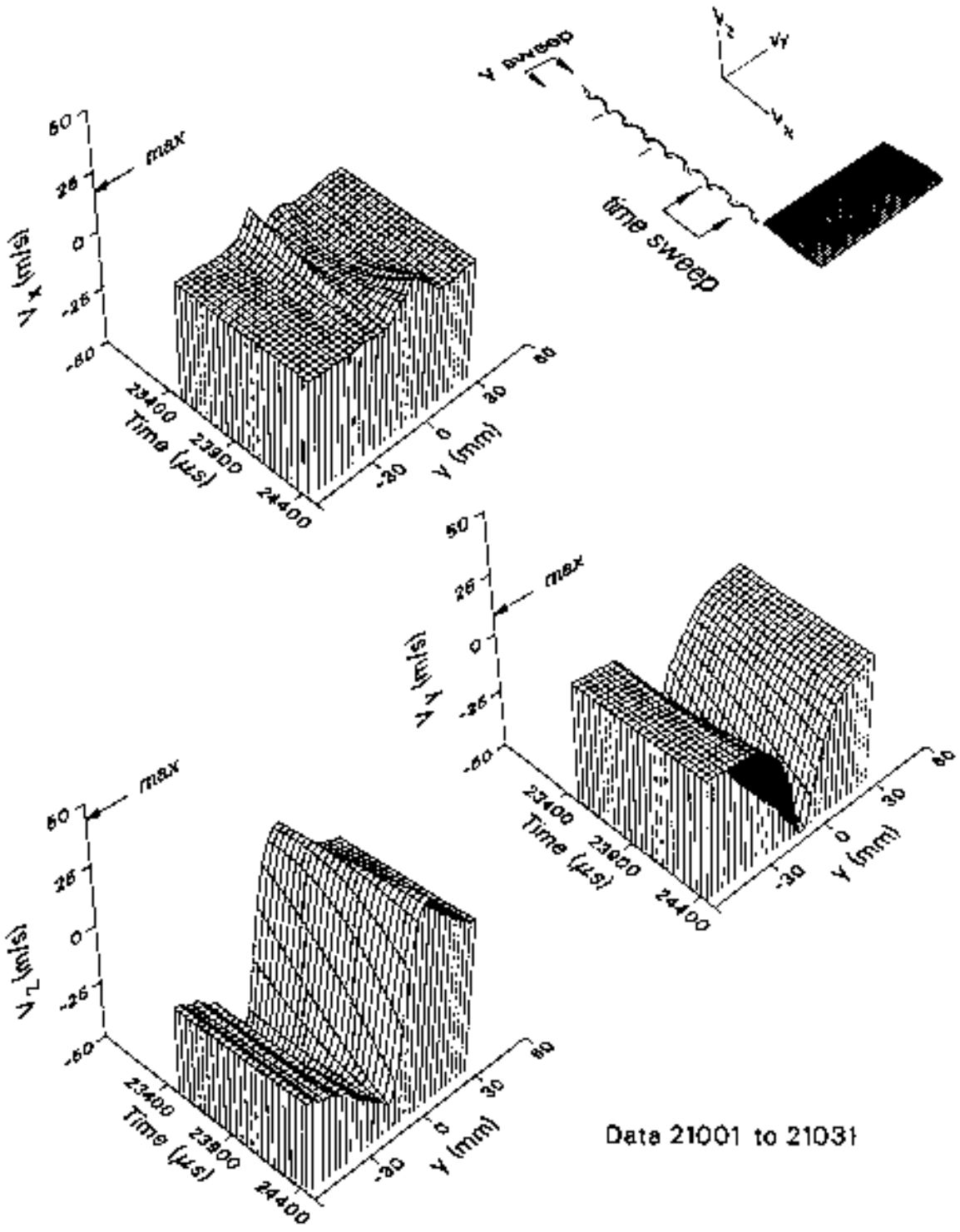

Figure 16. Velocity components along a horizontal sweep across the trailing vortex as the tip of the rotor blade moved from 0.3 to 1.0 chord lengths past the measurement location. The rotor speed was 1100 rpm.

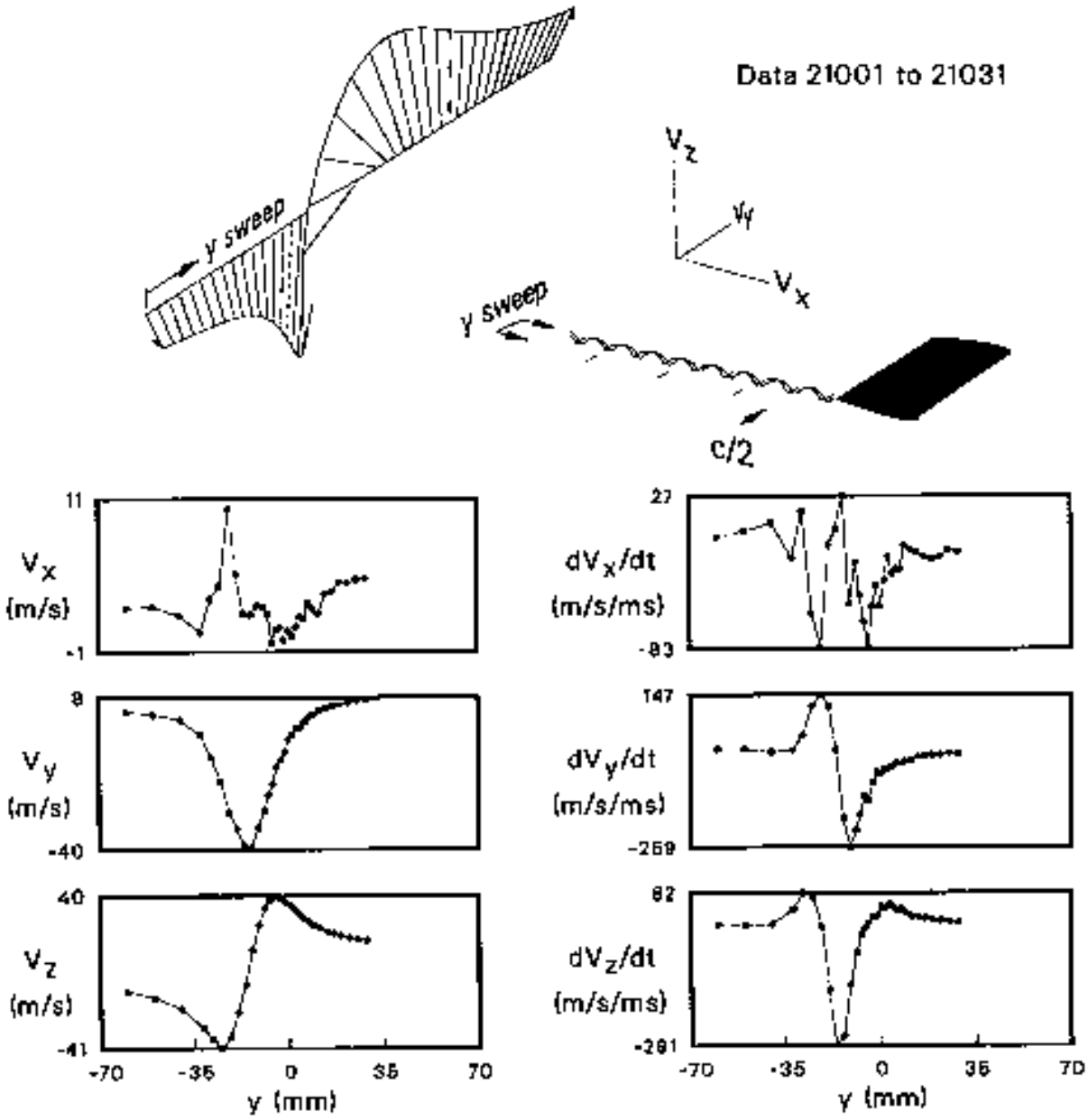

Figure 17. Velocity components along a horizontal sweep across the trailing vortex after the blade tip moved forward 0.5 chord length. The rotor speed was 1100 rpm.

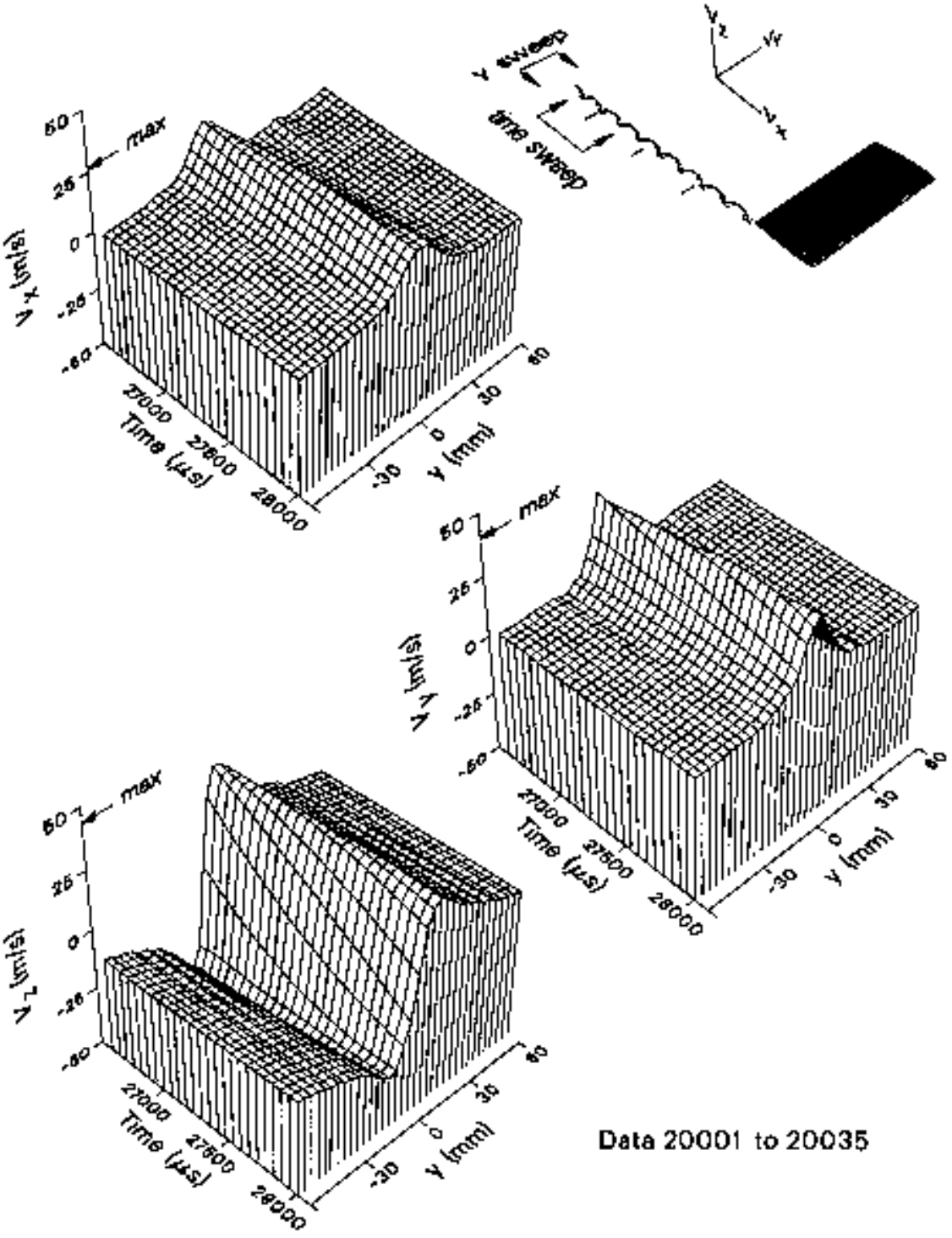

Figure 18. Velocity components along a horizontal sweep across the trailing vortex as the tip of the rotor blade moved from 2.5 to 3.5 chord lengths past the measurement location. The rotor speed was 1100 rpm.

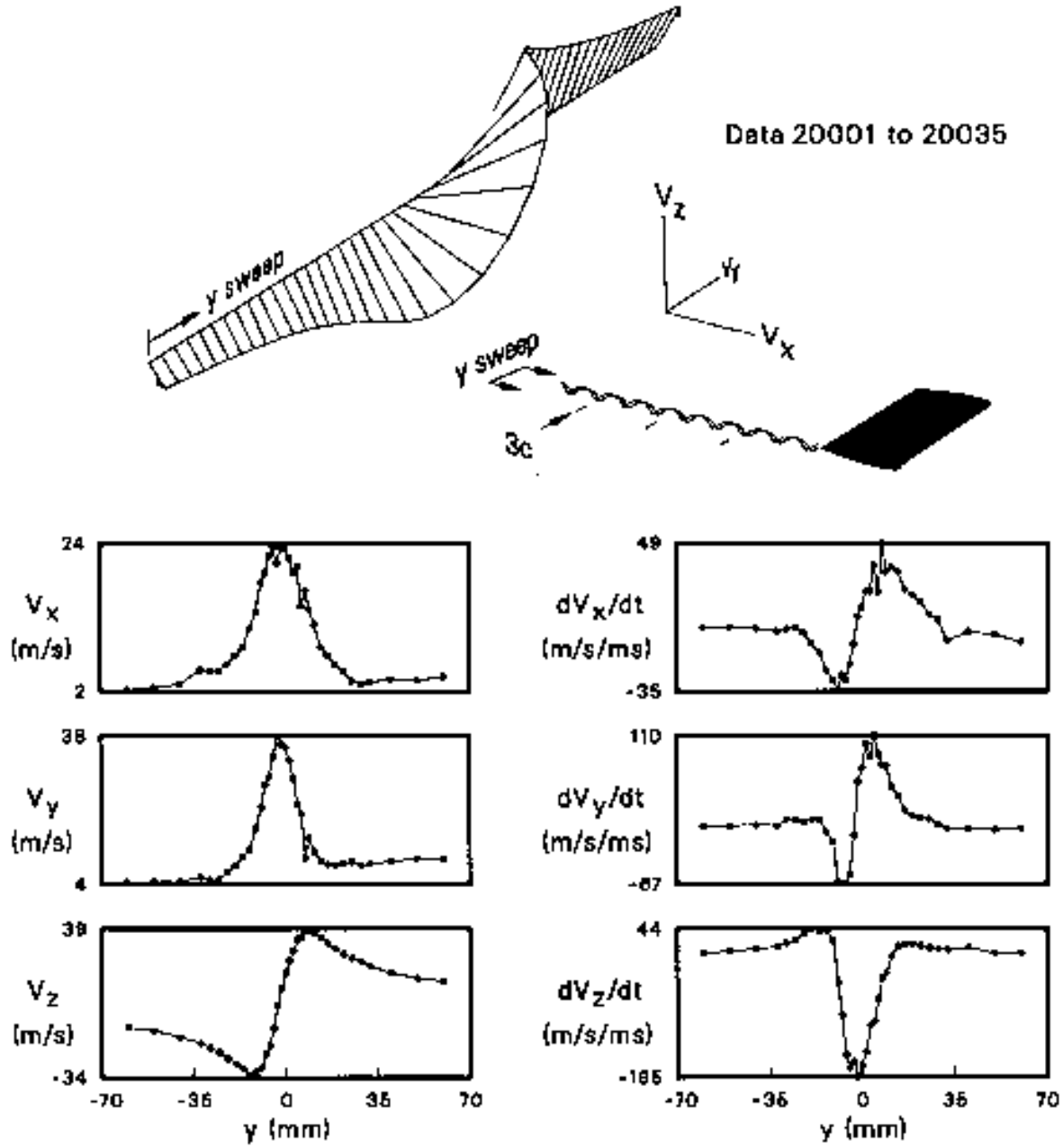

Figure 19. Velocity components along a horizontal sweep across the trailing vortex after the blade tip moved forward 3 chord lengths. The rotor speed was 1100 rpm.

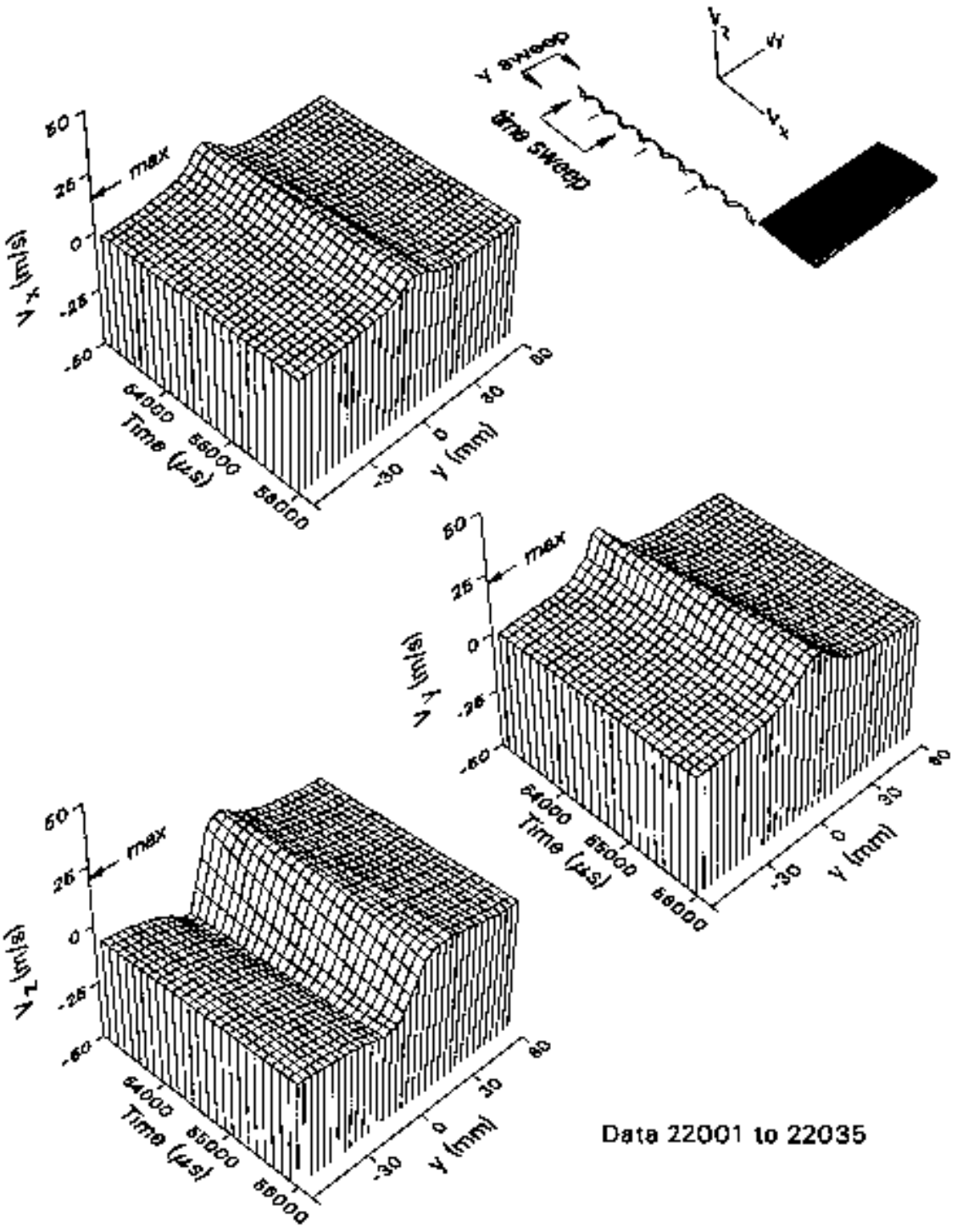

Figure 20. Velocity components along a horizontal sweep across the trailing vortex as the tip of the rotor blade moved from 2.5 to 3.5 chord lengths past the measurement location. The rotor speed was 550 rpm.

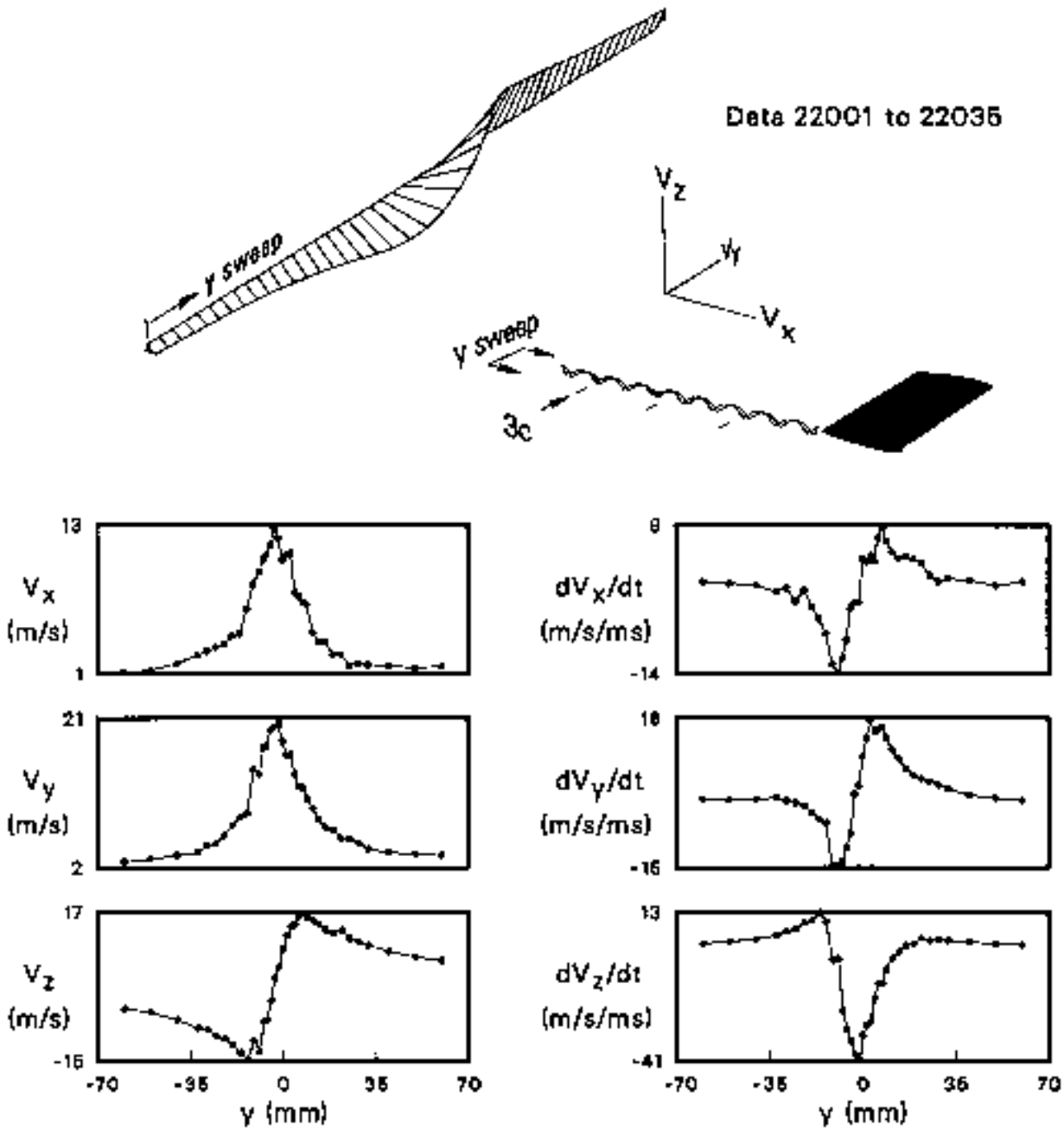

Figure 21. Velocity components along a horizontal sweep across the trailing vortex after the blade tip moved forward 3 chord lengths. The rotor speed was 550 rpm.

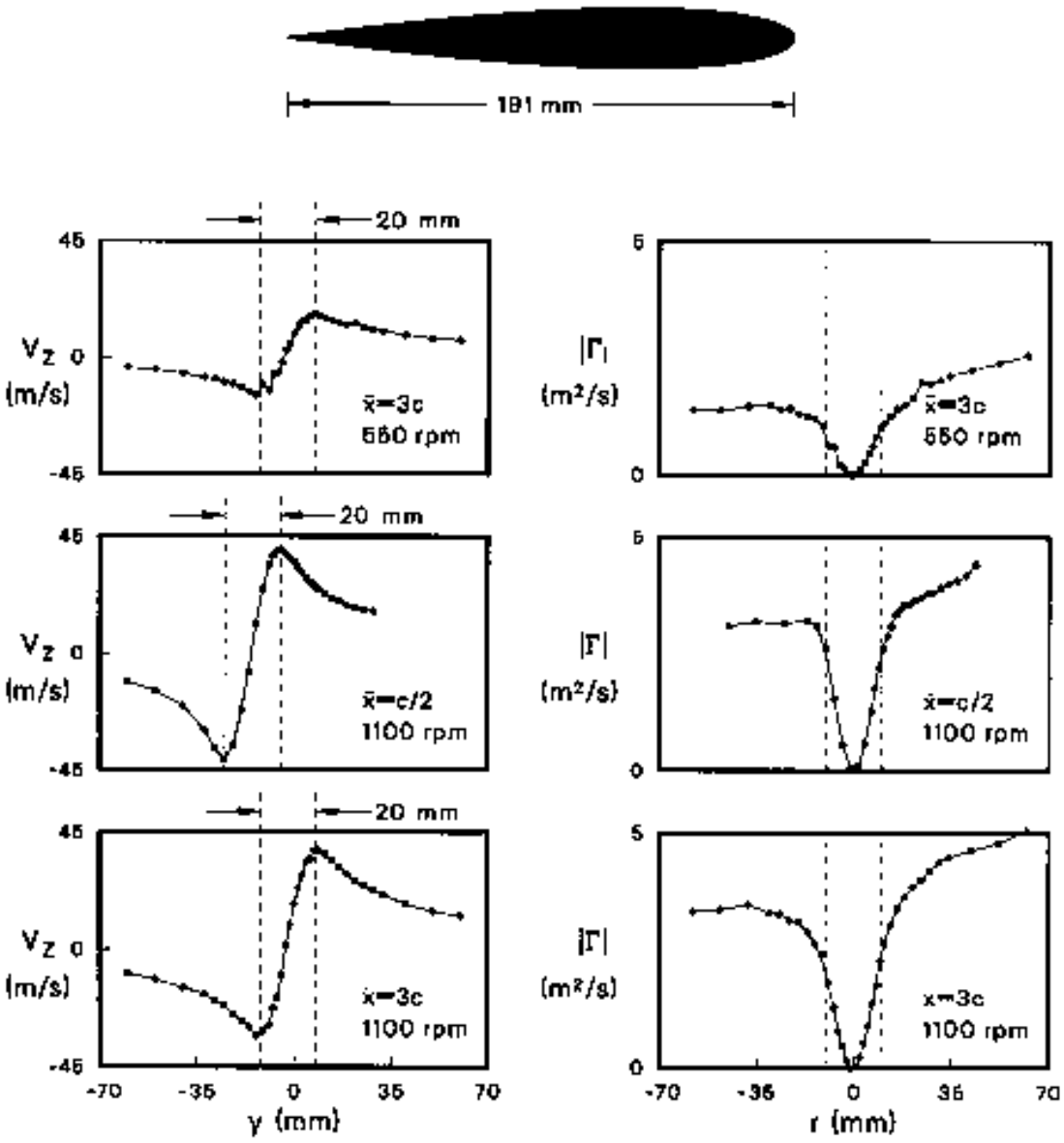

Figure 22. Vertical velocity component (V_Z) and circulation (Γ) along horizontal sweeps across the trailing vortex. The approximate center of the vortex when $\bar{x}$ = 3c and the tip speed was 1100 rpm defines the y = 0 position. The distance r is measured from the calculated center of the vortex.

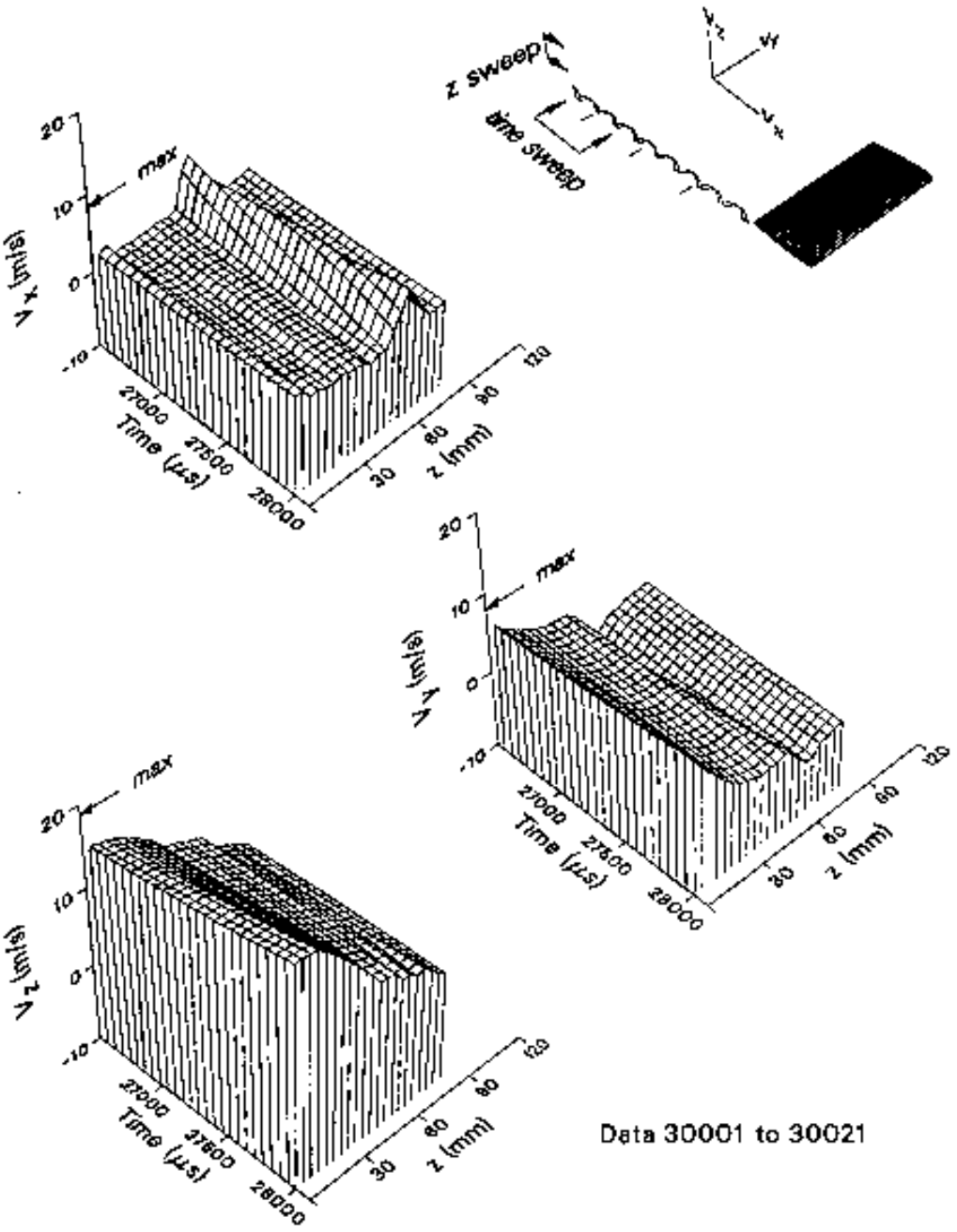

Figure 23. Velocity components along a vertical sweep across the wake at y = 40 mm as the tip of the rotor blade moved from 2.5 to 3.5 chord lengths past the measurement location. The rotor speed was 1100 rpm.

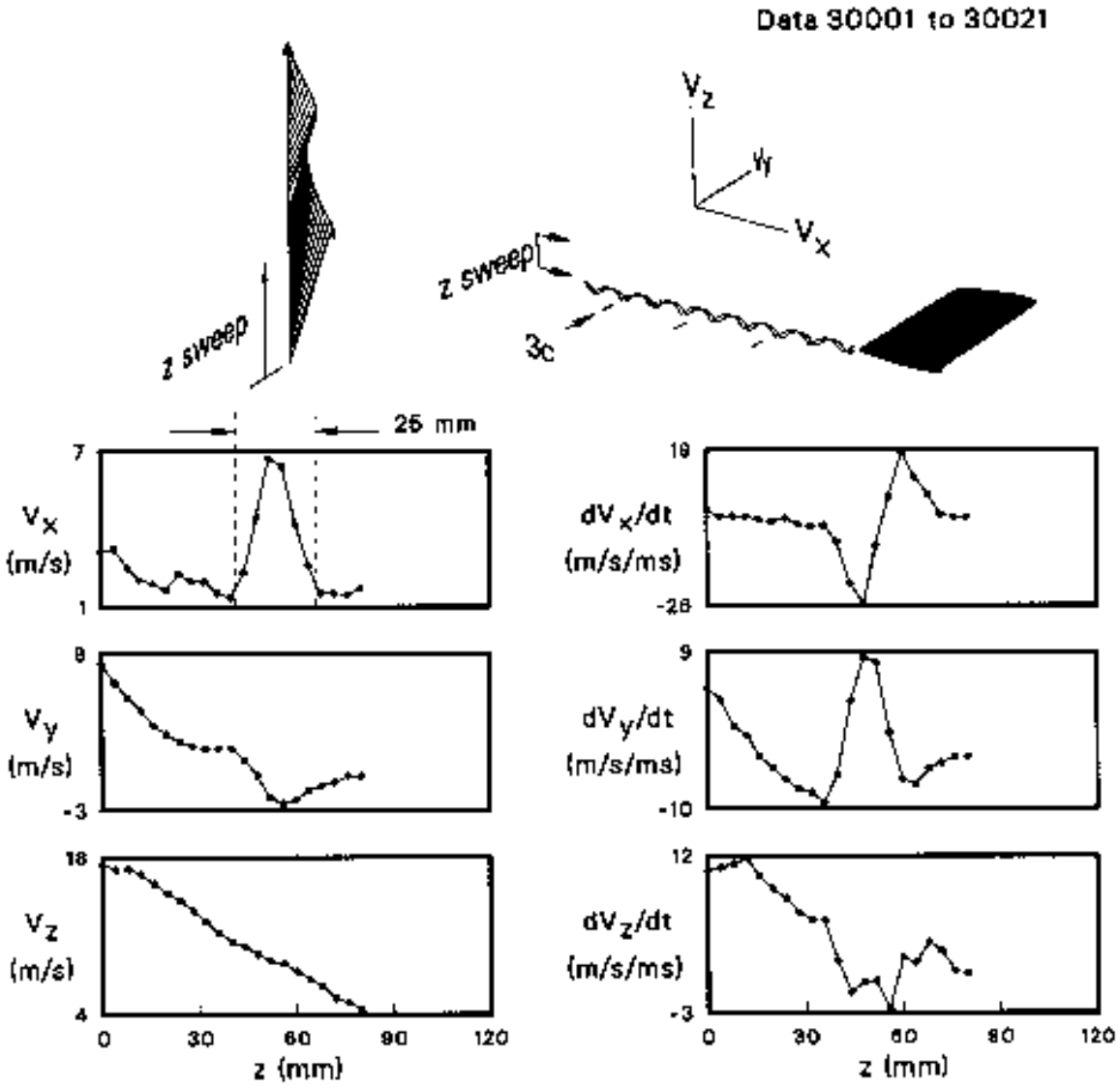

Figure 24. Velocity components along a vertical sweep across the wake at y = 40 mm inboard from the rotor tip and after the blade tip moved forward 3 chord lengths. The rotor speed was 1100 rpm.

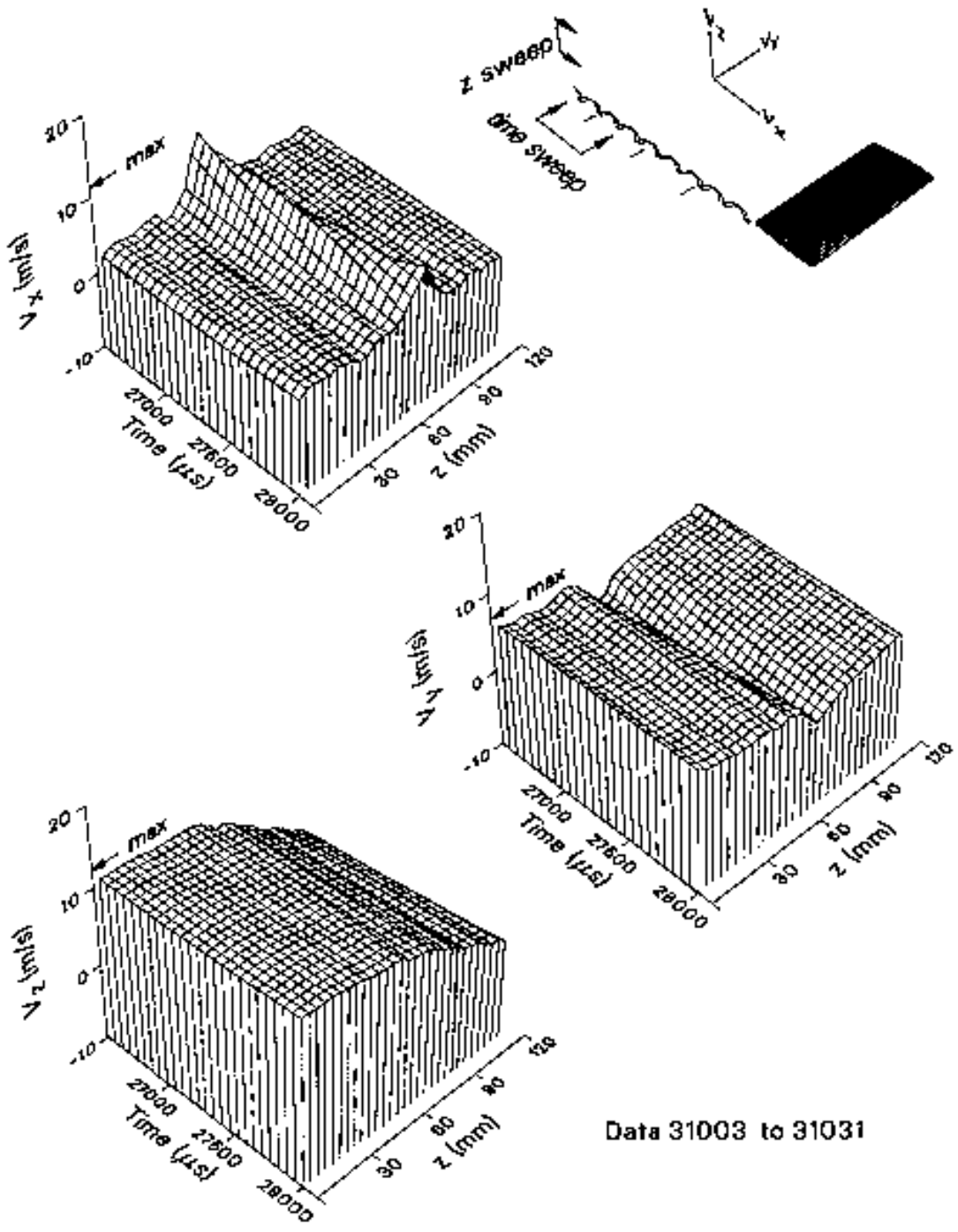

Figure 25. Velocity components along a vertical sweep across the wake at y = 80 mm as the tip of the rotor blade moved from 2.5 to 3.5 chord lengths past the measurement location. The rotor speed was 1100 rpm.

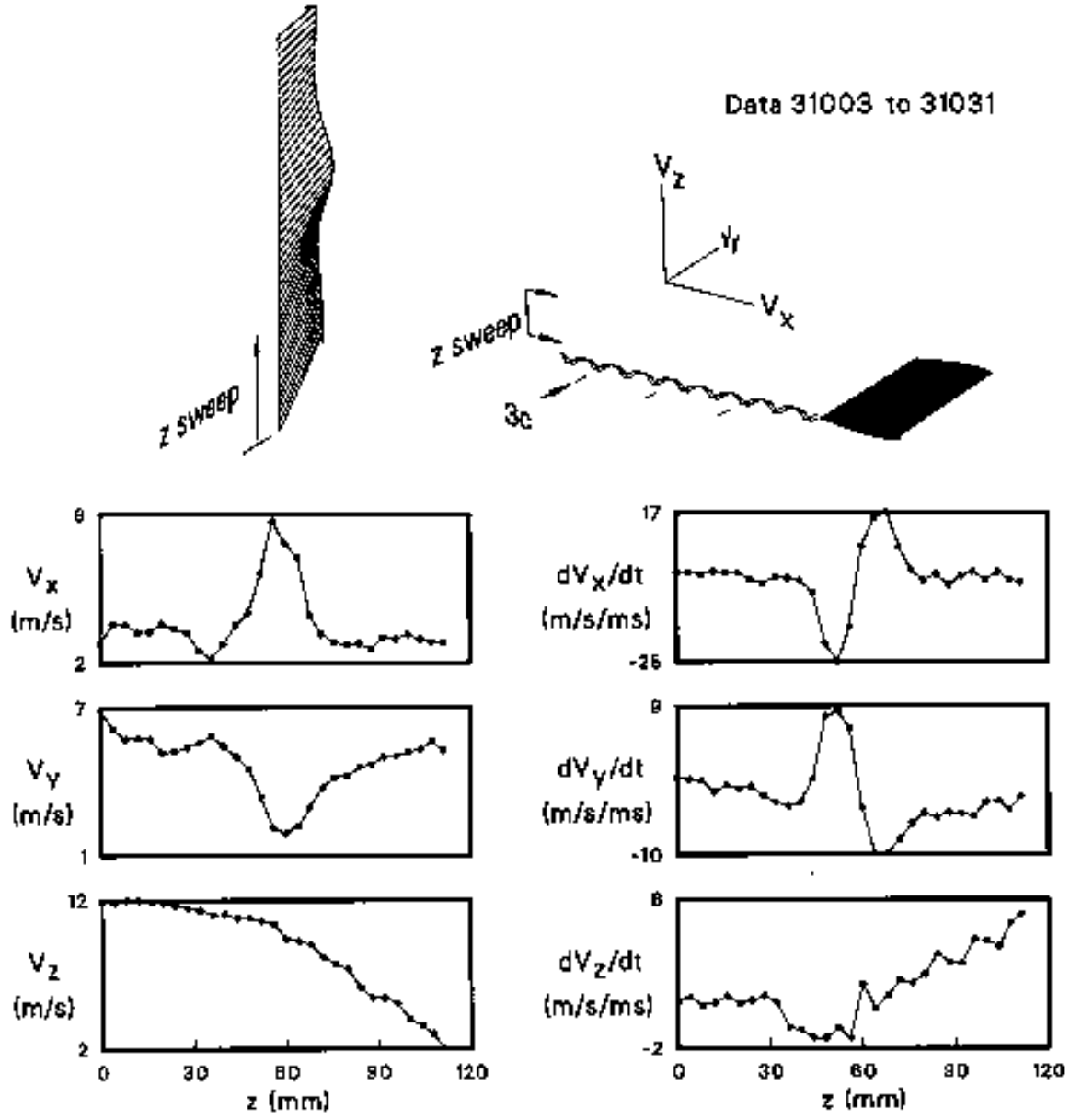

Figure 26. Velocity components along a vertical sweep across the wake at y = 80 mm inboard from the rotor tip and after the blade tip moved forward 3 chord lengths. The rotor speed was 1100 rpm.

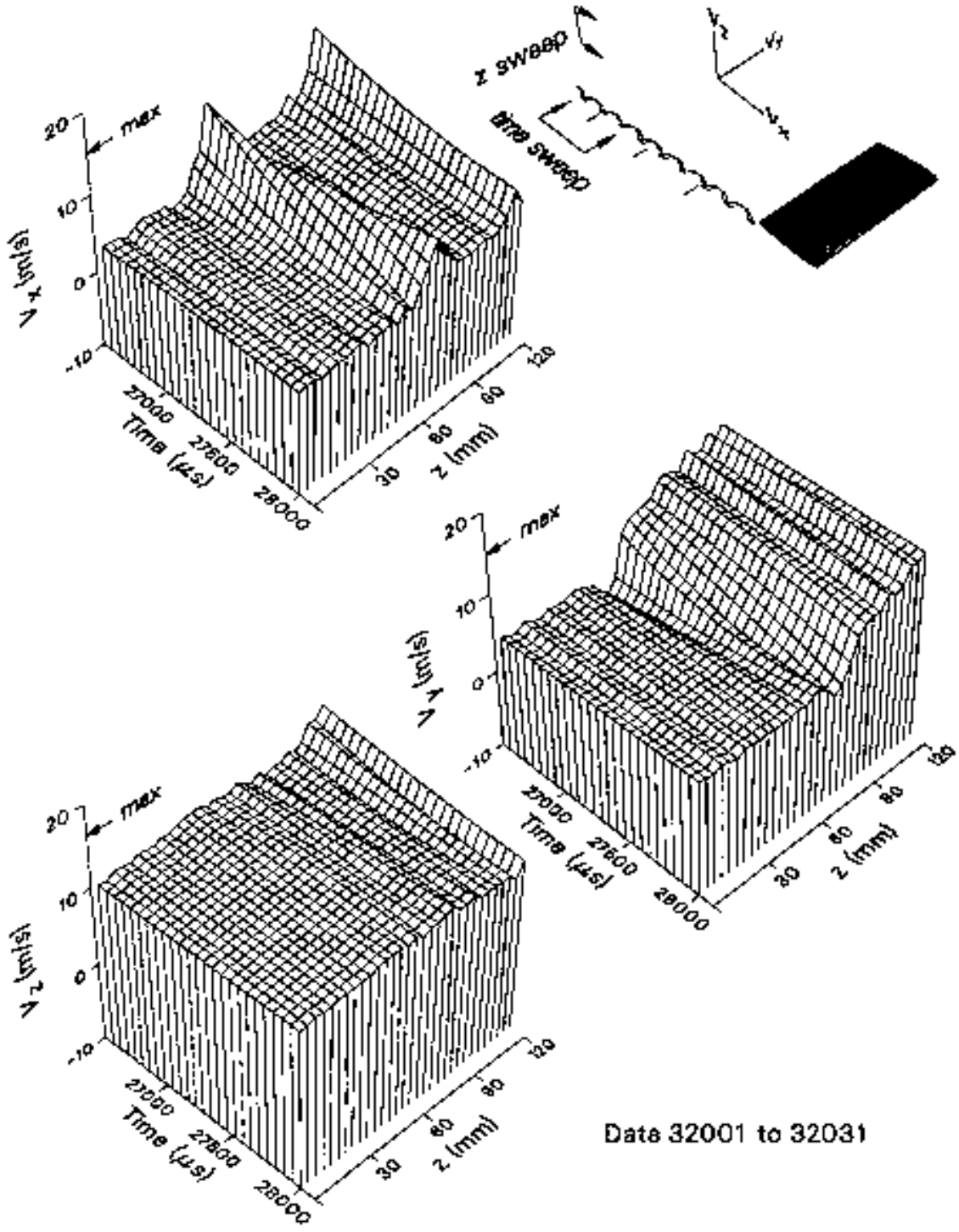

Figure 27. Velocity components along a vertical sweep across the wake at y = 136 mm as the tip of the rotor blade moved from 2.5 to 3.5 chord lengths past the measurement location. The rotor speed was 1100 rpm.

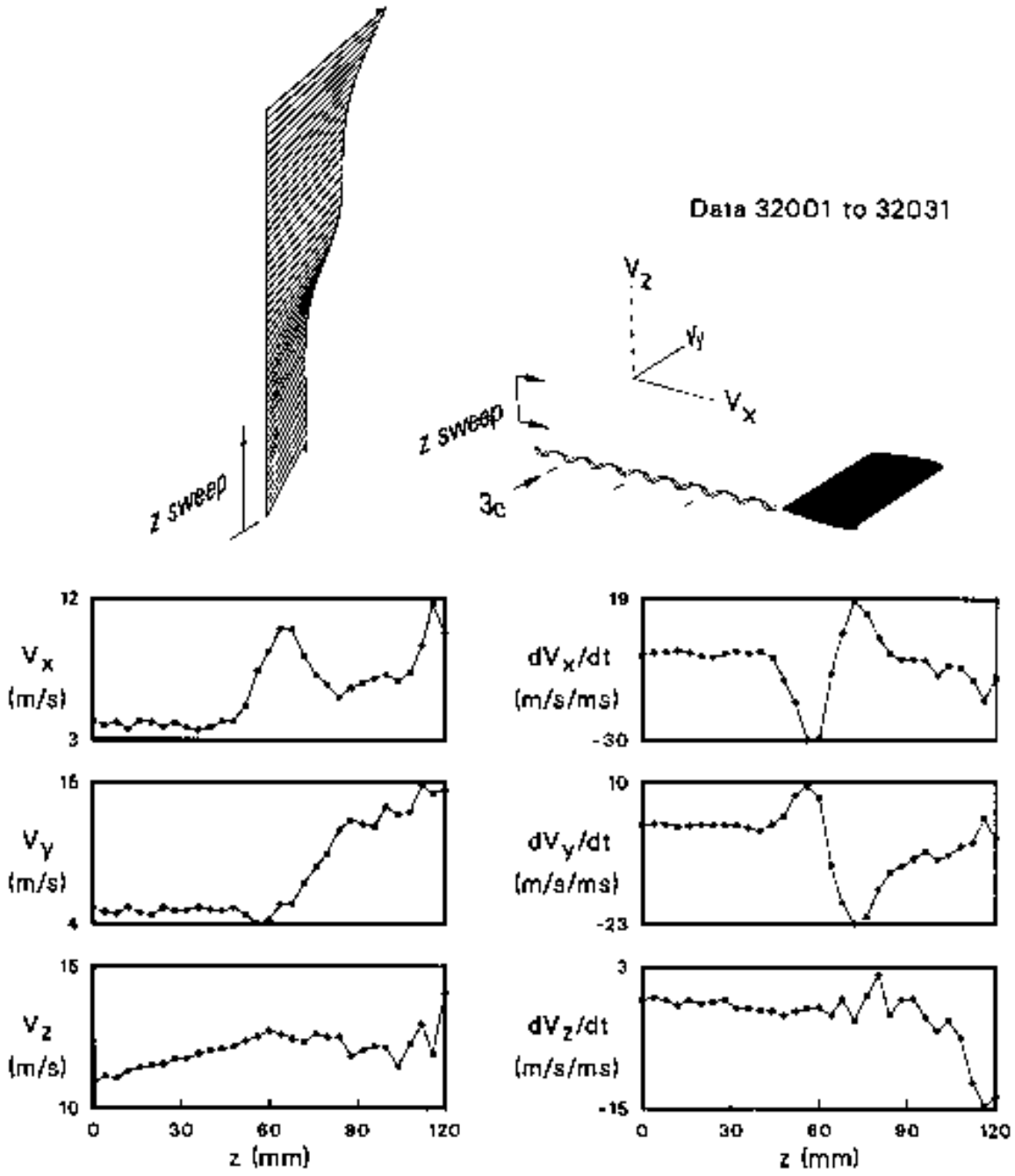

Figure 28. Velocity components along a vertical sweep across the wake at y = 136 mm inboard from the rotor tip and after the blade tip moved forward 3 chord lengths. The rotor speed was 1100 rpm.

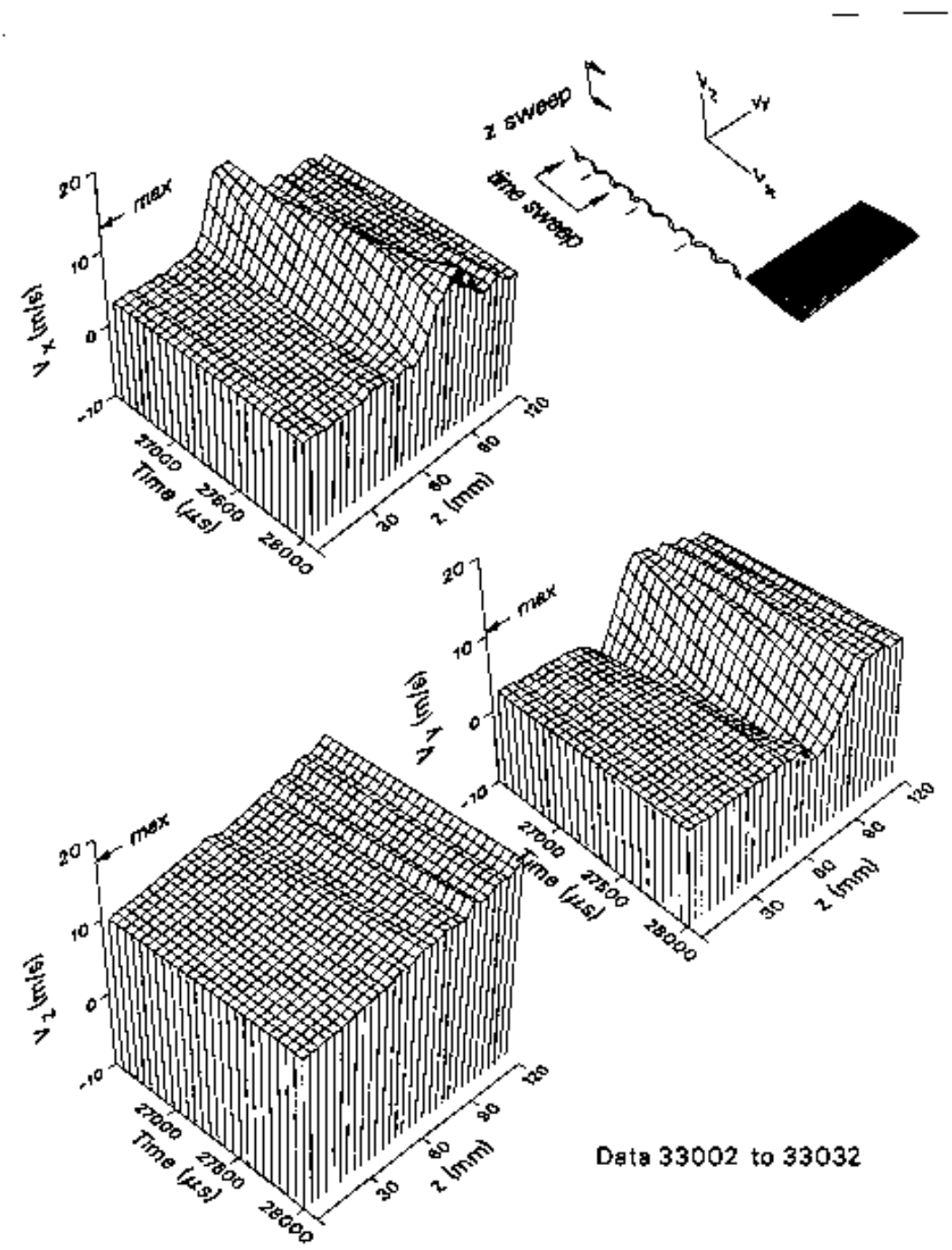

Figure 29. Velocity components along a vertical sweep across the wake at y = 192 mm as the tip of the rotor blade moved from 2.5 to 3.5 chord lengths past the measurement location. The rotor speed was 1100 rpm.

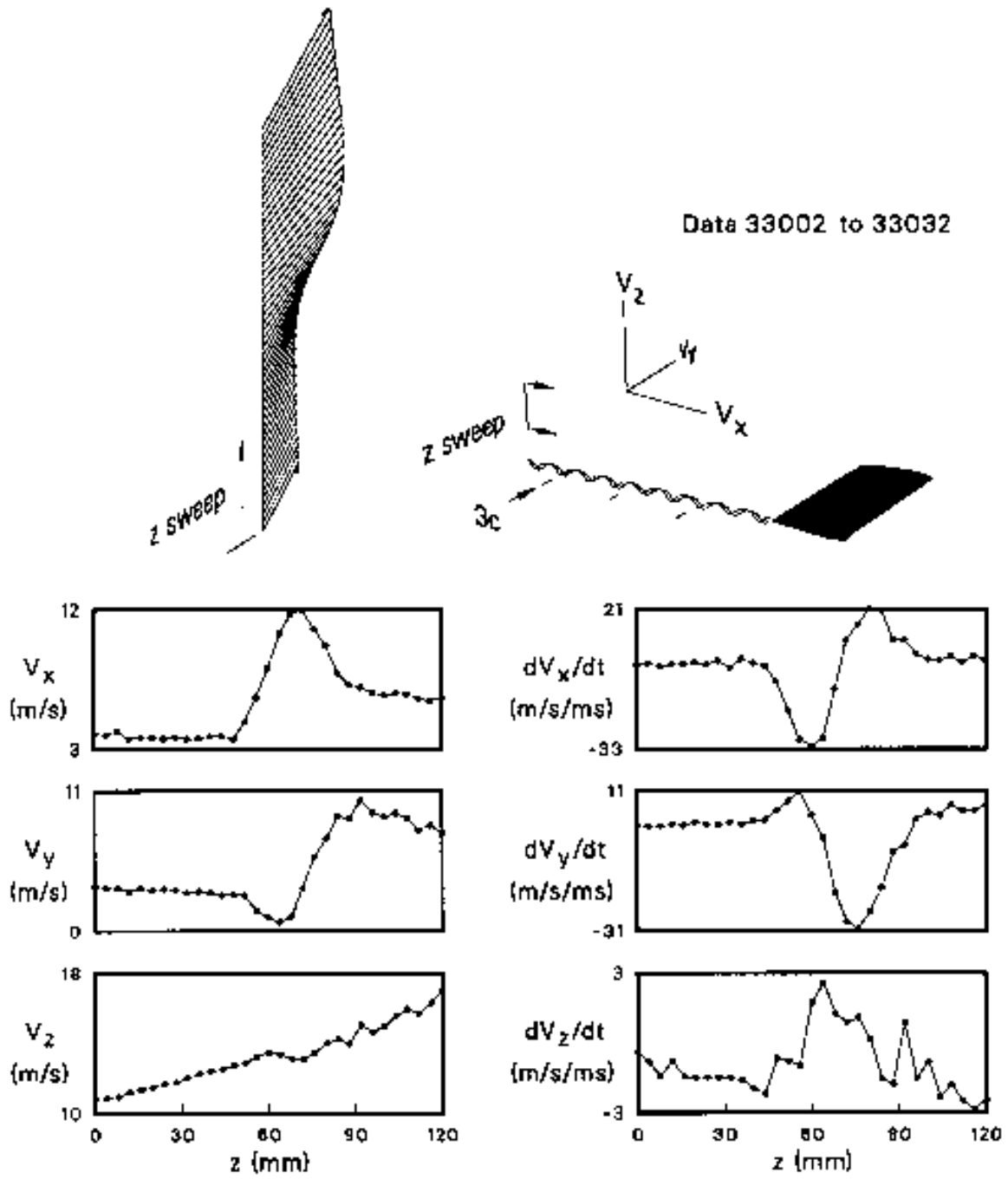

Figure 30. Velocity components along a vertical sweep across the wake at y = 192 mm inboard from the rotor tip and after the blade tip moved forward 3 chord lengths. The rotor speed was 1100 rpm.

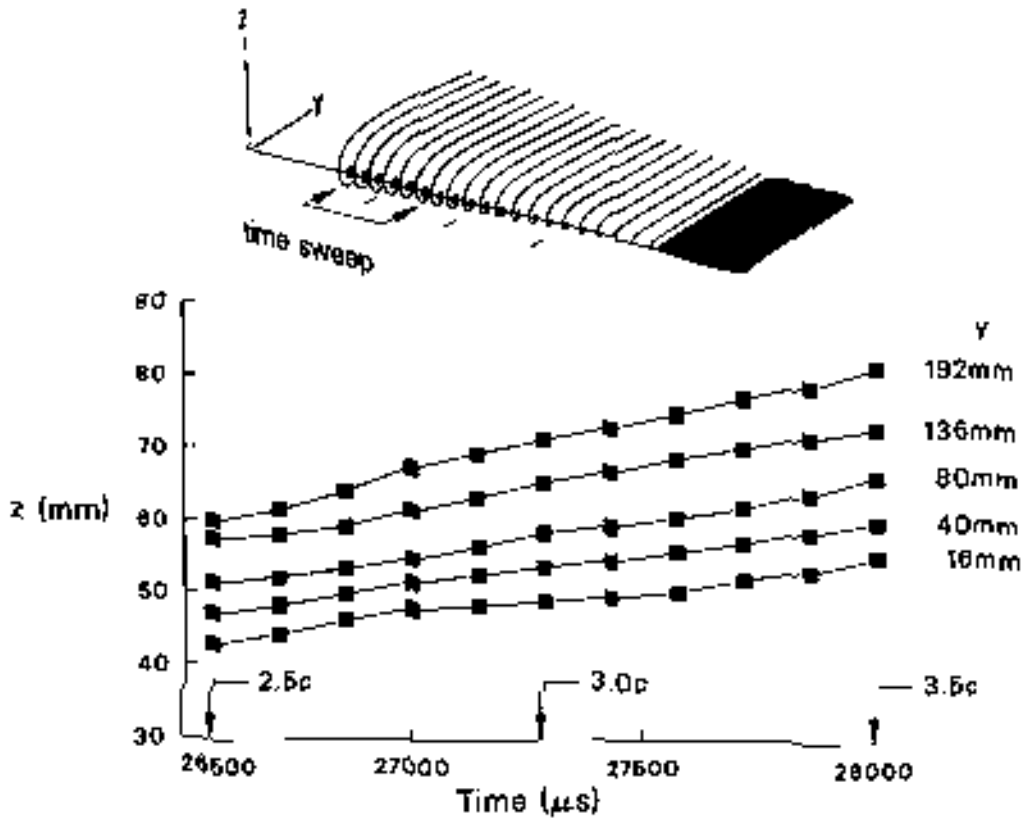

Figure 31. Vertical displacement of the deficit in the V_X profile at particular span locations in the wake of the rotor blade as it travels at 1100 rpm from 2.5 to 3.5 chord lengths past the measurement location.

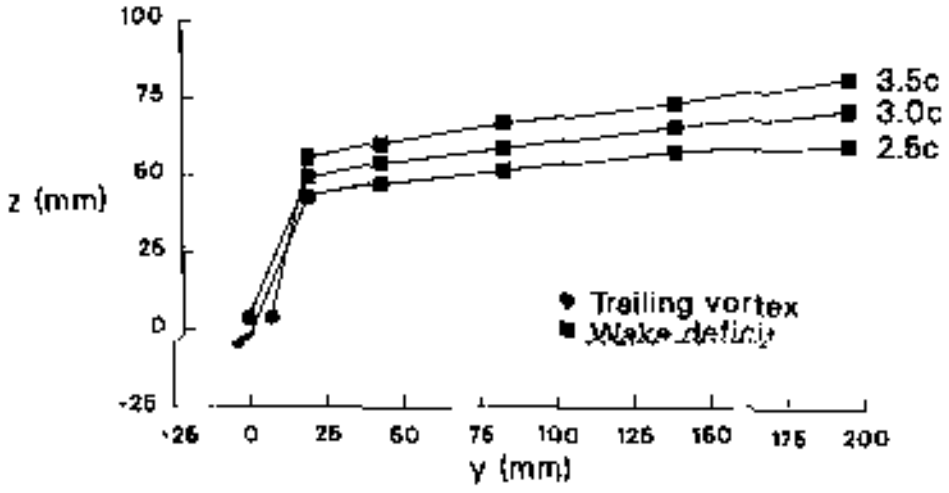

Figure 32. Location of the trailing vortex and the deficit in the V_X profile at selected distances from 2.5 to 3.5 chord lengths behind the rotor blade moving at 1100 rpm.

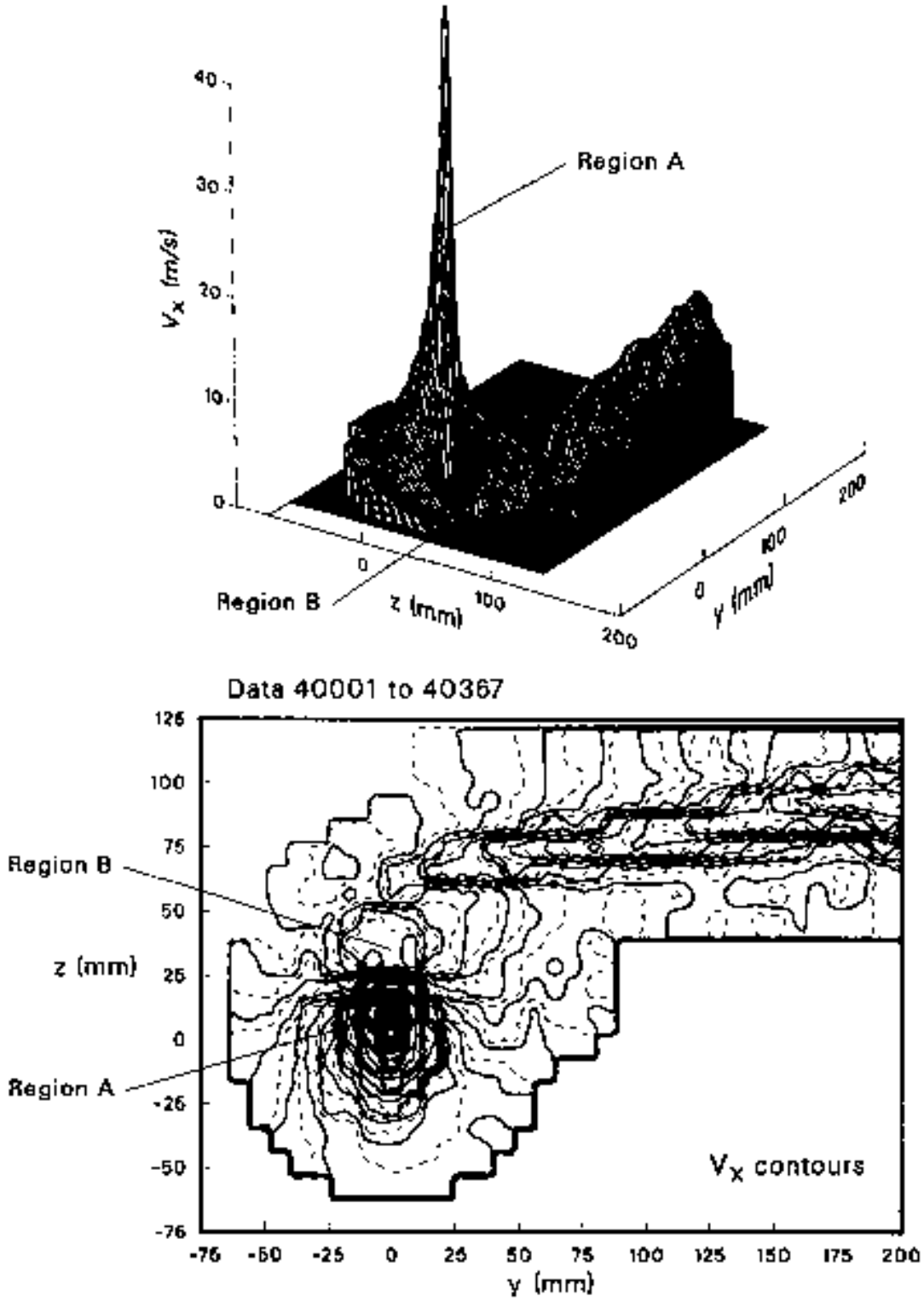

Figure 33. Streamwise velocity component (V_X) over the y-z plane that cuts across the rotor wake after the rotor blade moved 3 chord lengths past the measurement plane. The rotor speed was 1100 rpm.

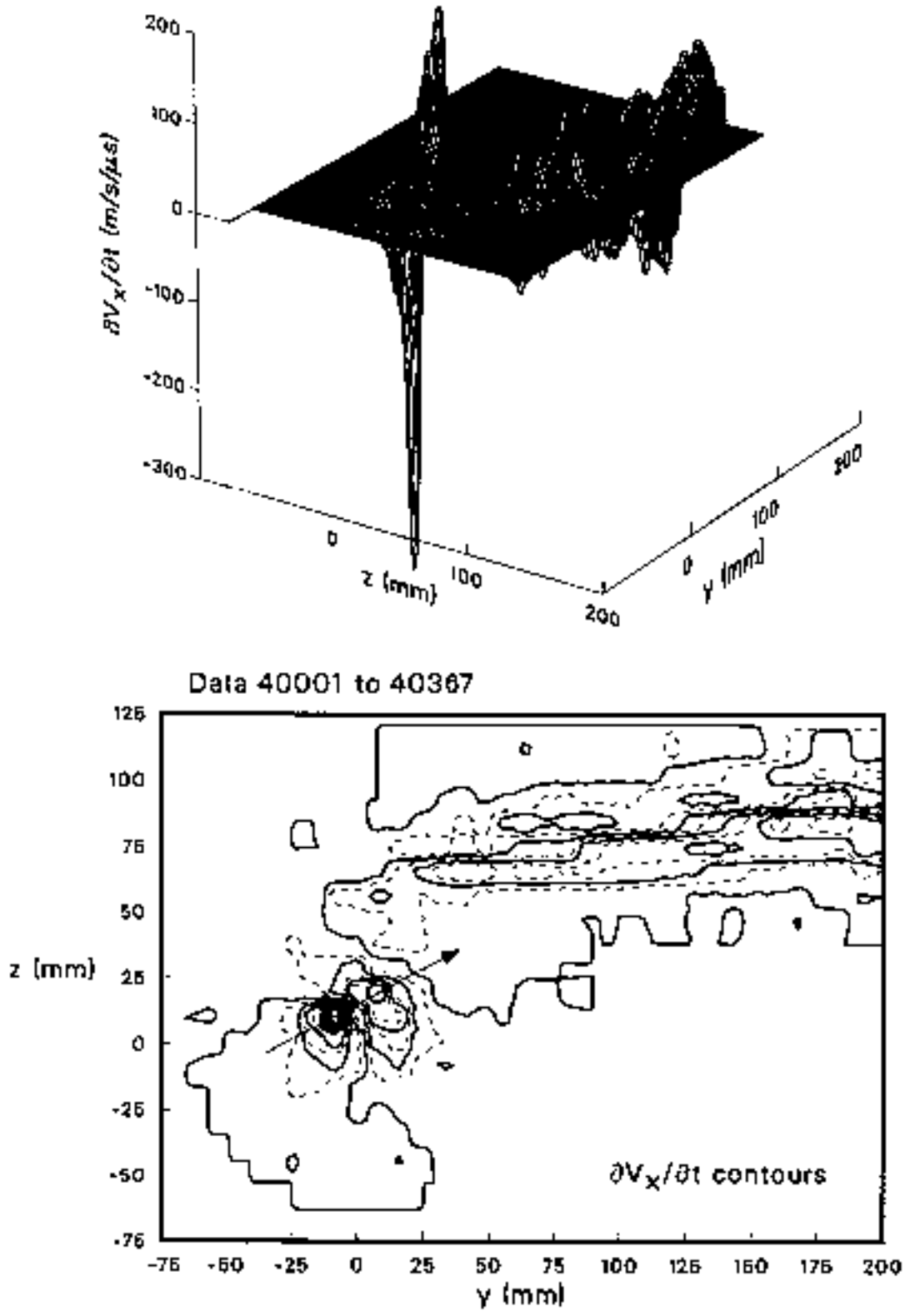

Figure 34. Time derivative of velocity component (V_X) over the y-z plane that cuts across the rotor wake after the rotor blade moved 3 chord lengths past the measurement plane. The rotor speed was 1100 rpm.

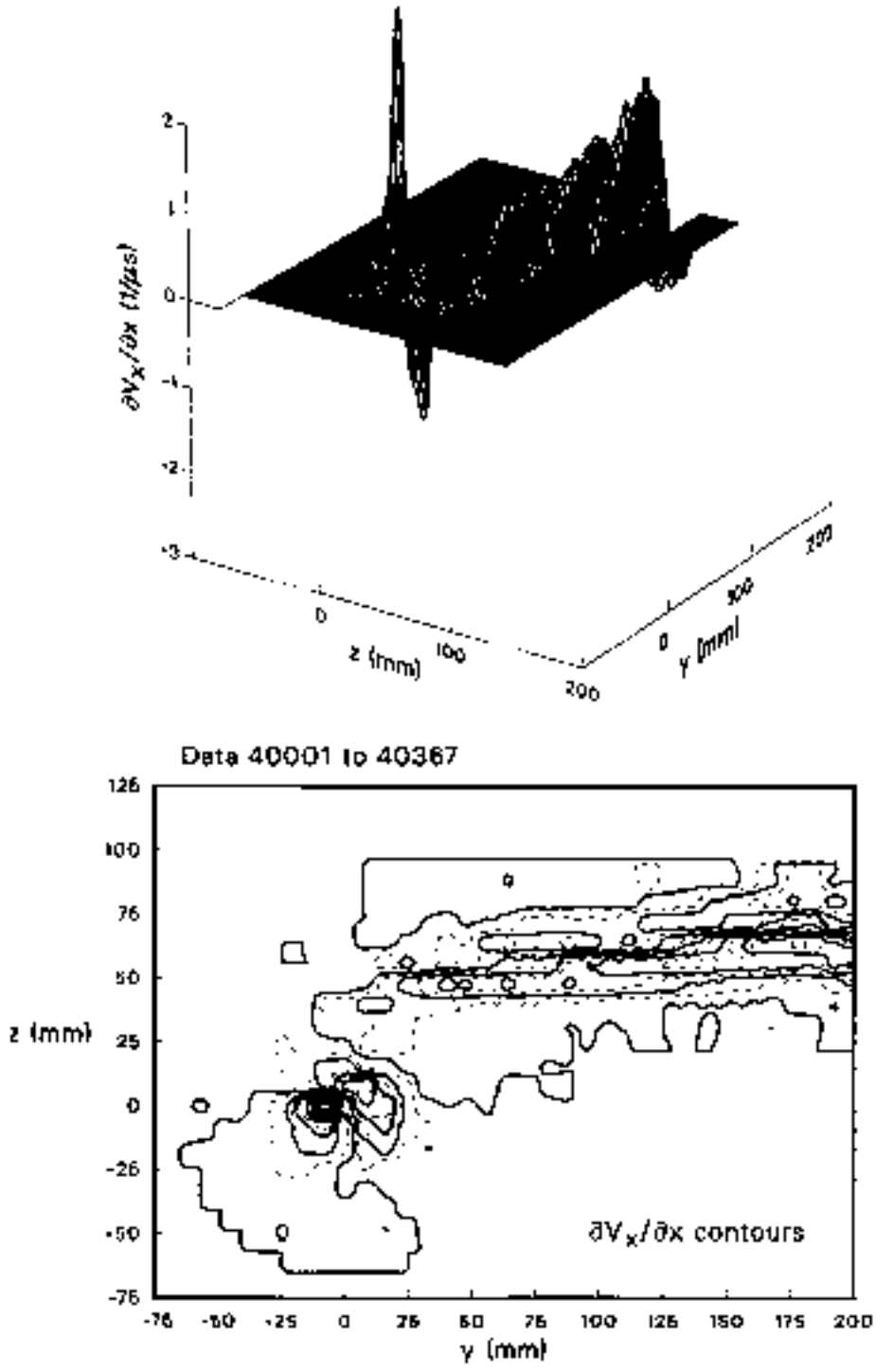

Figure 35. Streamwise derivative of velocity component (V_X) over the y-z plane that cuts across the rotor wake after the rotor blade moved 3 chord lengths past the measurement plane. The rotor speed was 1100 rpm.

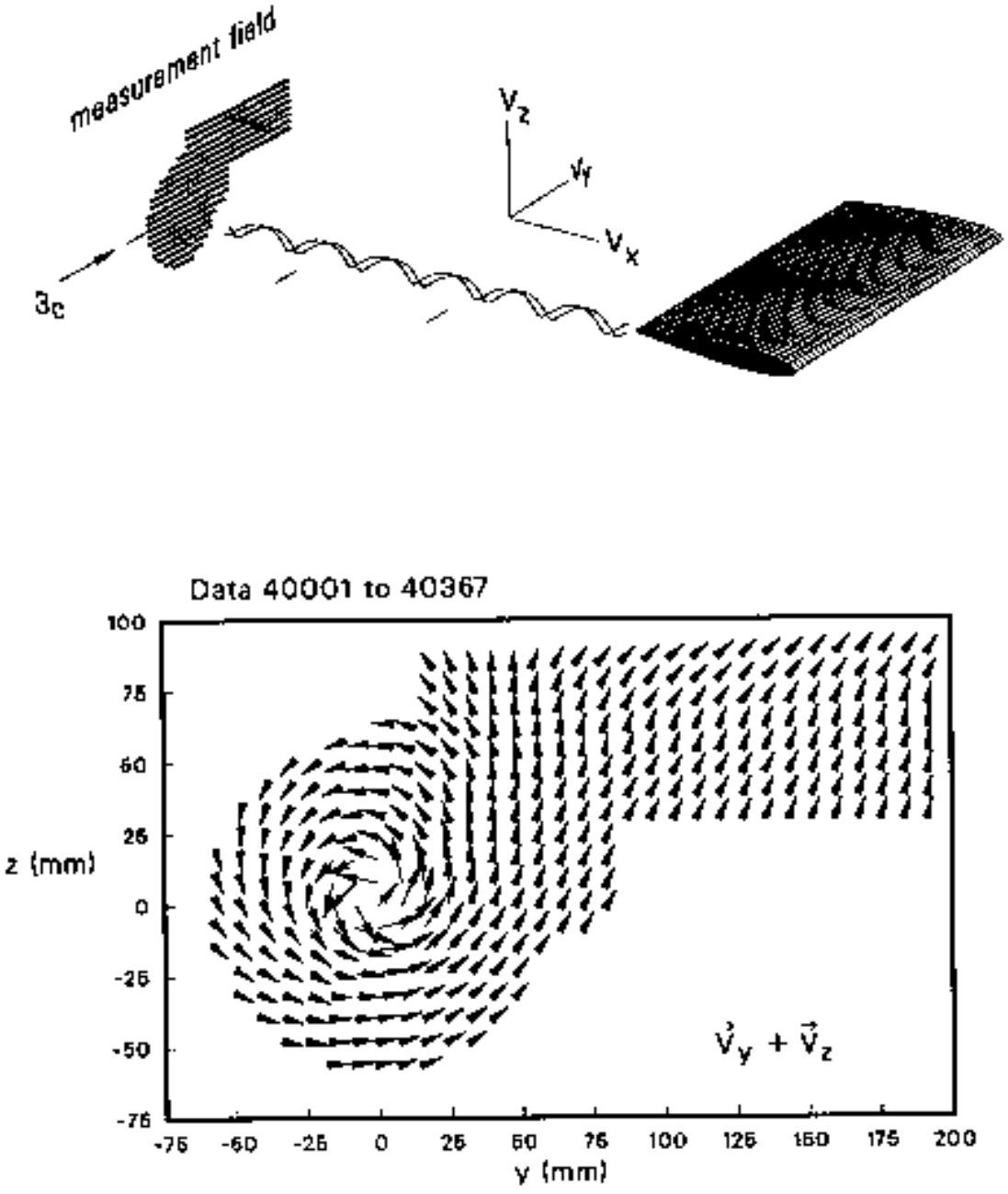

Figure 36. Velocity-vector field in the y-z plane after the rotor blade moved 3 chord lengths past the measurement plane. The rotor speed was 1100 rpm.

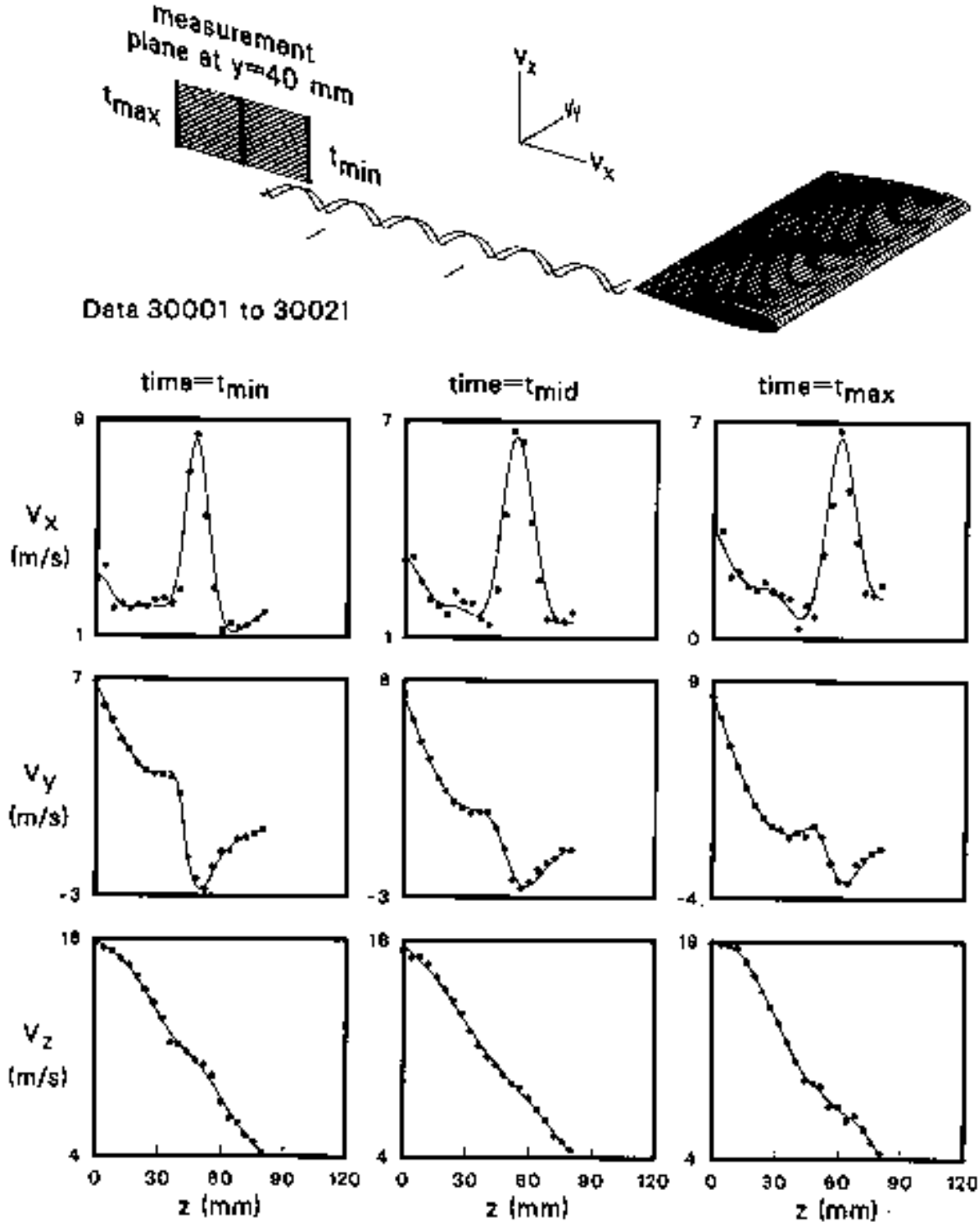

Figure 37. Velocity profiles (data with spline-curve smoothing) along a vertical sweep across the wake at y = 40 mm for 3 specific times as the tip of the rotor blade moved from 2.5 to 3.5 chord lengths past the measurement location. The rotor speed was 1100 rpm.

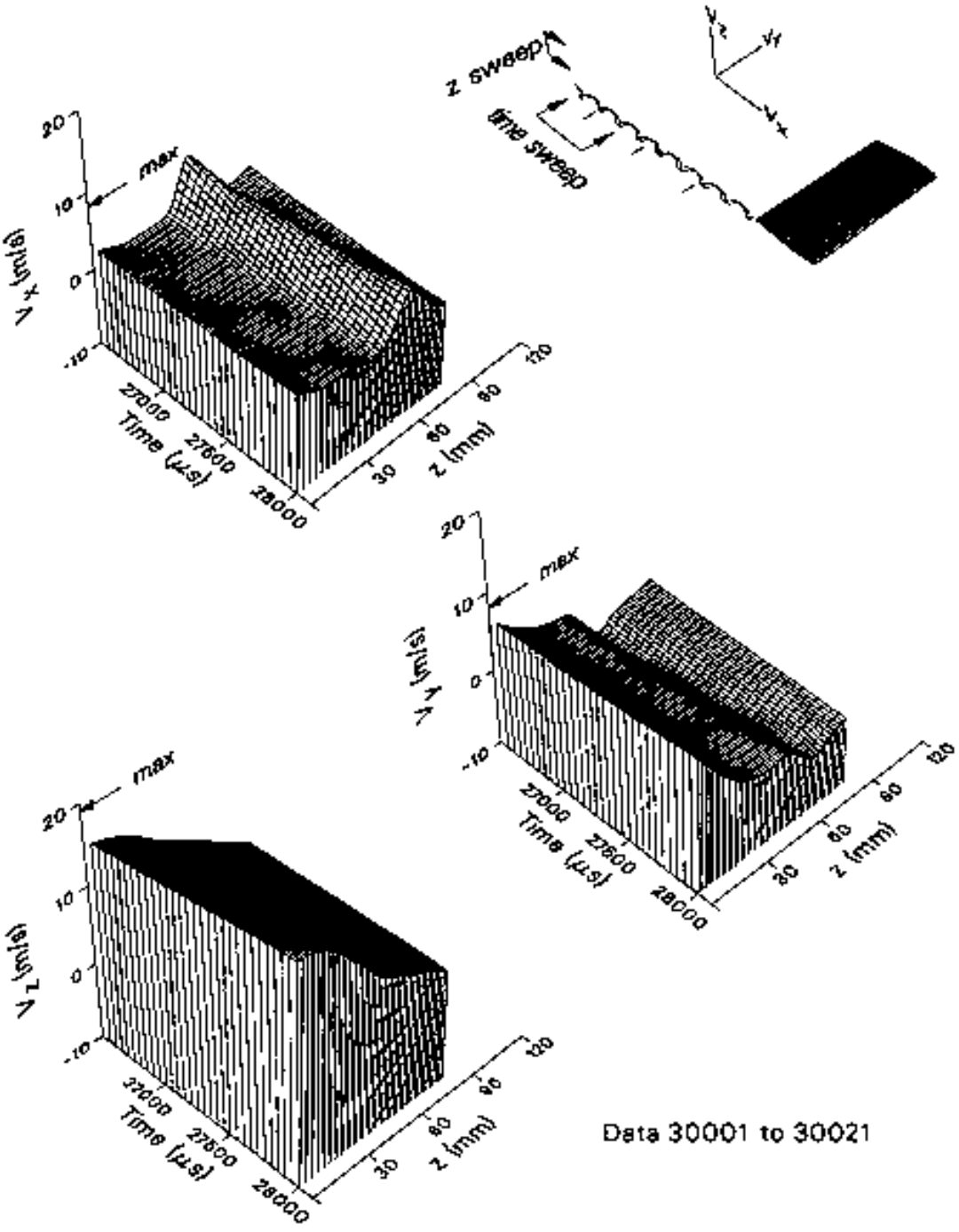

Figure 38. Velocity components (after spline-curve smoothing) along a vertical sweep across the wake at y = 40 mm as the tip of the rotor blade moved from 2.5 to 3.5 chord lengths past the measurement location. The rotor speed was 1100 rpm.

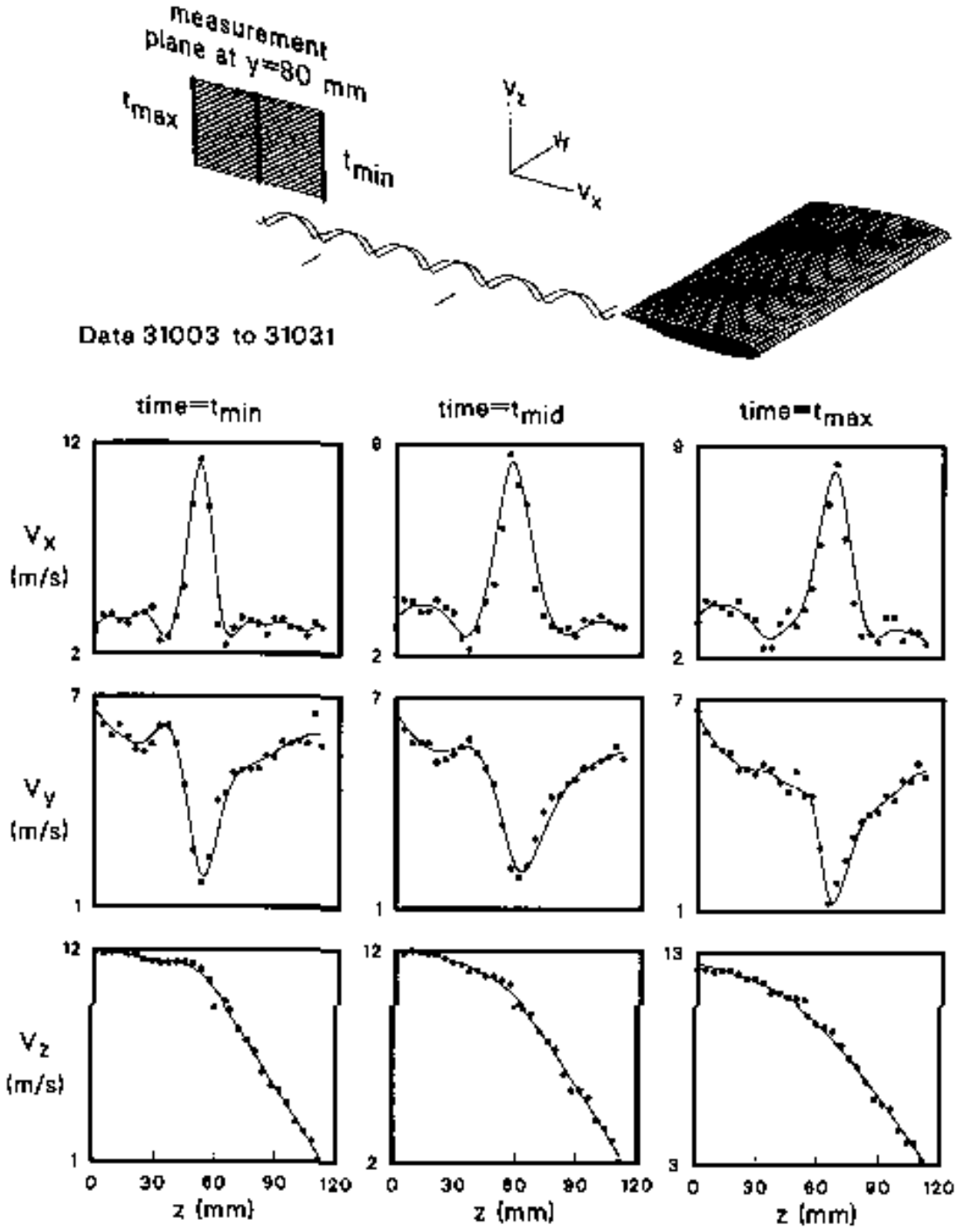

Figure 39. Velocity profiles (data with spline-curve smoothing) along a vertical sweep across the wake at y = 80 mm for 3 specific times as the tip of the rotor blade moved from 2.5 to 3.5 chord lengths past the measurement location. The rotor speed was 1100 rpm.

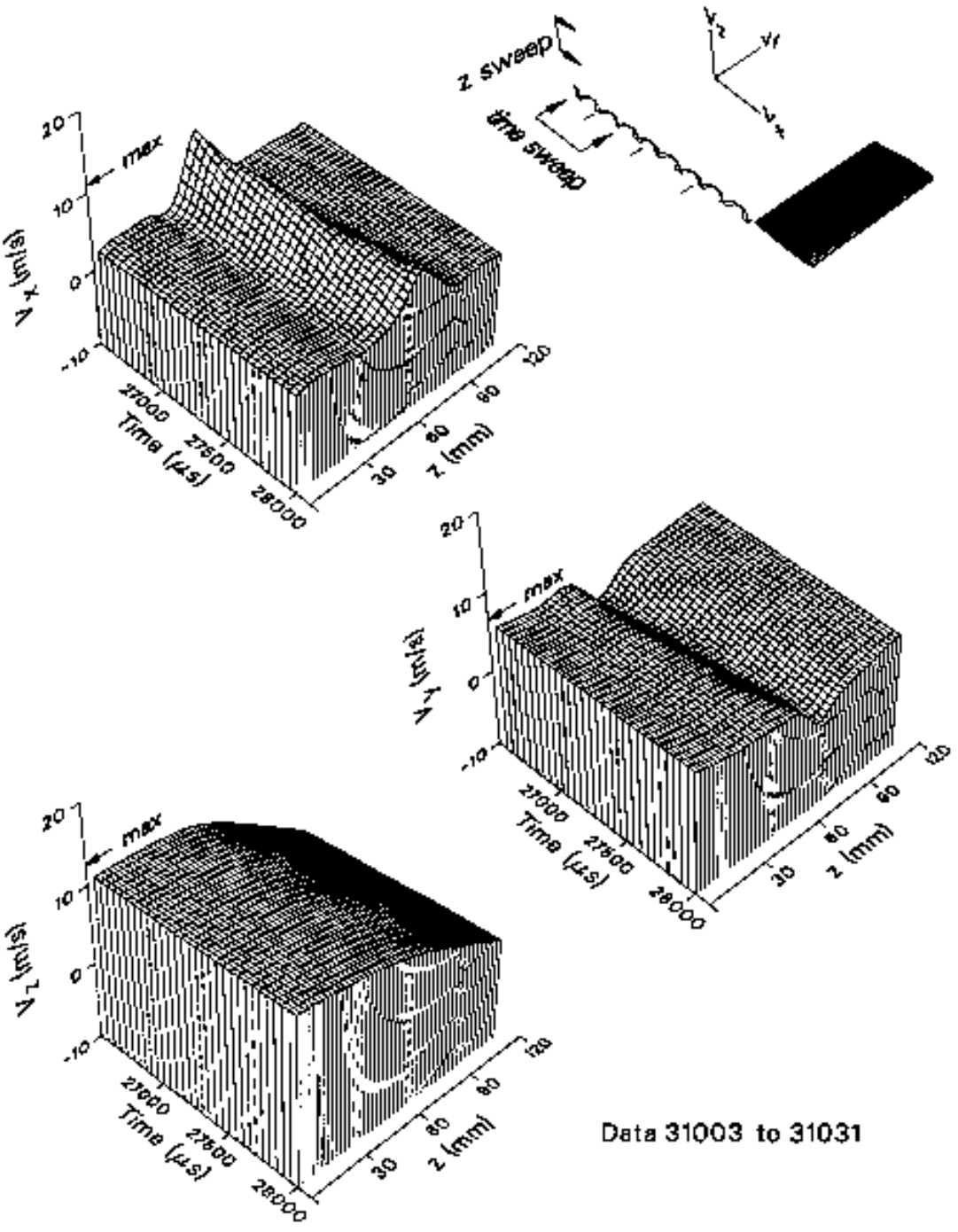

Figure 40. Velocity components (after spline-curve smoothing) along a vertical sweep across the wake at y = 80 mm as the tip of the rotor blade moved from 2.5 to 3.5 chord lengths past the measurement location. The rotor speed was 1100 rpm.

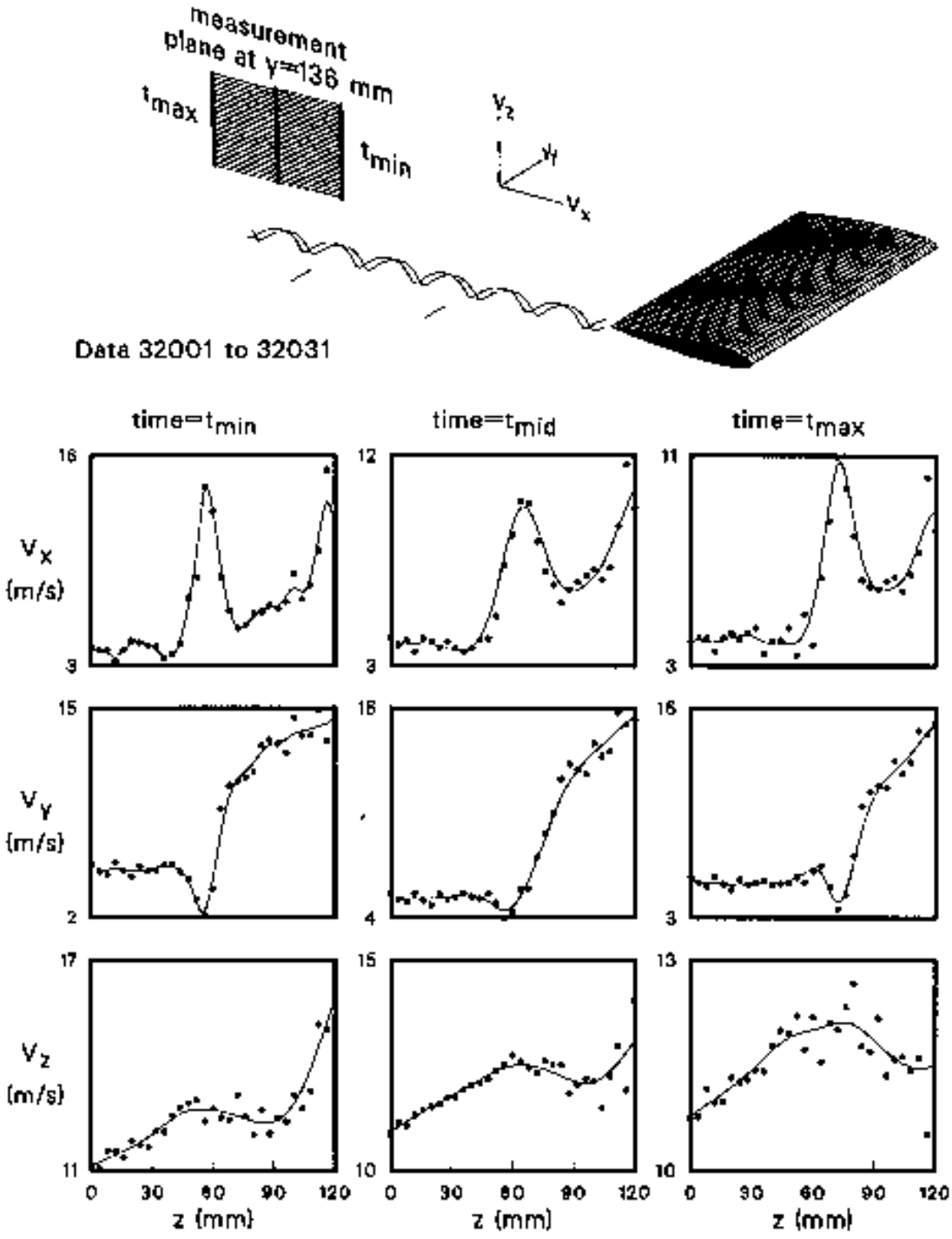

Figure 41. Velocity profiles (data with spline-curve smoothing) along a vertical sweep across the wake at y = 136 mm for 3 specific times as the tip of the rotor blade moved from 2.5 to 3.5 chord lengths past the measurement location. The rotor speed was 1100 rpm.

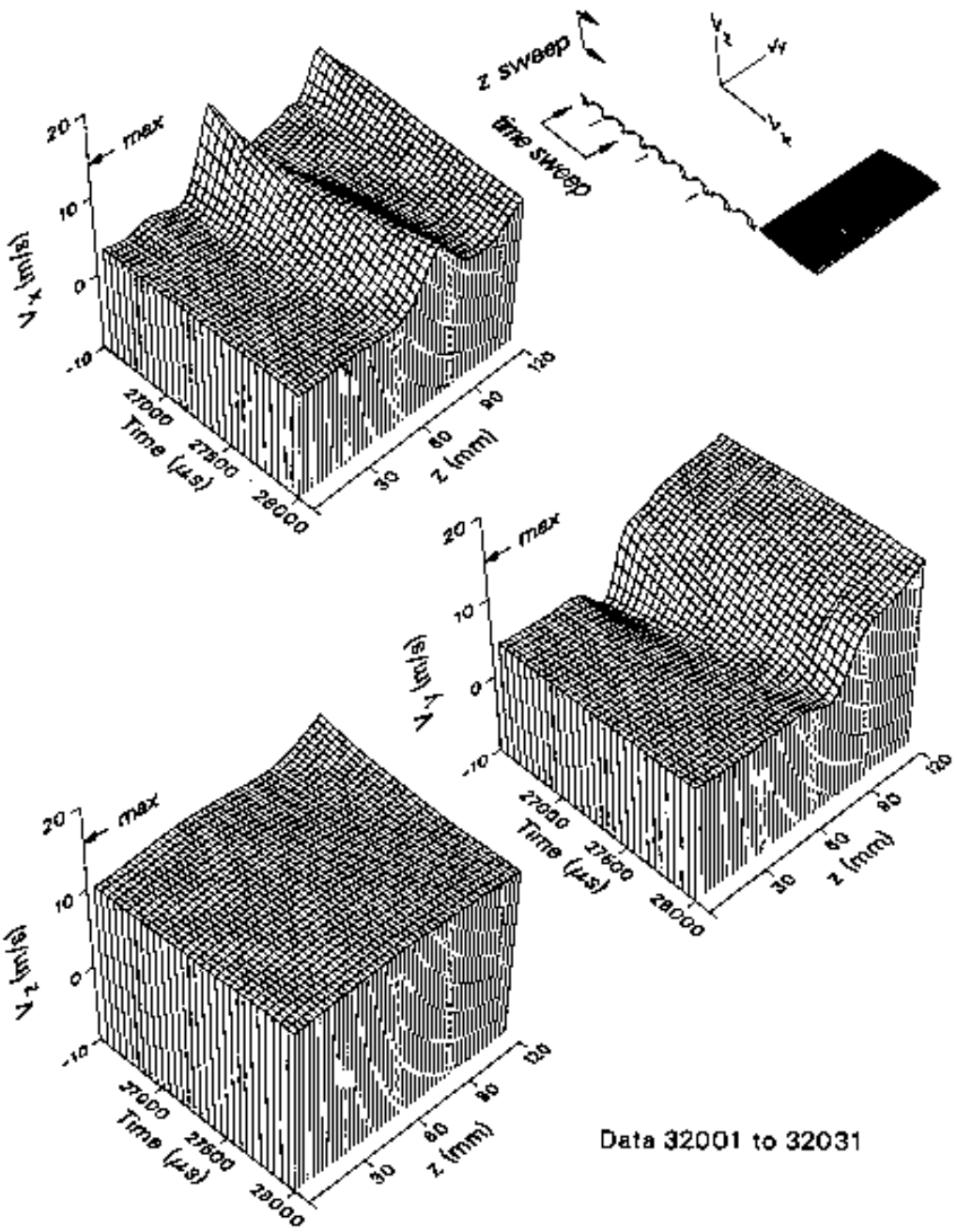

Figure 42. Velocity components (after spline-curve smoothing) along a vertical sweep across the wake at y = 136 mm as the tip of the rotor blade moved from 2.5 to 3.5 chord lengths past the measurement location. The rotor speed was 1100 rpm.

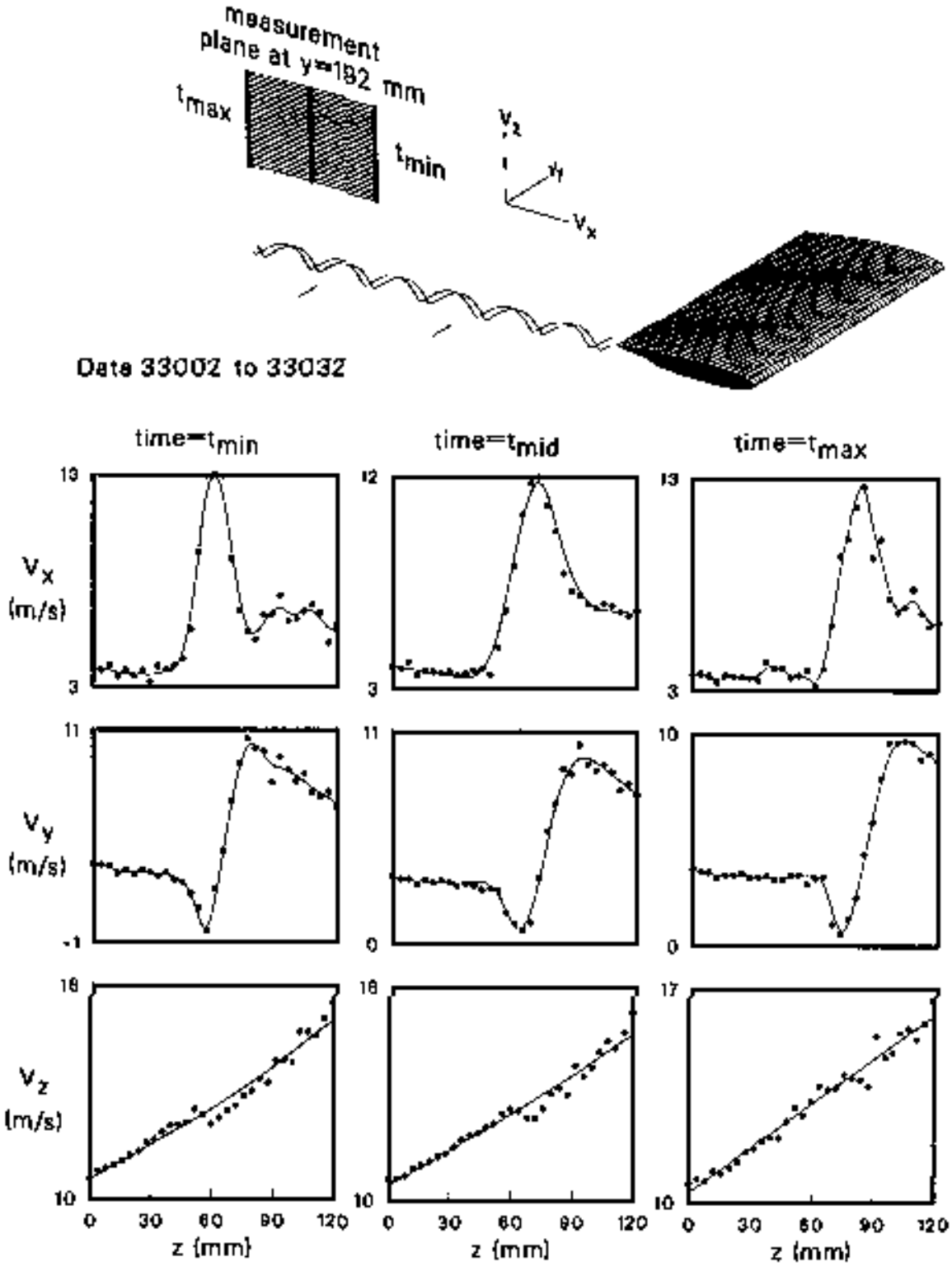

Figure 43. Velocity profiles (data with spline-curve smoothing) along a vertical sweep across the wake at y = 192 mm for 3 specific times as the tip of the rotor blade moved from 2.5 to 3.5 chord lengths past the measurement location. The rotor speed was 1100 rpm.

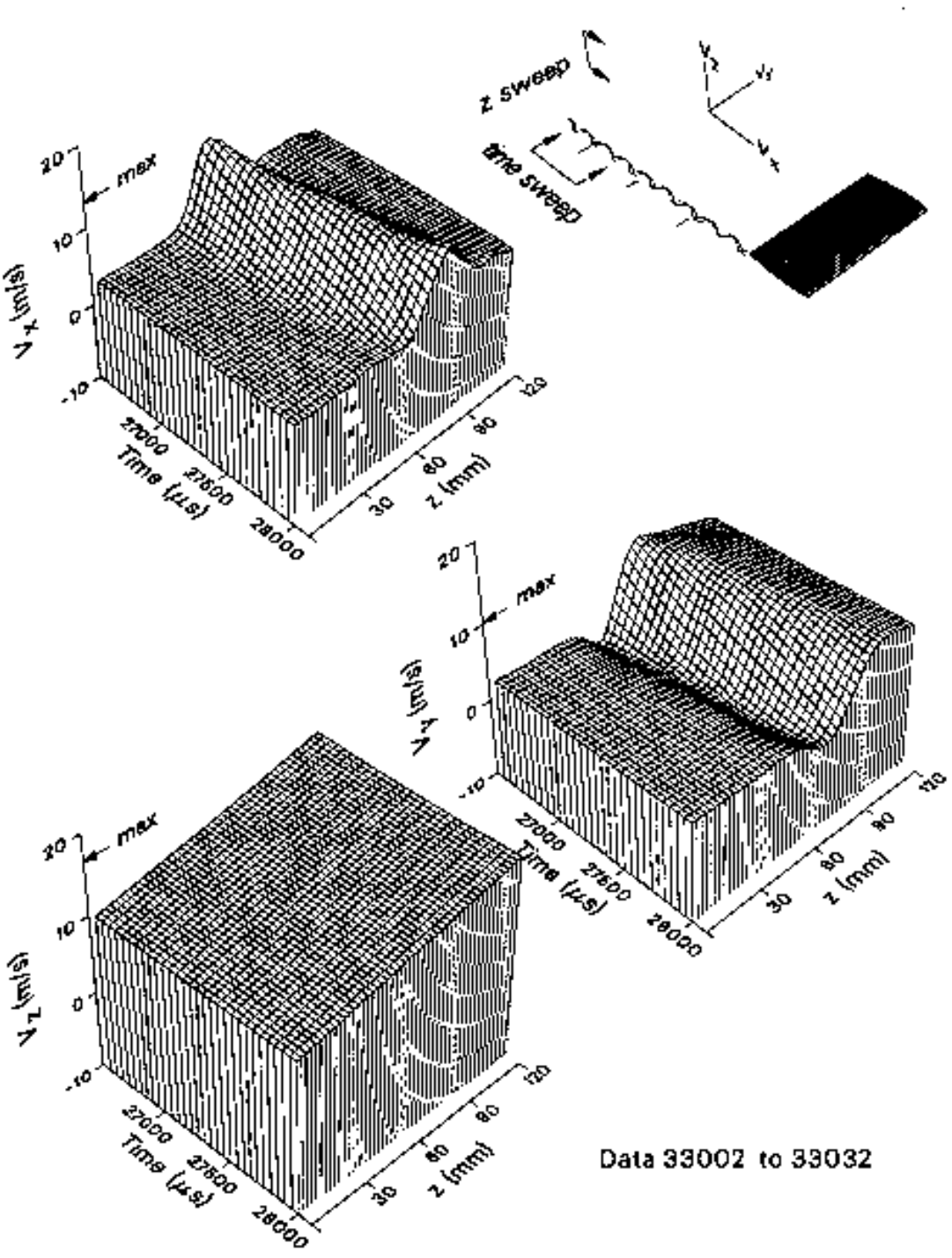

Figure 44. Velocity components (after spline-curve smoothing) along a vertical sweep across the wake at y = 192 mm as the tip of the rotor blade moved from 2.5 to 3.5 chord lengths past the measurement location. The rotor speed was 1100 rpm.

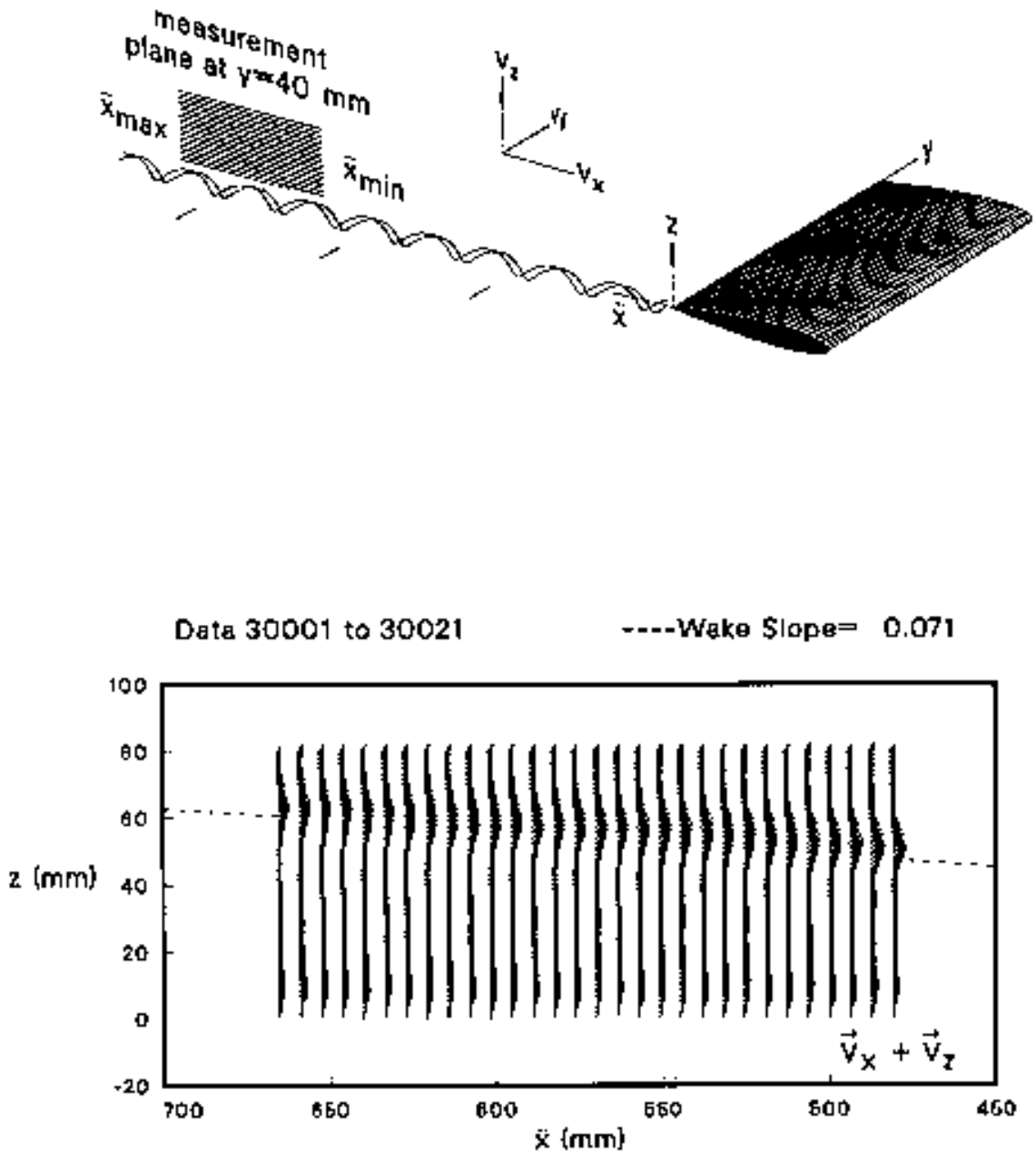

Figure 45. Velocity-vector field in the x-z plane passing through y = 40 mm during the time that the tip of the rotor blade advanced from 2.5 to 3.5 chord lengths. The rotor speed was 1100 rpm.

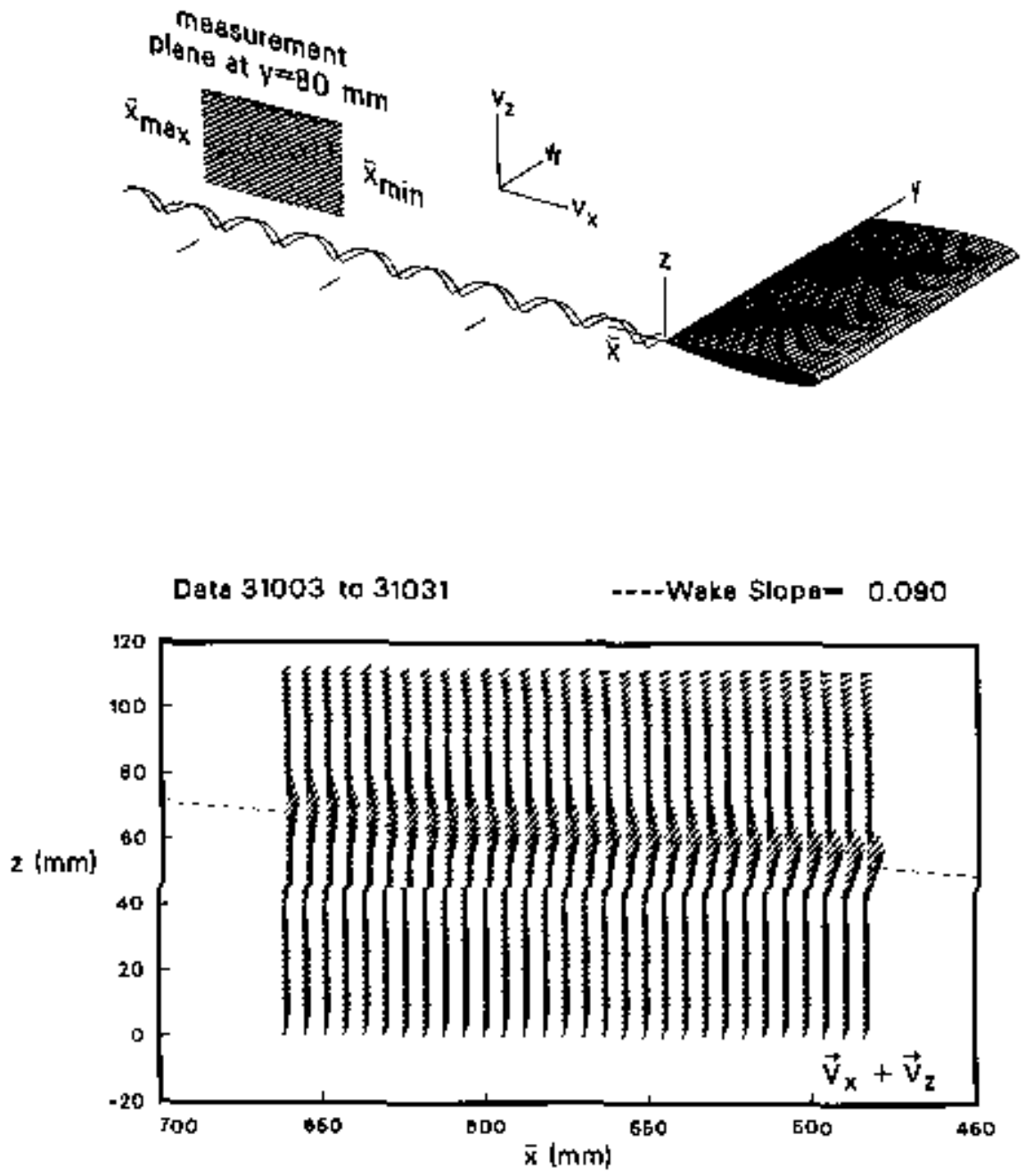

Figure 46. Velocity-vector field in the x-z plane passing through y = 80 mm during the time that the tip of the rotor blade advanced from 2.5 to 3.5 chord lengths. The rotor speed was 1100 rpm.

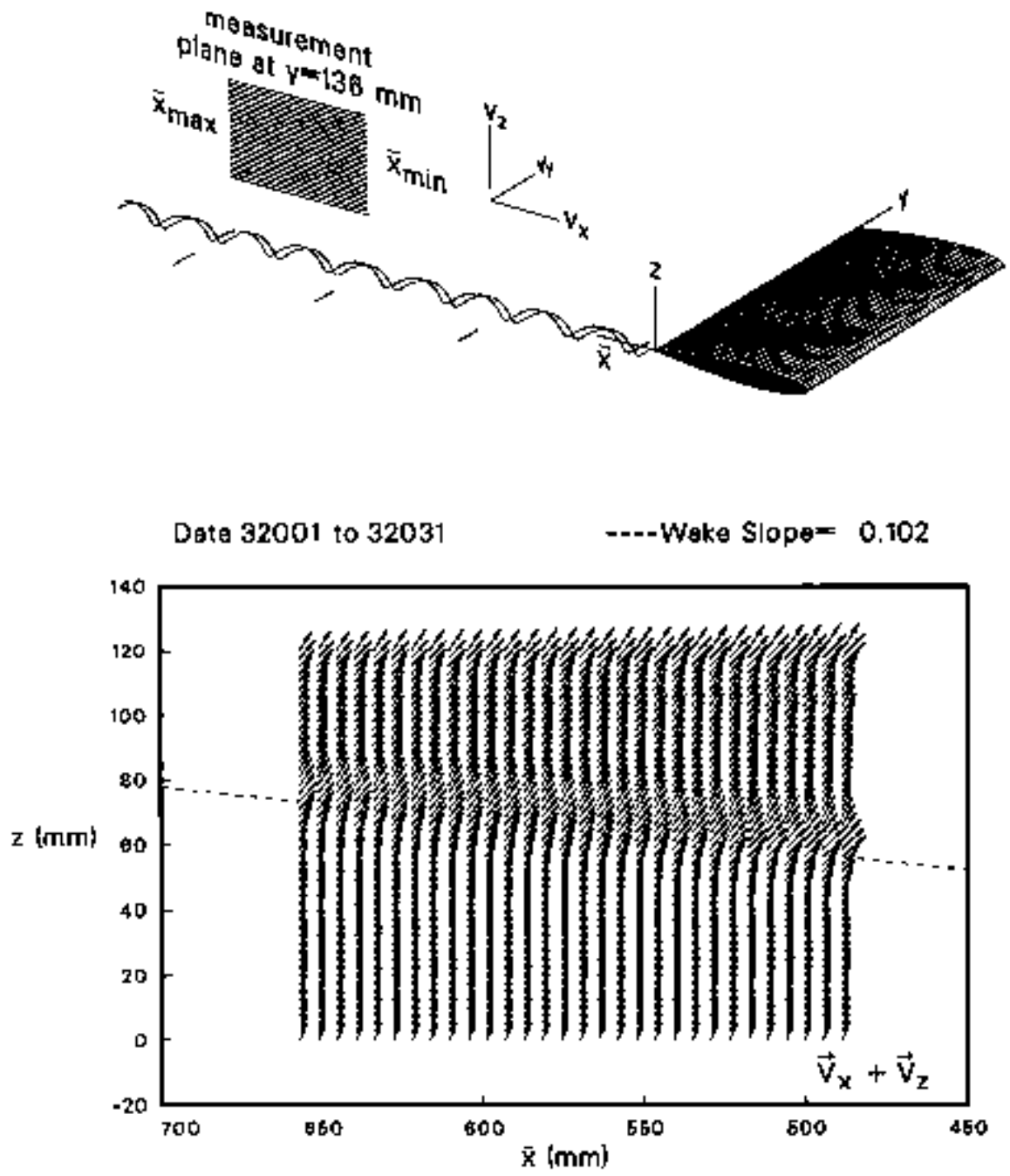

Figure 47. Velocity-vector field in the x-z plane passing through y = 136 mm during the time that the tip of the rotor blade advanced from 2.5 to 3.5 chord lengths. The rotor speed was 1100 rpm.

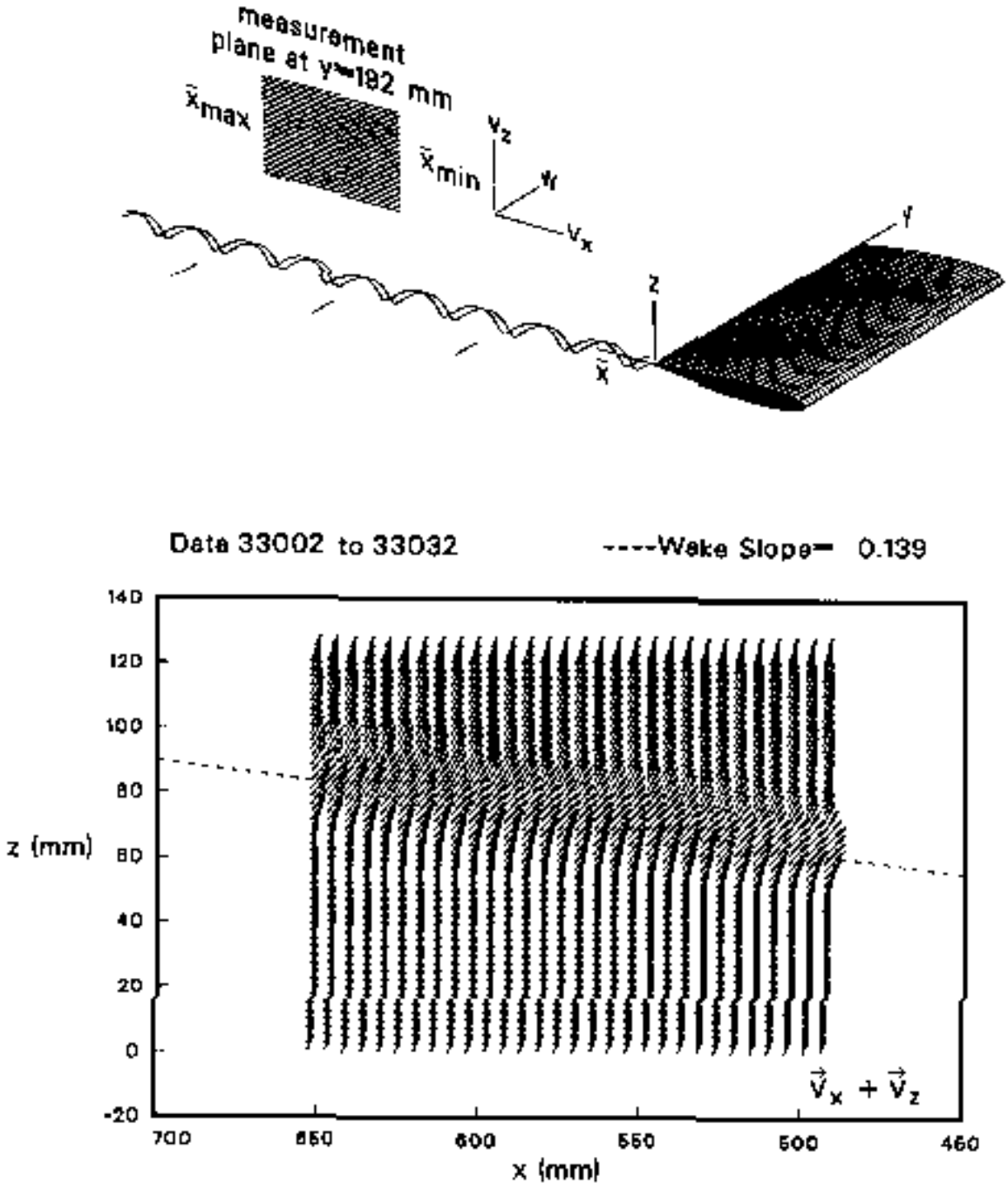

Figure 48. Velocity-vector field in the x-z plane passing through y = 192 mm during the time that the tip of the rotor blade advanced from 2.5 to 3.5 chord lengths. The rotor speed was 1100 rpm.

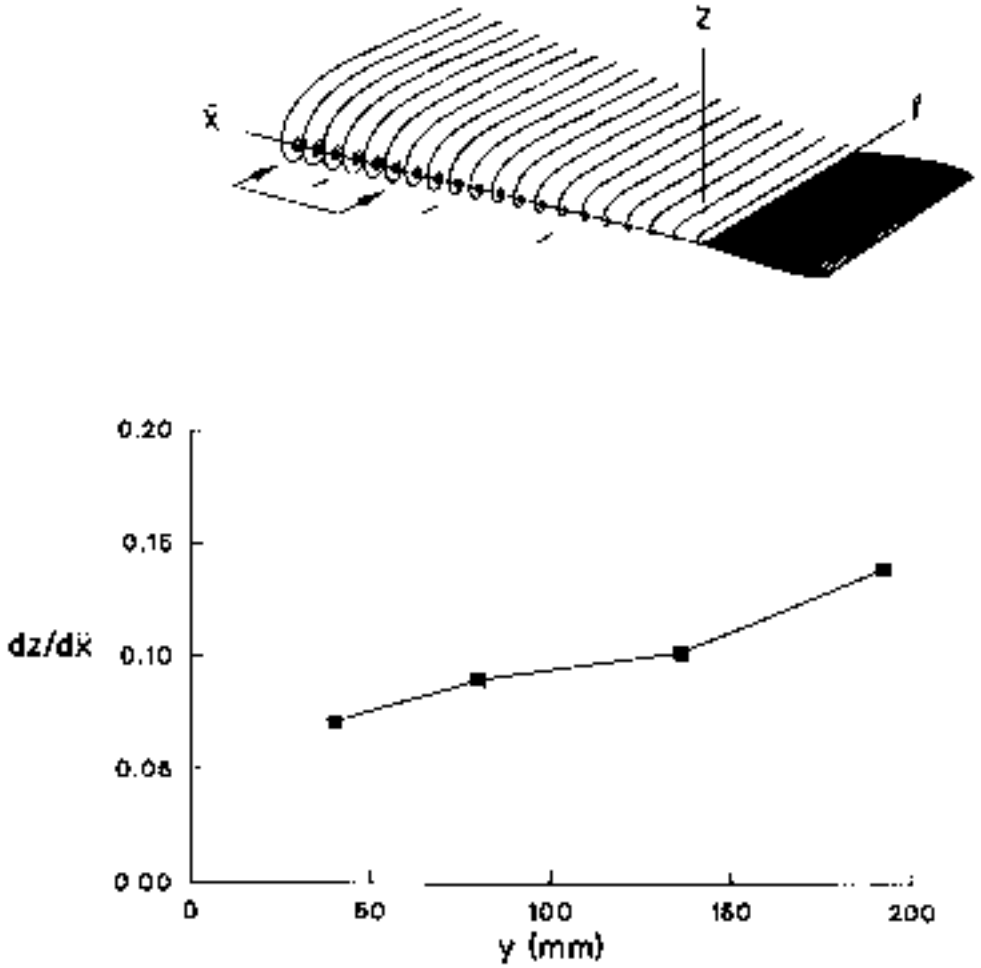

Figure 49. Vertical displacement of the wake with respect to increasing downstream distance (wake slope) at particular span locations during the time that the rotor blade advanced at 1100 rpm from 2.5 to 3.5 chord lengths past the measurement location.

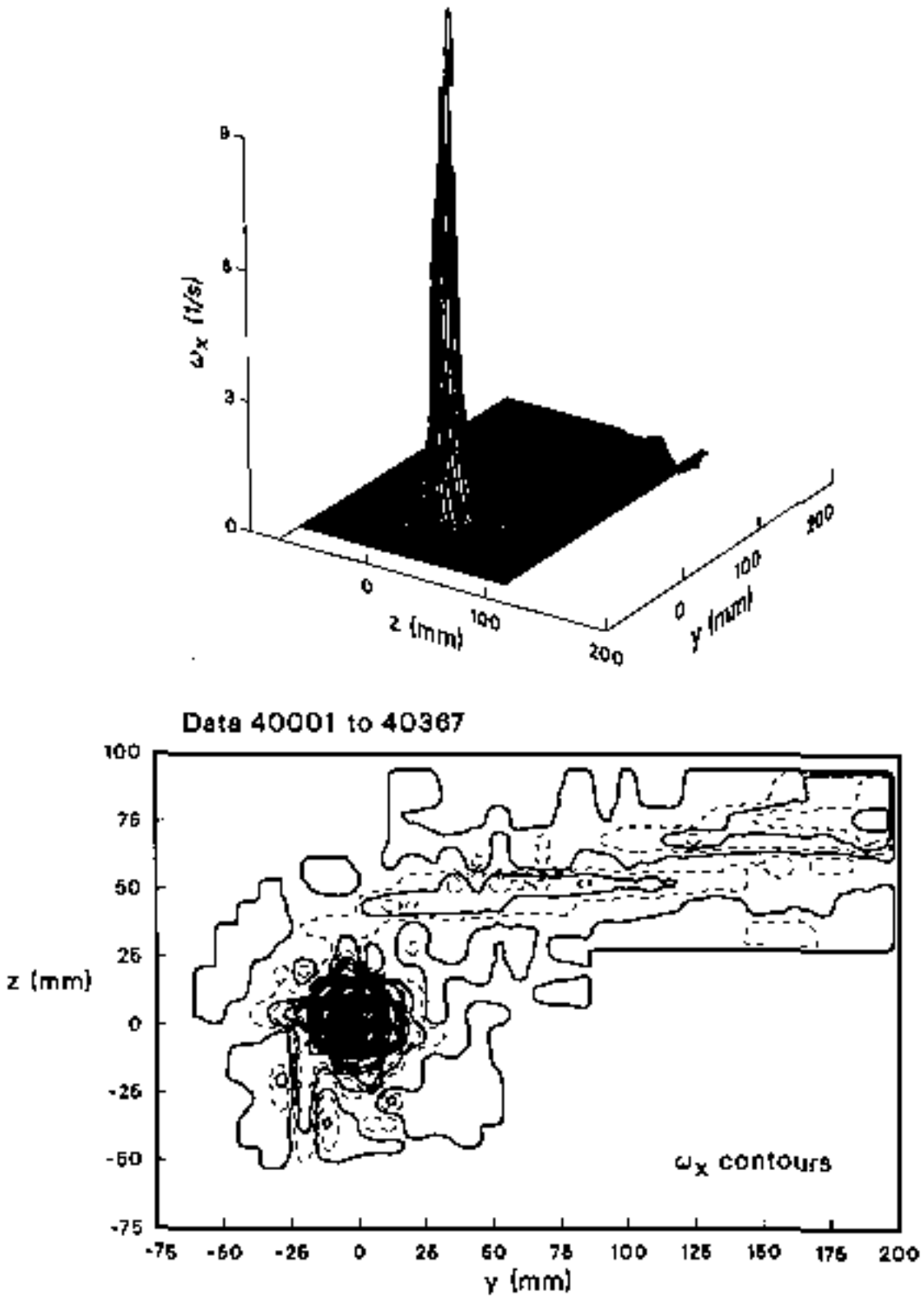

Figure 50. Streamwise component of vorticity (ω_X) over the y-z plane that cuts across the rotor wake after the rotor blade moved 3 chord lengths past the measurement plane. The rotor speed was 1100 rpm.

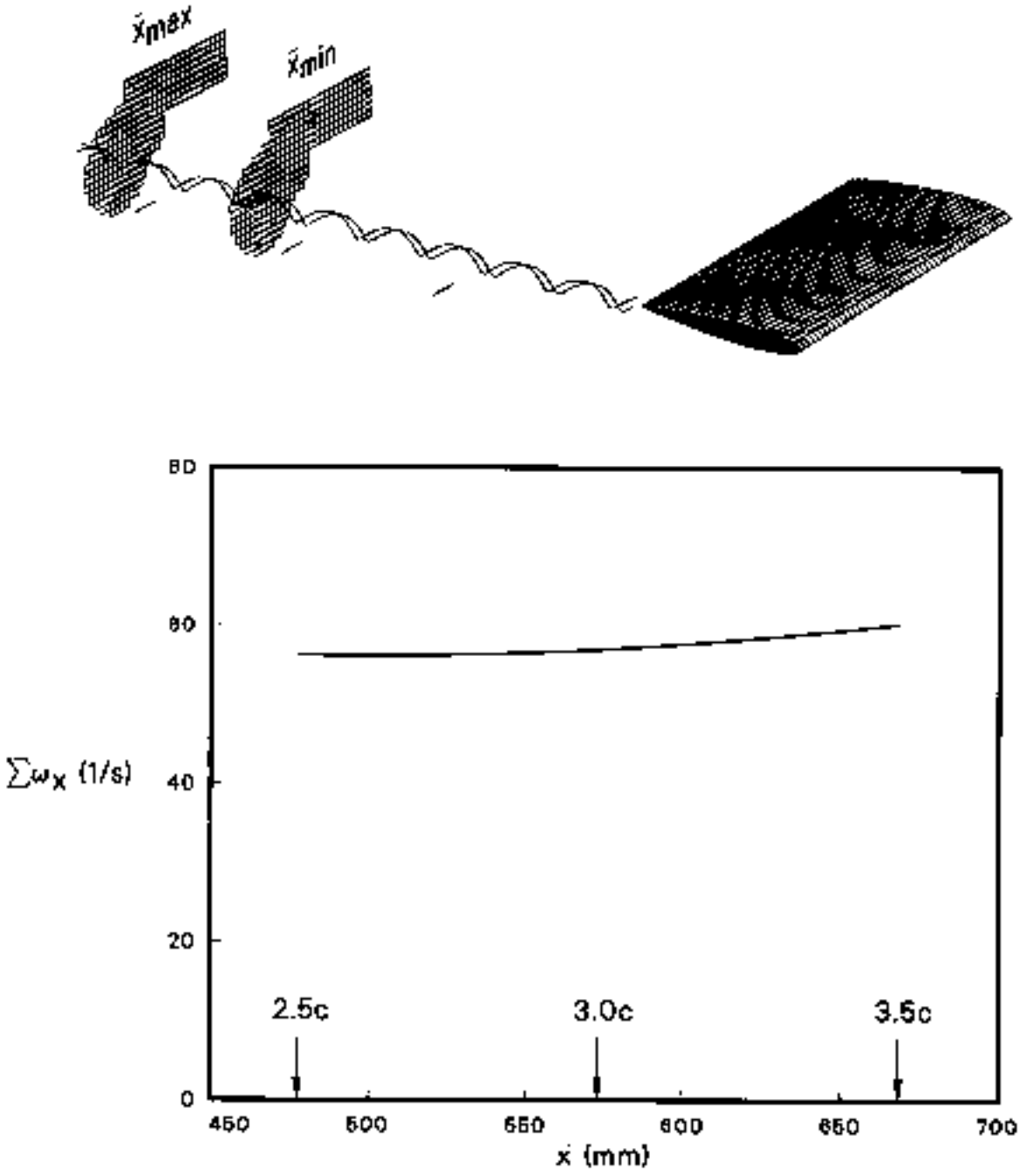

Figure 51. Summation of the streamwise component of vorticity (ω_X) over the y-z plane that cuts across the rotor wake during the time that the tip of the rotor blade advanced from 2.5 to 3.5 chord lengths past the measurement plane. The rotor speed was 1100 rpm.

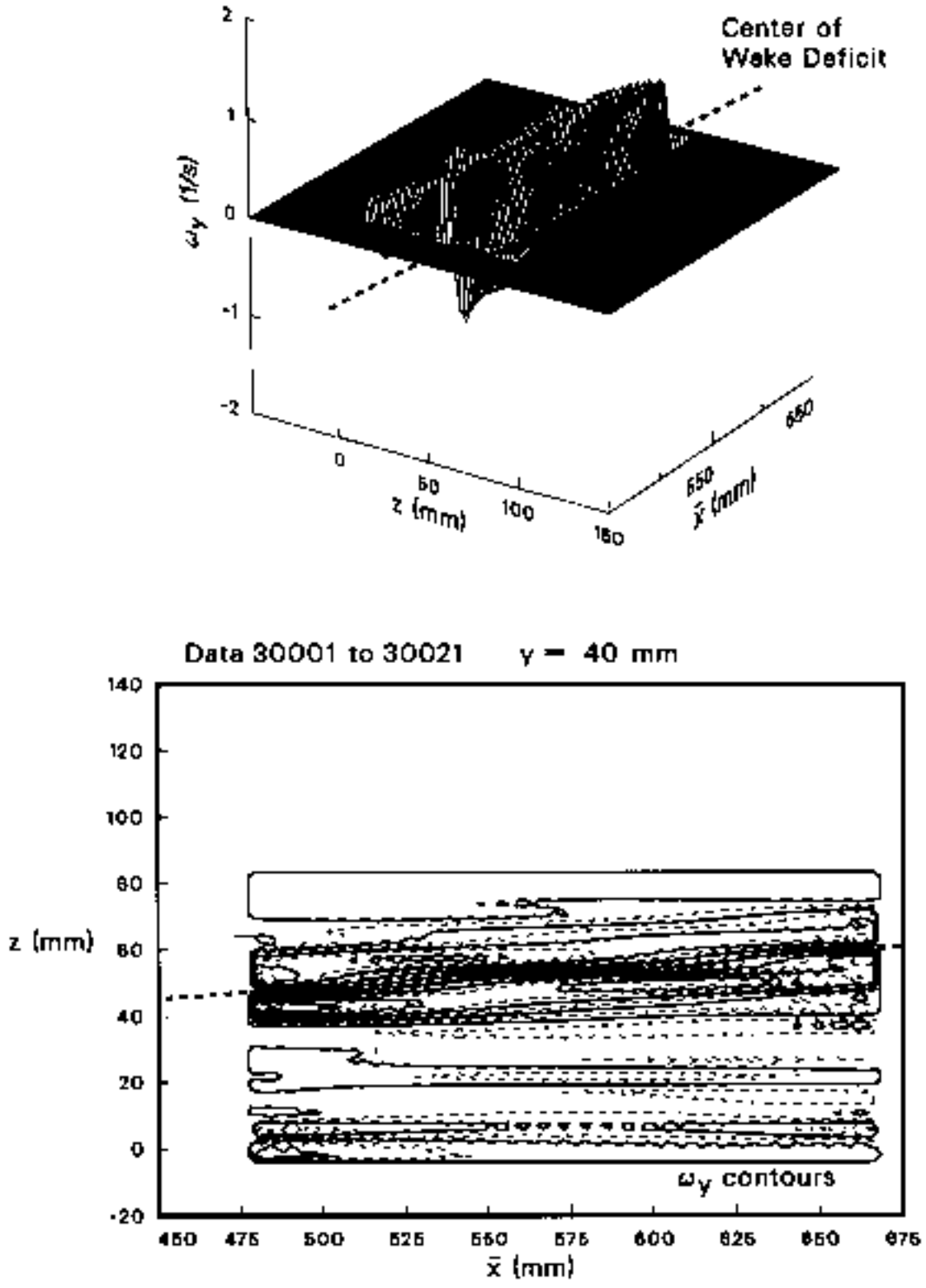

Figure 52. Spanwise component of vorticity (ω_Y) over the x-z plane at y = 40 mm during the time that the tip of the rotor blade advanced from 2.5 to 3.5 chord lengths. The rotor speed was 1100 rpm.

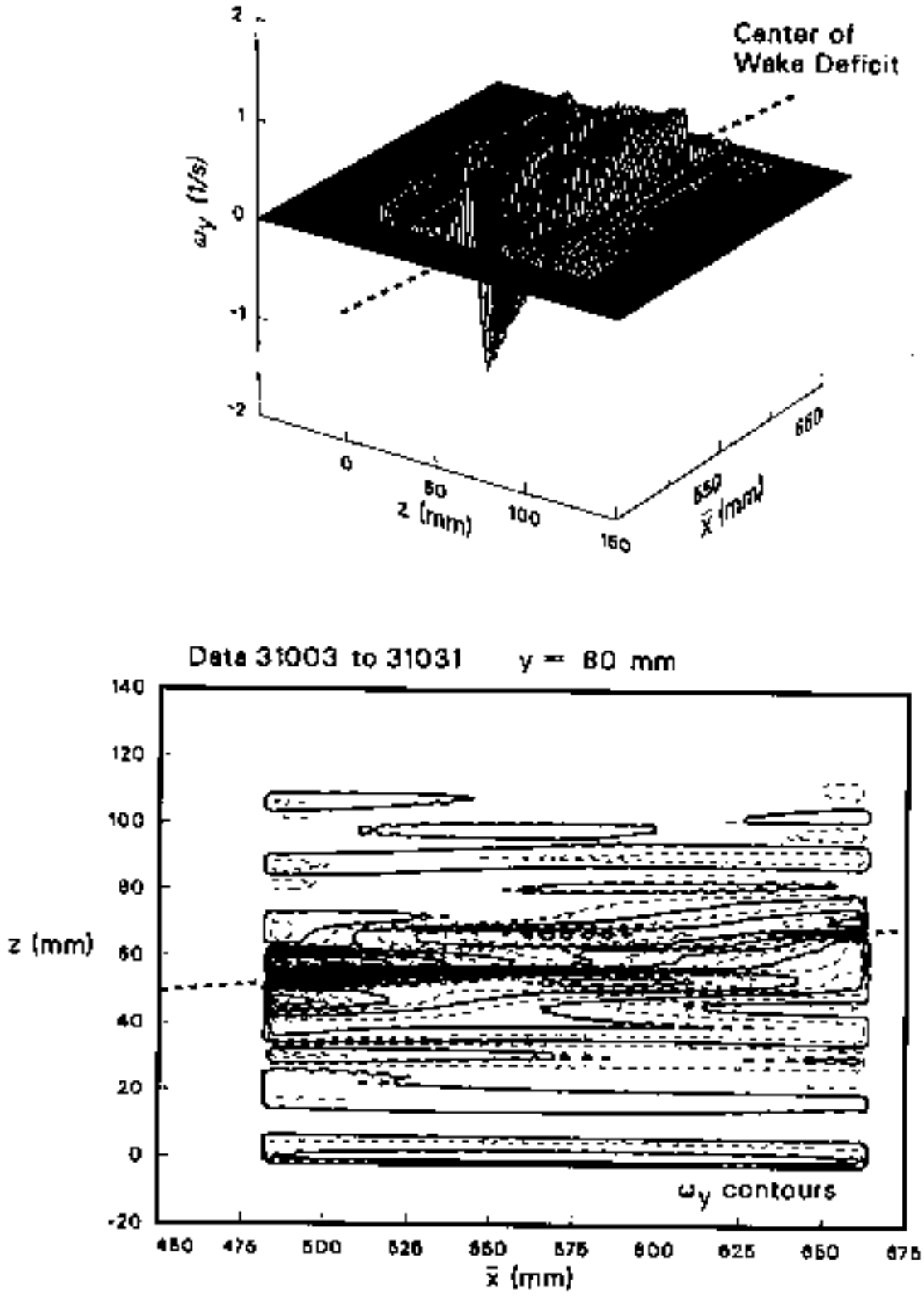

Figure 53. Spanwise component of vorticity (ω_Y) over the x-z plane at y = 80 mm during the time that the tip of the rotor blade advanced from 2.5 to 3.5 chord lengths. The rotor speed was 1100 rpm.

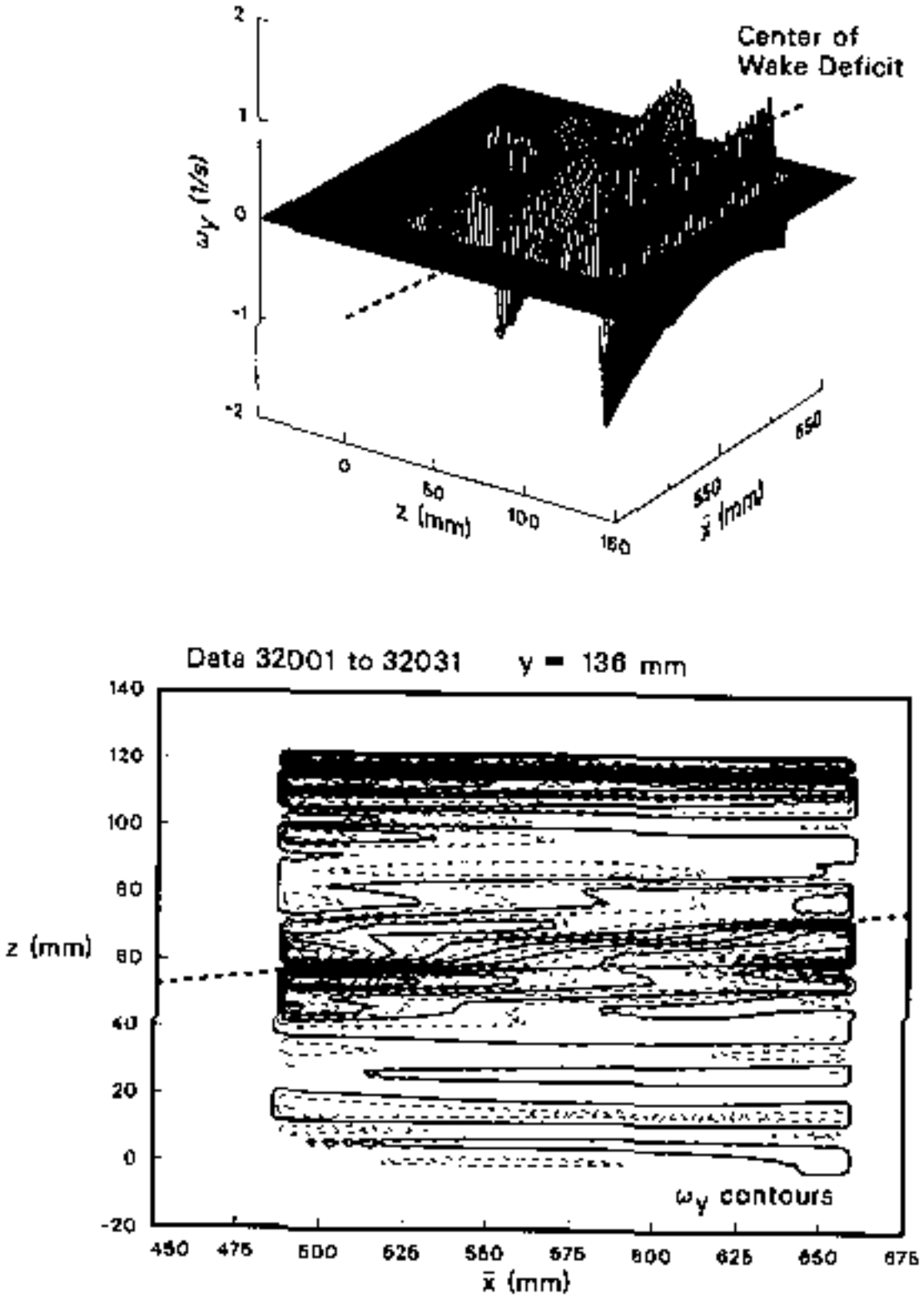

Figure 54. Spanwise component of vorticity (ω_Y) over the x-z plane at y = 136 mm during the time that the tip of the rotor blade advanced from 2.5 to 3.5 chord lengths. The rotor speed was 1100 rpm.

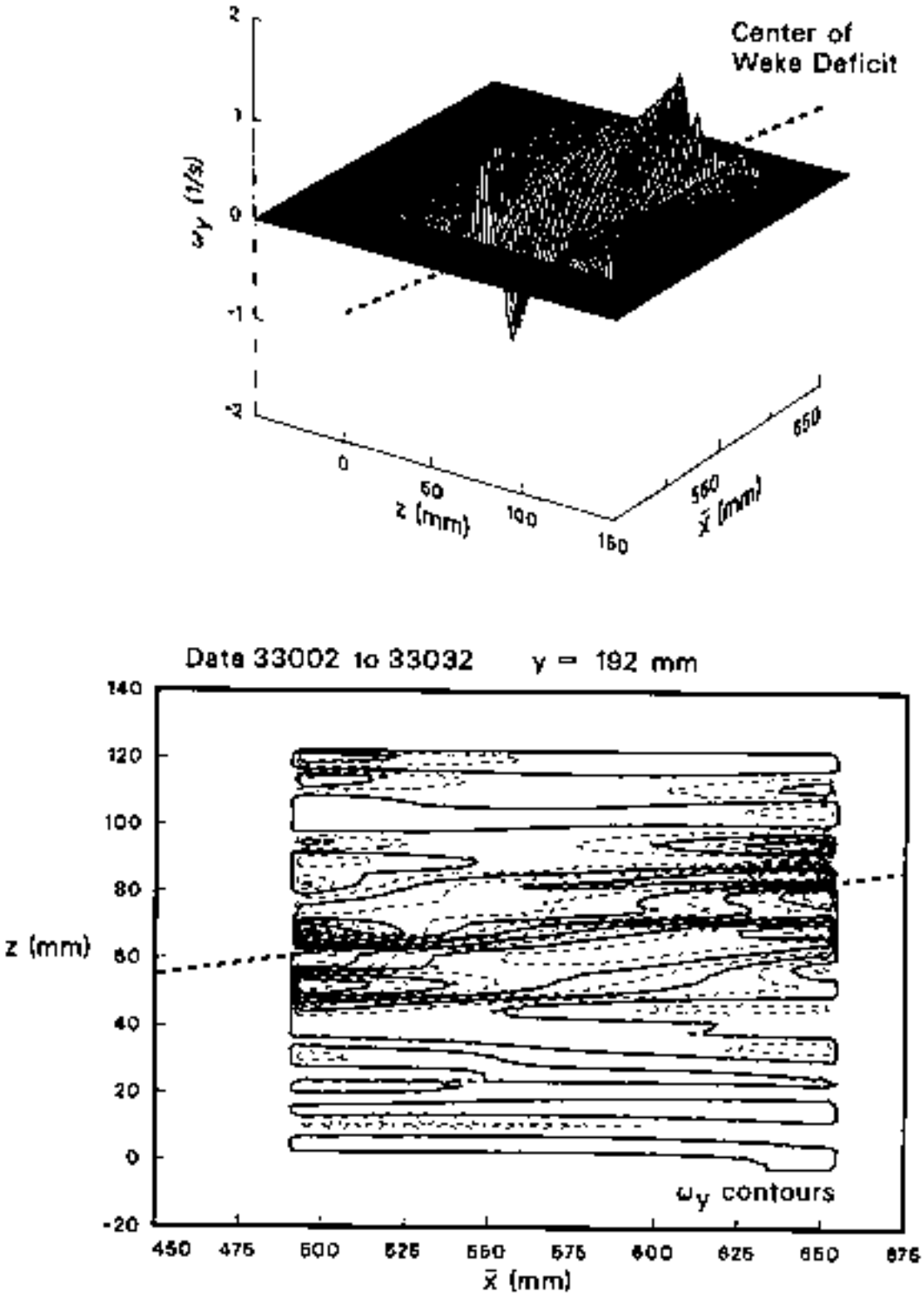

Figure 55. Spanwise component of vorticity (ω_Y) over the x-z plane at y = 192 mm during the time that the tip of the rotor blade advanced from 2.5 to 3.5 chord lengths. The rotor speed was 1100 rpm.

REPORT DOCUMENTATION PAGE

Form Approved
OMB No. 0704-0188

1. AGENCY USE ONLY (Leave blank)	2. REPORT DATE	3. REPORT TYPE AND DATES COVERED
	August 1995	Technical Paper

4. TITLE AND SUBTITLE

3-D Wake Measurements Near a Hovering Rotor for Determining Profile and Induced Drag

5. FUNDING NUMBERS

505-59-87

6. AUTHOR(S)

K. W. McAlister, C. A. Schuler,* L. Branum, and J. C. Wu**

7. PERFORMING ORGANIZATION NAME(S) AND ADDRESS(ES)

Ames Research Center, Moffett Field, CA 94035-1000 and Aeroflightdynamics Directorate, USAAVRDEC, ATCOM, Ames Research Center, Moffett Field, CA 94035-1000
*Aerometrics, Inc., Sunnyvale, California
**School of Aerospace Engineering, Georgia Institute of Technology, Atlanta, Georgia

8. PERFORMING ORGANIZATION REPORT NUMBER

A-950078

9. SPONSORING/MONITORING AGENCY NAME(S) AND ADDRESS(ES)

National Aeronautics and Space Administration
Washington, DC 20546-0001 and U.S. Army Aviation and Troop Command, St. Louis, MO 63120-1798

10. SPONSORING/MONITORING AGENCY REPORT NUMBER

NASA TP-3577
USAATCOM TR-95-A-006

11. SUPPLEMENTARY NOTES

Point of Contact: Kenneth W. McAlister, Ames Research Center, MS 215-1, Moffett Field, CA 94035-1000; (415) 604-5892

12a. DISTRIBUTION/AVAILABILITY STATEMENT

Unclassified-Unlimited
Subject Category –02

Available from the NASA Center for AeroSpace Information, 800 Elkridge Landing Road, Linthicum Heights, MD 21090; (301) 621-0390

12b. DISTRIBUTION CODE

13. ABSTRACT (Maximum 200 words)

Primarily an experimental effort, this study focuses on the velocity and vorticity fields in the near wake of a hovering rotor. Drag terminology is reviewed, and the theory for separately determining the profile- and induced-drag components from wake quantities is introduced. Instantaneous visualizations of the flow field are used to center the laser velocimeter (LV) measurements on the vortex core and to assess the extent of the positional meandering of the trailing vortex. Velocity profiles obtained at different rotor speeds and distances behind the rotor blade clearly indicate the position, size, and rate of movement of the wake sheet and the core of the trailing vortex. The results also show the distribution of vorticity along the wake sheet and within the trailing vortex.

14. SUBJECT TERMS	15. NUMBER OF PAGES
Rotor wake, Trailing vortex, Profile drag, Induced drag, Vorticity	70
	16. PRICE CODE: A04

17. SECURITY CLASSIFICATION OF REPORT	18. SECURITY CLASSIFICATION OF THIS PAGE	19. SECURITY CLASSIFICATION OF ABSTRACT	20. LIMITATION OF ABSTRACT
Unclassified	Unclassified		